

Stereolithographic hydrogel printing of 3D microfluidic cell culture chips

Zhang, Rujing; Larsen, Niels Bent

Publication date:
2017

Document Version
Publisher's PDF, also known as Version of record

[Link back to DTU Orbit](#)

Citation (APA):
Zhang, R., & Larsen, N. B. (2017). Stereolithographic hydrogel printing of 3D microfluidic cell culture chips. DTU Nanotech.

DTU Library

Technical Information Center of Denmark

General rights

Copyright and moral rights for the publications made accessible in the public portal are retained by the authors and/or other copyright owners and it is a condition of accessing publications that users recognise and abide by the legal requirements associated with these rights.

- Users may download and print one copy of any publication from the public portal for the purpose of private study or research.
- You may not further distribute the material or use it for any profit-making activity or commercial gain
- You may freely distribute the URL identifying the publication in the public portal

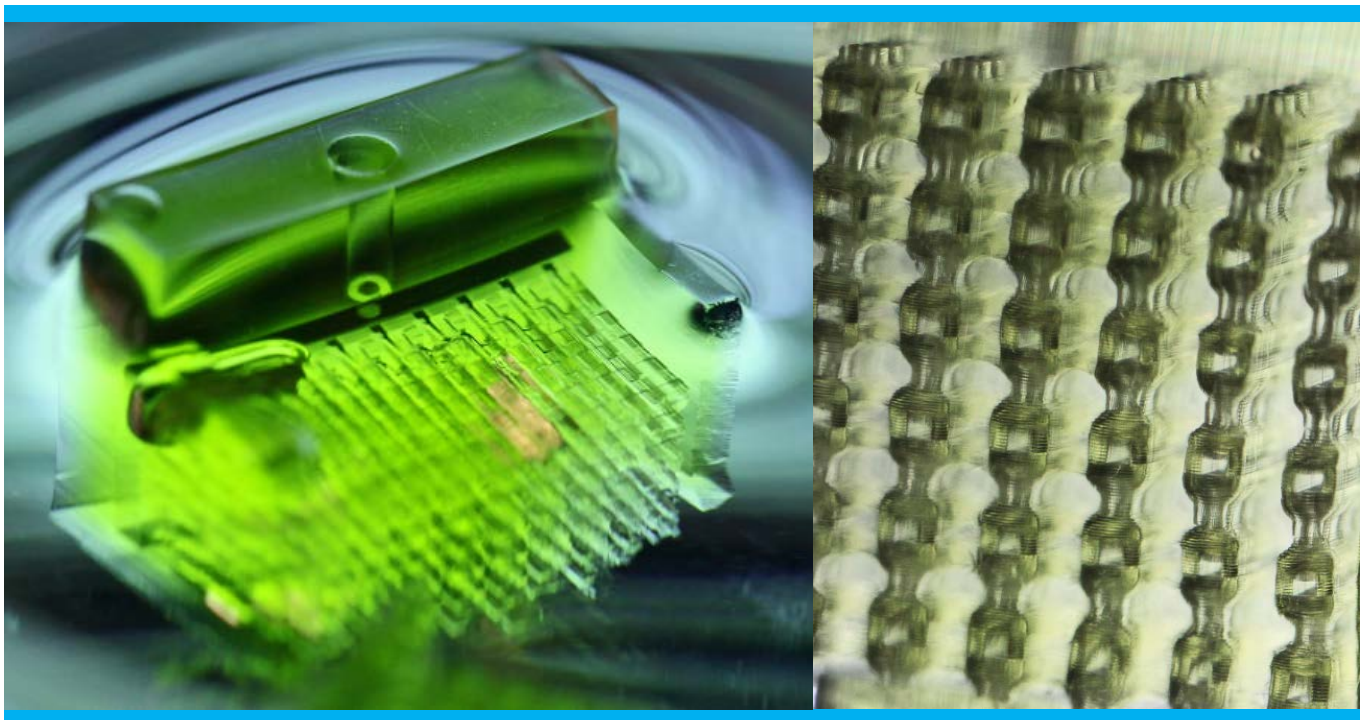
If you believe that this document breaches copyright please contact us providing details, and we will remove access to the work immediately and investigate your claim.



Stereolithographic hydrogel printing of 3D microfluidic cell culture chips

Rujing Zhang
PhD Thesis October 2017

Stereolithographic hydrogel printing of 3D microfluidic cell culture chips



Rujing Zhang (张如靖)

PhD Thesis

October 2017

Supervisor: Professor Niels B. Larsen

Abstract

Three-dimensional (3D) *in vitro* cell culture models capturing both the structural and dynamic complexity of the *in vivo* situation are in great demand as an alternative to animal models. Despite tremendous progress in engineering complex tissue/organ models in the past decade, approaches that support the required freedom in design, detail and chemistry for fabricating truly 3D constructs have remained limited. Here, we report a stereolithographic high-resolution 3D printing technique utilizing poly(ethylene glycol) diacrylate (PEGDA, MW 700) to manufacture diffusion-open and mechanically stable hydrogel constructs as self-contained chips, where confined culture volumes are supplied with oxygen and nutrients by perfusable vascular-like networks. An optimized resin formulation enables printing of hydrogel chips with perfusable multi-furcated microchannel networks, and the printed microchannels can be steadily perfused for at least one week. In addition, the integration of multiple independently perfusable and structurally stable channel systems further allows for easy combination of different bulk material volumes at exact relative spatial positions. We demonstrate this structural and material flexibility by embedding a highly compliant cell-laden gelatin hydrogel within the confines of a 3D printed resilient PEGDA hydrogel chip of intermediate compliance. Overall, our proposed strategy represents an automated, cost-effective and high resolution technique to manufacture complex 3D constructs containing microfluidic perfusion networks as advanced *in vitro* models for various biomedical applications such as drug development and *in vitro* disease modeling.

Multi-material stereolithographic printing based on epoxy and acrylate has also been demonstrated. Perfusion chips composed of a stiff epoxy component as structural supports interfacing the external world as well as compliant PEGDA component as microfluidic channels have been manufactured and perfused. Although still in the preliminary stage, this dual-material printing approach shows the potential for constructing complex 3D structures with heterogeneous components fulfilling different purposes.

Dansk resumé

Tre-dimensionelle (3D) *in vitro* celledyrkningsmodeller, der afspejler både den strukturelle og dynamiske kompleksitet af *in vivo* miljøer, er efterspurgt som et alternativ til dyremodeller. På trods af store fremskridt i udvikling af komplekse vævs-/organ-modeller i det forløbne tiår har kun et fåtal af de udviklede metoder kunnet bidrage med tilstrækkelige frihedsgrader i design, detaljegrad og kemi til at kunne fremstille sande 3D dyrkningsenheder. Vi beskriver her en stereolitografisk høj-opløst 3D printningsmetode der gør brug af poly(ethylenglykol) (PEGDA, 700 g/mol) til at fremstille diffusionsåbne og mekanisk stabile hydrogelenheder som selvstændige chips, hvor afgrænsede dyrkningsvolumener bliver forsynet med oxygen og næringsstoffer fra væskegennemstrømning i blodkars-lignende netværk af kanaler. En optimeret sammensætning af den anvendte printevæske tillader printning af hydrogel-chips som har gennemstrømbare mikrokkanaler med et tværsnit på ned til 100 µm x 100 µm, og de printede mikrokkanaler kan gennemstrømmes med dyrkningsvæske i mindst en uge. Yderligere tillader integration af separate uafhængige kanalsystemer i chipenheden at forskellige volumener i enheden kan fyldes med forskellige materialer med stor indbyrdes rumlig præcision. Vi demonstrerer denne fleksibilitet i struktur og materialer ved at indlejre en meget mekanisk eftergivende celle-fyldt gelatine hydrogel i et defineret hulrum i en 3D printet PEGDA hydrogel chip af middel eftergiveness. Overordnet set udgør vores foreslåede tilgang en automatiseret, omkostningseffektiv og høj rumligt opløst metode til at fremstille komplekse 3D enheder indeholdende mikrofluide kanalnetværk, som kan anvendes som avancerede *in vitro* modeller i en række biomedicinske anvendelser så som medicinudvikling og *in vitro* sygdomsmodeller.

Fler-materiale stereolitografisk printning baseret på epoxy- og akrylat-udgangsmaterialer er også blevet demonstreret: Chips med mikrofluide kanaler er blevet fremstillet, hvor en printet stiv epoxy-baseret komponent er anvendt som strukturel understøttelse som grænseflade til omverdenen og en printet middel eftergivende PEGDA komponent fungerer som vægge i mikrofluide kanaler. Væskegennemstrømning af de printede mikrokkanaler er efterfølgende vist. Disse foreløbige resultater fra fler-materiale printning illustrerer potentialet for at fremstille komplekse 3D strukturer med forskellige komponenter der opfylder forskellige krav.

Table of Contents

Chapter 1:

Introduction	1
1.1 Motivation and project goal.....	1
1.2 Why transition from 2D to 3D?	3
1.3 Animal models.....	4
1.4 Conventional 3D cell culture models	4
1.4.1 Scaffold-free models	4
1.4.2 Scaffold-based models	6
1.4.2.1 Porous scaffolds with simultaneous cell encapsulation	6
1.4.2.2 Porous scaffolds with post-fabrication cell seeding	8
1.4.3 Limitations of conventional 3D cell culture models	8
1.5 Planar microfluidic cell culture models	9
1.5.1 Fabrication of planar microfluidic devices	9
1.5.2 The unique physical features that the microscale provides	10
1.5.3 “Organs-on-chips”	11
1.5.4 Limitations of planar microfluidic cell culture models	12
1.6 3D printing based cell culture models	14
1.6.1 Droplet-based printing	15
1.6.2 Powder-based printing	16
1.6.3 Extrusion-based printing	17
1.6.4 Stereolithography	22
1.6.4.1 The basics of stereolithography	22
1.6.4.2 Resins used for stereolithography	24
1.6.4.3 Stereolithography in constructing cell culture models	26
1.6.4.4 Limitations of stereolithography	27
1.6.4.5 Summary	28

Chapter 2:

Hydrogel 3D microfluidics based on a modified commercial stereolithography printer	30
2.1 Choice of resin components	30
2.2 The effect of photoabsorber on resin curing depth	32
2.3 Modification of the commercial printer	33
2.4 Optimization of printing configurations	34
2.4.1 The importance of a non-adhesive surface at the vat bottom	34
2.4.2 The spatial printing resolution for microchannels	35
2.4.3 The effect of PEGDA concentration on printing	37
2.5 Cell compatibility of the printed PEGDA hydrogel constructs	38
2.6 Perfusion of printed PEGDA microchannels with full 3D design freedom	39

2.7 Conclusion	42
2.8 Experimental section	43
2.8.1 Materials	43
2.8.2 LAP synthesis	43
2.8.3 Pre-treatment of cover slip surfaces	43
2.8.4 Projection stereolithography of PEGDA hydrogels	43
2.8.5 Perfusion of printed PEGDA microchannels	44
2.8.6 Cell culture	44
2.8.7 Cell compatibility of printed PEGDA hydrogel sheets	45
 Chapter 3:	
Hydrogel 3D microfluidics based on a home-built polychromic stereolithography printer	46
3.1 Optimization of the spatial printing resolution for microchannels	46
3.2 Swelling and mechanical properties of 3D printed PEGDA hydrogels	51
3.3 Perfusion of printed PEGDA microchannel networks	54
3.4 Cell compatibility of the printed micro-perfusable chip constructs	59
3.5 Embedding of cell-laden matrices in printed perfusable hydrogel chips	61
3.6 Printing and perfusion of a massively perfusable tissue chip	69
3.7 Conclusion	72
3.8 Experimental section	72
3.8.1 Materials	72
3.8.2 LAP synthesis	72
3.8.3 GelMA synthesis	73
3.8.4 Pre-treatment of cover slip surfaces	73
3.8.5 Projection stereolithography of PEGDA hydrogels	73
3.8.6 Analysis of swelling properties of printed PEGDA hydrogels	74
3.8.7 Analysis of mechanical properties of printed PEGDA hydrogels	74
3.8.8 Perfusion of printed PEGDA microchannel networks	75
3.8.9 Cell culture	75
3.8.10 Cytotoxicity assay	75
3.8.11 Endothelialization of perfusion microchannels	76
3.8.12 Multi-furcated 3D perfusion culture constructs	76
3.8.13 Perfusion culture in printed 3D hydrogel microfluidic chips	77
 Chapter 4: Multi-material stereolithographic printing	79
4.1 Optimization of epoxy and PEGDA concentration	81
4.2 Printing and perfusion of dual-material constructs	83
4.3 Conclusion	85
4.4 Experimental section	85
4.4.1 Materials	85
4.4.2 Projection stereolithography of dual-material constructs	85

4.4.3 Perfusion of dual-material printed constructs	85
Chapter 5:	
Discussion	87
5.1 The advantages of our proposed approach	87
5.1.1 Direct embedding 3D complex and well-defined perfusion channel networks in hydrogel materials at high spatial resolutions	87
5.1.2 Diffusion-open and mechanically stable hydrogel constructs as self-contained 3D microfluidic chips that allow for long-term steady perfusion cultures	88
5.2 The limitations of our proposed approach	89
5.2.1 Inability to encapsulate cells during fabrication and limited capability of incorporating multiple materials	89
5.2.2 Inability to establish direct cell-cell contact between cells cultured in different compartments within the same culture chip	90
5.3 Summary and future work	90
Chapter 6:	
Conclusion and outlook	92
Acknowledgements	95
Reference	97
External dissemination	109
Appendix.....	110

List of abbreviations

3D	three-dimensional
PEGDA	poly(ethylene glycol) diacrylate
ECM	cell-extracellular matrix
PEG	poly(ethylene glycol)
RGD	arginine-glycine-aspartate
PLGA	poly(lactic-co-glycolic acid)
HA	hydroxyapatite
PDMS	polydimethylsiloxane
CAD	computer-aided design
FDM	fused deposition modeling
PCL	poly(caprolactone)
PLA	poly(lactic acid)
SLA	Stereolithography
DLP	digital light projection
LCD	liquid crystal display
DMD	digital micromirror device
2PP	two-photon polymerization
MRI	magnetic resonance imaging
CT	computed tomography
PPF	poly(propylene fumarate)
SEM	Scanning electron microscopy
LAP	lithium phenyl-2,4,6-trimethylbenzoylphosphinate
QY	quinoline yellow
DI	deionized
PMMA	poly(methyl methacrylate)
FEP	fluorinated ethylene propylene
LED	light emitting diode
HUVEC	Human umbilical vein endothelial cells
GelMA	gelatin methacrylate
CQ	camphorquinone
CAT2	triarylsulfonium hexafluoroantimonate salts
EEC	3,4-epoxycyclohexylmethyl 3,4-epoxycyclohexanecarboxylate
Sudan I	1-phenylazo-2-naphthol
PC	propylene carbonate
DGDE	diethylene glycol diethyl ether

Chapter 1:

Introduction

1.1 Motivation and project goal

During the past decades, biomedical research has flourished in many aspects, from cell and molecular biology that aims to promote better understanding of human physiology, to drug development that aims to provide better therapeutics, and ultimately to tissue engineering that aims to replace damaged tissues or organs. Cell culture model, as an essential component in all of those abovementioned research fields, plays an important role in unraveling the complexity of biological systems.

Much progress has been made in cell culture models, from traditional 2D monolayer cultures to well-engineered 3D culture models. The most common substrates for supporting cell growth have been made from polystyrene and glass and have taken the form of a flat two-dimensional (2D) surface.¹ Such robust and convenient approach has been routinely adopted by researchers for their daily work, and it has contributed greatly to our understanding of basic cell and molecular biology. In the meantime, its overly simplistic nature has frequently raised doubts about how relevant it is for interpreting the information obtained compared to the extremely complex native biological systems. Therefore, the importance of a 3D cell culture model has been widely recognized and techniques that can achieve 3D cell culture are in great demands.

The key challenge in constructing functional 3D culture models is vascularization. Native tissues and organs are supplied with oxygen and nutrients through an intricate vascular network which constantly delivers convective blood flow locally, while the maintenance of cells cultured *in vitro* within a 3D environment is mainly dependent on the slow diffusion of soluble factors from the surrounding culture medium. Therefore, a healthy *in vitro* 3D cell culture at a physiologically relevant scale remains a major challenge.

With the advent of 3D printing techniques, fabrication of 3D cell culture models with embedded artificial vascular-like channel network has become possible. There are many existing 3D printing techniques, all of which have their own advantages and disadvantages. Therefore how to choose suitable materials and techniques takes much consideration depending on models of interest and intended applications. While some techniques focus on biological relevance and complexity, others focus on manufacturability. Ideally, a balance needs to be well kept so that an adequately complex system can also be manufactured in a cost-efficient, automated and user-friendly manner, which would make it easier to disseminate outside research labs and ultimately contribute to the social welfare.

In addition, although the ability to manufacture exact replicas of natural tissue or organs *in vitro* is extremely attractive, we are still far away from that stage. A currently more realistic aim is to provide enough functionality for those constructed culture models to serve as clinically useful replacements for damaged tissues or as *in vitro* models for scientific

studies such as disease modeling and drug development. Since native cellular systems are very complex, the degree to which researchers must control the cellular microenvironment to elicit desired biological response is still largely unclear,² and there will be a continuing process that involves model construction and model validation.

Motivated by all those challenges and inspirations discussed previously, the goal of this PhD project is to develop a facile and reproducible 3D printing-based fabrication platform for vascularized 3D cell culture models that aim to serve as *in vitro* tissue models for applications such as drug screening and *in vitro* disease modeling rather than *in vivo* implants. More specifically, we aim to use stereolithographic 3D printing to manufacture diffusion-open and mechanically stable hydrogel constructs as self-contained 3D microfluidic chips, where confined cell culture units are supplied with oxygen and nutrients through independently perfusable vascular-like networks, as illustrated in green for the culture unit and in red for the perfusion network in **Figure 1.1**. The goal of the project is further divided into the following tasks:

1. Develop a suitable cost-efficient resin for printing diffusion-open yet mechanically stable hydrogel constructs with embedded true 3D microfluidic channel networks of physiologically relevant sizes.
2. Develop a facile platform for steady and long-term perfusion of constructed hydrogel chips.
3. Develop a platform for long-term perfusion cultures of cells within constructed hydrogel chips.

The present progress in the field as well as existing techniques used for 3D cell cultures are reviewed in the following sections. The 3D printing technique used in this project, stereolithography, as well as the current challenges that motivate us to carry out this project are highlighted.

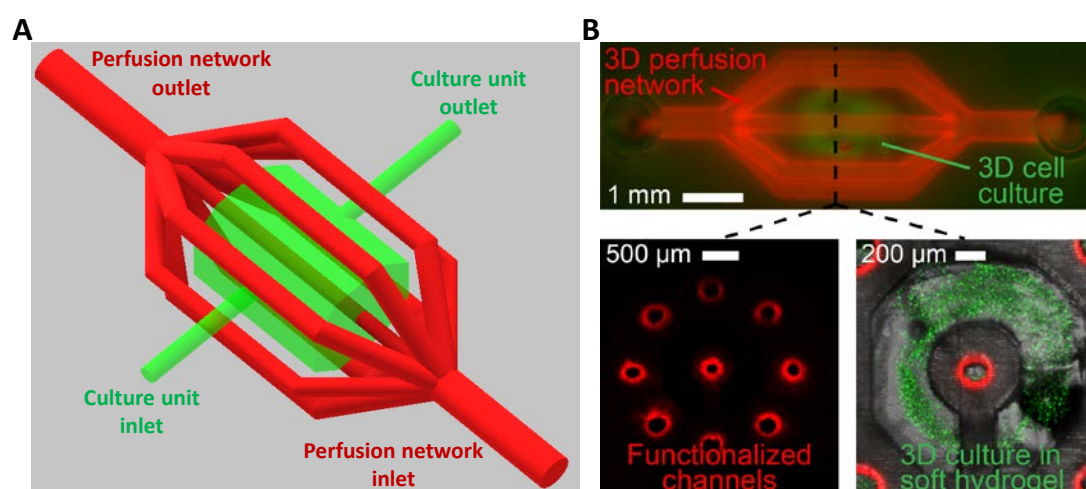


Figure 1.1 A) A schematic diagram of a generic 3D hydrogel microfluidic chip design containing a cell culture unit (green) surrounded and traversed by a perfusion fluidic channel network (red). B) Wide-field fluorescence image (top view) of the printed 3D microfluidic chip showing the vascular-like

network coated by rhodamine (red) and the chamber filled with live fibroblasts (green)-laden gelatin hydrogel, as well as confocal fluorescence images of a cross-sectioned slice of the printed hydrogel chip showing the perfused vascular-network (red), live fibroblasts (green) and the printed hydrogel chip outline (transmitted light, grey).

1.2 Why transition from 2D to 3D?

Cell culture is essential to many biomedical studies including cell biology, pathology, tissue engineering as well as development of therapeutic drugs.³ So far cell culture studies have mainly been performed in a form of cellular monolayer on 2-dimensional (2D) planar surfaces, such as polystyrene well plates, flasks and Petri dishes. Those conventional 2D cell culture systems represent a convenient, affordable and robust technical platform that has been extensively adopted by researchers and has notably improved the understanding of human biology and disease.⁴ However, in the body, nearly all cells reside in a 3D microenvironment composed of vasculature enabling oxygen and nutrients supply as well as metabolic wastes removal, soluble factors, cell-extracellular matrix (ECM) interactions and cell-cell communications (**Figure 1.2**).⁵ Those elements constitute the specific cell microenvironment and work in concert to regulate various cellular behaviors and functionalities. Conventional 2D culture systems fail to recapitulate such complex microenvironment and subsequently often produce misleading results in predicting *in vivo* responses. It is now commonly accepted that cells cultured in their native 3D environments behave differently compared to those cultured in 2D in many cellular processes, such as morphology, proliferation, migration and drug sensitivity.⁶ As a result, 3D cell culture models that better mimic *in vivo* conditions are in great demand.

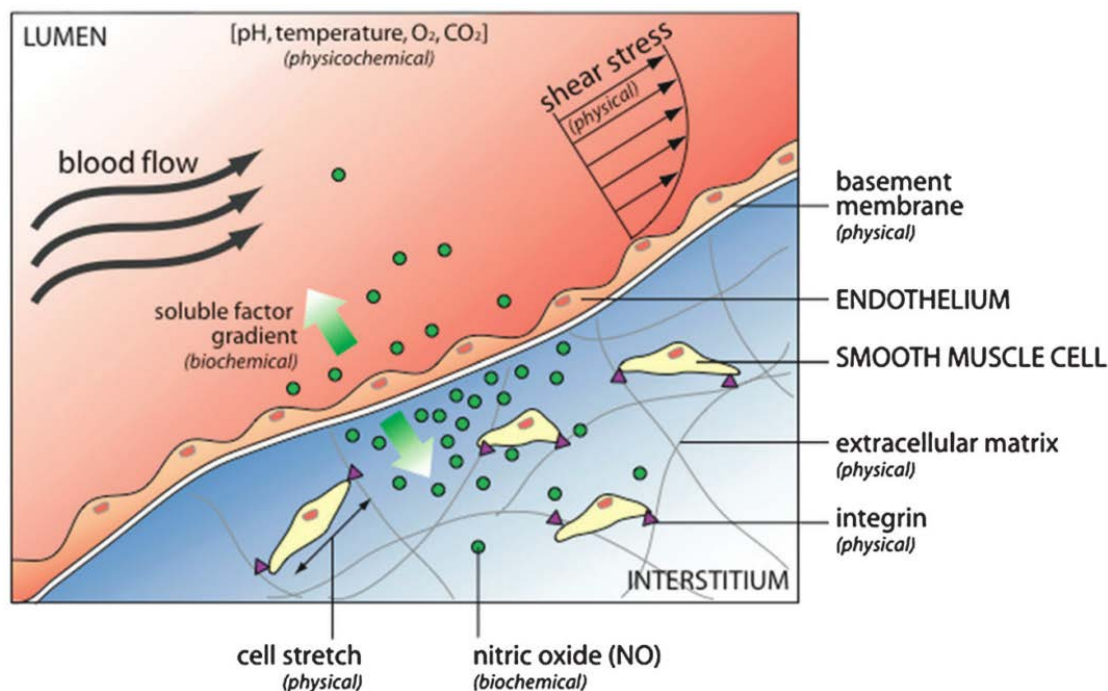


Figure 1.2 The cell microenvironment is composed of multiple elements. For example, the endothelium that lines blood vessels is exposed to hemodynamic shear stress (external physical force) that stimulates a biochemical response. Soluble factor molecules diffuse to neighboring smooth

muscle cells (SMCs), where they regulate cell contraction and relaxation. The gradient of diffused soluble factors affect nearby SMCs more than distant SMCs. Endothelial cells are anchored to the basement membrane, while SMCs are anchored to the ECM of the interstitium, both through integrins that act as sensors and transducers of physical force. Local physicochemical properties ensure proper regulation of both physical and biochemical mechanisms.⁵ Reproduced from ref. 5.

1.3 Animal models

Animal models, exemplified by rodents, dogs and monkeys, provide greater physiological relevance compared to traditional 2D cell cultures. Consequently they have been widely implemented to investigate the underlying cellular mechanisms of human physiology and have become the standard procedure of drug screening prior to clinical trials. However, animal models are expensive, time-consuming and ethically controversial.⁶ Furthermore, it is difficult to independently control experimental variables in animal models and their clinical translatability has been questioned largely due to the species difference between animals and humans.⁷ Approximately only 10% of the drug candidates entering the clinical trial reach the final approval stage and enter the market.⁸ Therefore, *in vitro* 3D cell culture models capturing the complexity of *in vivo* tissues and organs are emerging as a bridge between traditional 2D cell cultures and *in vivo* animal models, and have gained ever increasing attention for their use in a variety of biomedical applications such as drug development and toxicology.¹

1.4 Conventional 3D cell culture models

Several conventional 3D cell culture models have been developed and they can generally be grouped into two categories: 1) scaffold-free models, exemplified by cell spheroid cultures (**Figure 1.3A**), and 2) scaffold-based models, exemplified by porous scaffolds with either simultaneous cell encapsulation or post-fabrication cell seeding (**Figure 1.3B**).

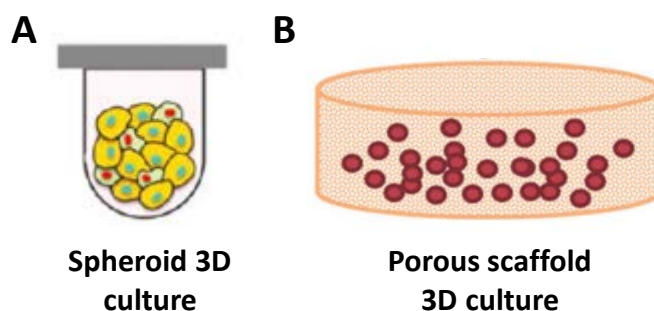


Figure 1.3 A schematic diagram of conventional 3D cell culture models: scaffold-free (A)⁹ and scaffold-based models (B)¹⁰. Adapted from ref. 9 (A) and ref. 10 (B).

1.4.1 Scaffold-free models

Cell spheroids are simple 3D culture models and can be generated by several techniques such as hanging drop, rotating culture and concave plates with non-adhesive surface coating.

The formation is based on the tendency of adherent cells to aggregate. As a result, spheroids as compact cell aggregates have found many uses especially in modeling solid tumor.¹ However, it is generally challenging to well control the size of formed cell spheroids. Also, when spheroids grow beyond a certain size, the diffusion of oxygen and nutrients becomes limited and subsequently leads to necrosis in the spheroid core.¹¹ Most cells *in vivo* are supplied with oxygen and nutrients by an intricate vascular system composed of larger blood vessels that are subdivided into small capillaries. The adoption of such vascular system is due to the fact that diffusion only becomes a significant way of mass transport in the short length scale. Unlike convection in which the mass transport is linearly dependent on time if the volumetric flow rate is constant, diffusion distance is proportional to the square root of time according to the Einstein-Smoluchowski relation:

$$d = \sqrt{2Dt} \text{ (in one dimension)}$$

where d is the linear distance a particle has moved from its initial position in a time t , and D is the diffusion coefficient of the particle.¹² Consequently, although diffusion occurs continuously, it is an extreme slow process over a large length scale. For example, oxygen in water takes about 5 min to diffuse 1 mm ($D = 2 \times 10^{-9} \text{ m}^2/\text{s}$)¹³, but only 2 sec to diffuse 100 μm . Hence, cells *in vivo* are supplied with oxygen and nutrients through pervasive convective blood flows followed by local diffusion. Also, oxygen is being consumed by cells as it diffuses, thereby creating a maximum distance between cells and their closest capillaries where the diffusion is fast enough to compensate for the consumption. Such distance depends on various parameters including cell density and consumption rate. In native tissues, this maximum distance is typically a few hundred micrometers, although it may be much smaller in highly metabolically active tissues like heart muscles (**Figure 1.4**).¹⁴ Studies have shown that under appropriate culture conditions vascular endothelial cells can self-assemble to form new microvascular networks, a process called vasculogenesis.^{2,15} However, such spontaneous process occurs too slowly to supply the cells with adequate oxygen and nutrients during the time needed for a mature network to form.¹⁶ Therefore a general strategy to embed artificial vascular-like networks within cell culture models is in great demand.

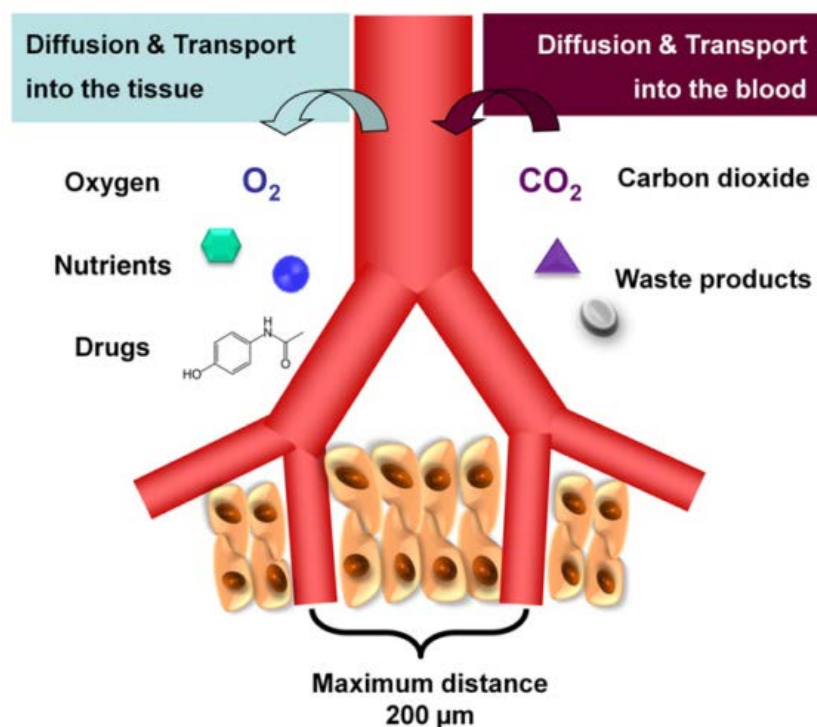


Figure 1.4 A schematic diagram of diffusion and transport processes in vascularized tissues *in vivo*.¹⁴ Reproduced from ref. 14.

1.4.2 Scaffold-based models

The use of a scaffold becomes more necessary as the size and complexity of a 3D model increases.¹ Materials used for scaffolds can be divided into four groups: metals, ceramics, polymers and their composites.⁴ Among them, polymeric materials are the most widely used due to their great flexibility in controlling both their mechanical and chemical properties.

1.4.2.1 Porous scaffolds with simultaneous cell encapsulation

Porous scaffolds with simultaneous cell encapsulation are mostly restricted to hydrogel materials, which are polymeric crosslinked networks with high water content and recapitulate many physical and chemical properties of ECM.¹⁷ A hydrogel pre-polymer aqueous solution is mixed with a cell suspension and then quickly gelled through physical or/and chemical crosslinking mechanisms (**Figure 1.5**). Chemically crosslinked hydrogels are formed through covalent networks and therefore cannot dissolve in water without breakage of covalent bonds, while physical hydrogels are formed by dynamic and reversible networks based on non-covalent interactions such as hydrogen bond, hydrophobic and electrostatic interaction.¹⁸ As for polymers used for hydrogels, they are typically grouped into naturally derived (from living sources) and synthetic polymers.¹ Naturally derived polymers, such as collagen and gelatin, generally mimic the native *in vivo* ECM composition better than synthetic polymers and possess many intrinsic biological cues for directing multiple cellular behaviors such as cell adhesion and migration.¹⁹ However, they often suffer from poor mechanical properties and batch-to-batch variations.²⁰ On the other hand, synthetic

polymers, such as poly(ethylene glycol) (PEG), can be readily tailored to accommodate a range of physical and chemical requirements based on the specific application by controlling their chemical compositions, molecular weight, crosslinking density and so on. However, due to their general bio-inactivity, post modifications are usually required to render them adequate biofunctionality. For instance, conjugating PEG polymers with cell adhesive peptide sequences like arginine-glycine-aspartate (RGD) motif is a commonly used strategy to promote cell adhesion and compatibility for bioinert polymers.¹⁹

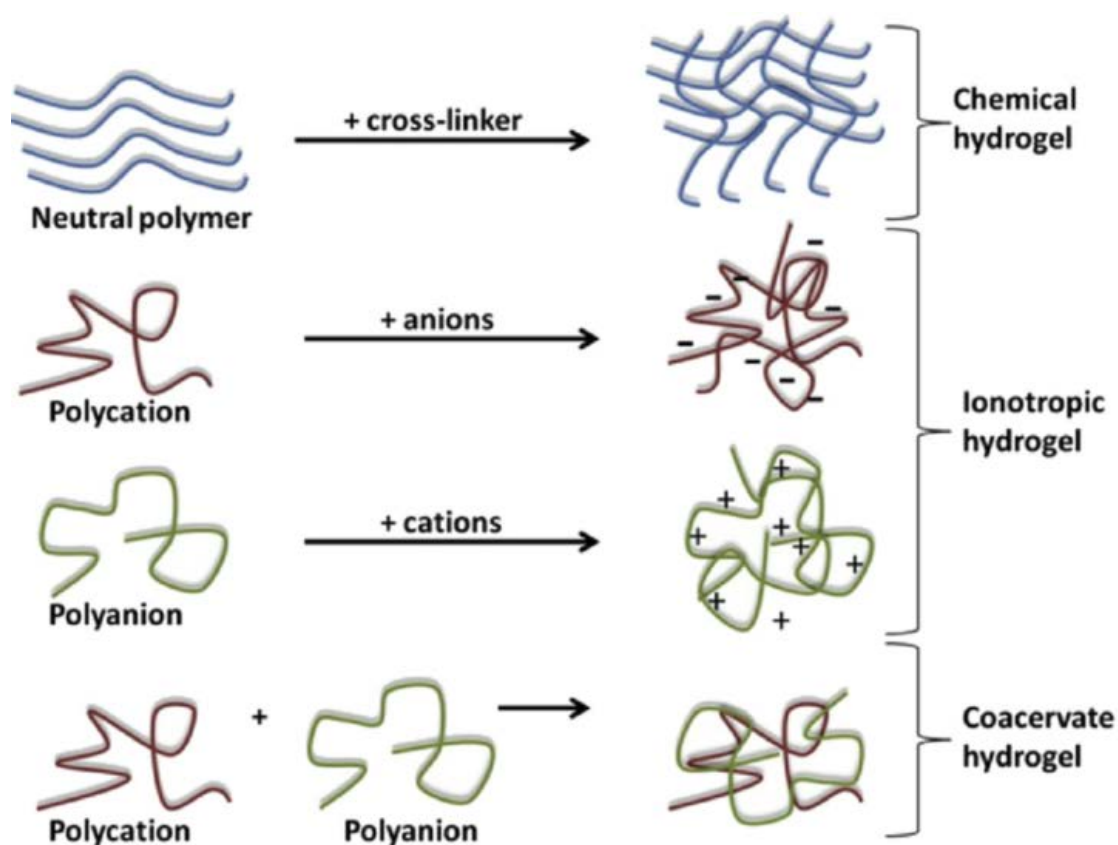


Figure 1.5 A schematic diagram of representative mechanisms for hydrogel formation.²¹ Reproduced from ref. 21.

Cell-encapsulated hydrogels have been extensively used as 3D *in vitro* models because they provide cells with their native 3D environment as well as cell-ECM interactions. Therefore distinct differences in cellular behaviors including morphogenesis, migration and differentiation have been observed compared to conventional 2D cultures. For example, breast epithelial cells cultured within 3D hydrogels formed an acinus structure possessing a cellular morphology similar to an *in vivo* structure that was never observed in 2D culture.²² The high water content in hydrogels, which contains soluble nutrients and oxygen, can initially maintain cellular activity. However, the low solubility and slow diffusion of oxygen in water will eventually prevent sufficient oxygen supply, and meanwhile those random submicron-sized porous structures formed during the gelling process prohibits sufficient convective flow within hydrogels. Therefore adequate cell viability can only be maintained in

a limited thickness.⁴ Cells embedded deep within hydrogels cannot survive for long due to insufficient supply of oxygen and nutrients.

1.4.2.2 Porous scaffolds with post-fabrication cell seeding

As an alternative to hydrogel encapsulation, cells can also be seeded onto scaffolds after fabrication. Since cells are not involved during fabrication process, there is more flexibility in choosing materials and manufacturing techniques. A wide range of polymers can be used to construct porous scaffolds by conventional manufacturing techniques such as freeze-drying, gas foaming, solvent casting and particulate leaching.⁴ The usually formed random micro-sized porous structures allow for diffusional mass transport as well as cell seeding.

Cell-seeded porous scaffolds have found many uses especially in tissue engineering. Specifically, osteoblast-seeded porous scaffolds composed of biodegradable poly(lactic-co-glycolic acid) (PLGA) and bioceramics (hydroxyapatite, HA) are widely used for bone tissue engineering. The biodegradable scaffolds provide temporal structural support for cells and are gradually degraded and subsequently replaced by newly formed bone tissues after implantation.²³ However, it is very difficult to control the microscale structural characteristics of such porous scaffolds fabricated by those conventional techniques, including porosity, pore interconnectivity, pore size and geometry, and pore-size distribution, which are closely related to scaffold performance such as mass transport, cell distribution and growth.⁴ Despite the generally larger pore size in such porous scaffolds compared to hydrogels, mass transport *via* passive diffusion still will be limited and cell distribution is often limited to the area close to the scaffold surface.⁴

1.4.3 Limitations of conventional 3D cell culture models

Despite the great contributions made by those conventional 3D cell culture models, there are still some major drawbacks.^{10,24}

Firstly, they generally lack an adequate vascularization strategy to ensure sufficient supply of nutrients and oxygen throughout the whole model. Therefore, sufficient cell viability can only be maintained within a limited 3D depth. As a result, vascularization in full 3D remains the key challenge in maintaining healthy cell cultures at a clinically relevant scale.¹⁴

Secondly, for scaffold-based models it is challenging to control structural characteristics of scaffolds due to their conventional manufacturing techniques.

Thirdly, they generally represent static culture conditions and therefore lack the ability to mimic the biochemically dynamic characteristics of *in vivo* systems. Although bioreactors commonly composed of a spinning or rotating container have been used to accommodate conventional 3D cell cultures and subsequently to facilitate nutrient supply and control over environmental conditions, their macroscale nature usually produces poorly defined fluidic dynamics.^{1,25,26}

Consequently, microfluidic and 3D printing-based cell culture models have been developed to address the above shortcomings.

1.5 Planar microfluidic cell culture models

Microfluidic devices, where fluids can be precisely manipulated at microscale, are built with technologies first developed by the semiconductor industry.²⁷ Basically, microfluidic cell culture models integrate microfluidics with those conventional 2D or 3D culture models. Cells can be cultured in microfluidic devices as a monolayer or as 3D modules such as spheroids and cell-encapsulated hydrogels. The major advantage of microfluidic cell culture over conventional cell cultures lies in its ability to manipulate fluids and its compartmental nature. However, due to their planar fabrication process, currently most of microfluidic devices feature 2D microfluidic networks.

1.5.1 Fabrication of planar microfluidic devices

Microfluidic devices used in research are mostly engineered by molding approaches based on polydimethylsiloxane (PDMS) due to a long list of key PDMS properties including biocompatibility, optical transparency, gas permeability and so on.^{28,29} The typical fabrication process consists of photolithography, replication and bonding (**Figure 1.6**). A silicon wafer is first spin coated with a thin film of photosensitive material (photoresist) and then exposed to UV light through a photomask containing defined micropatterns. Afterwards UV-exposed areas become either soluble or insoluble in a developer solution (a process termed development). Then pre-polymer of PDMS is cast against the silicon mold with patterned photoresist to generate a PDMS substrate that replicates the topography of the mold. Finally a PDMS substrate containing microchannel features is bonded with a blank PDMS slab or a cover glass to create a microfluidic device, where inlets and outlets can be made through punched holes.

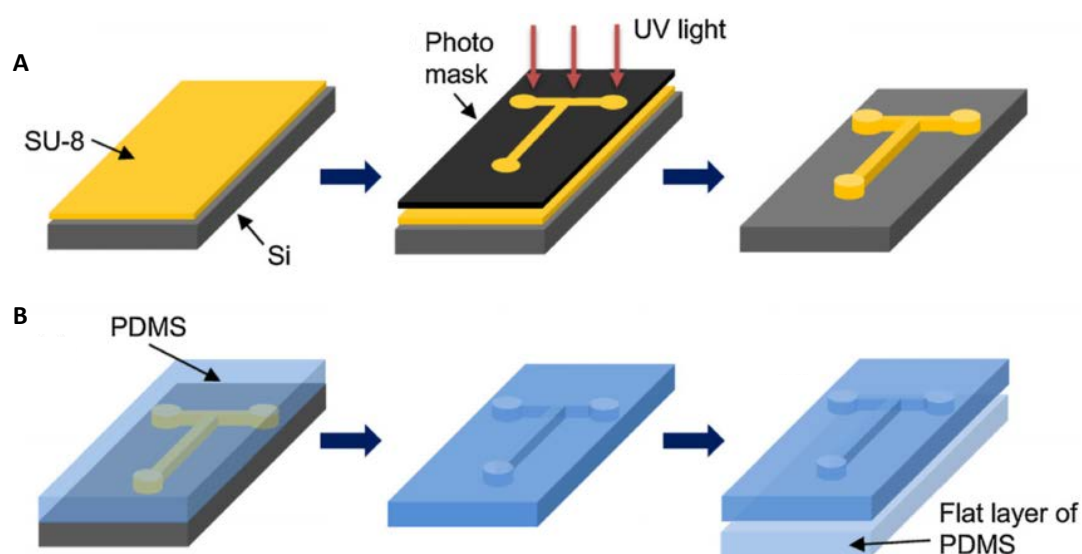


Figure 1.6 A schematic diagram showing the fabrication steps of PDMS microfluidic devices: mold fabrication based on photolithography (A) and replication/bonding process (B).³⁰ Adapted from ref. 30.

1.5.2 The unique physical features that the microscale provides

Due to the submillimeter length scale usually adopted in microfluidics, liquid flow is almost always laminar flow in microfluidic devices, allowing for highly predictable fluid dynamics, such as well controlled shear stress and diffusional rather than convective mixing among multiple laminar streams (**Figure 1.7A**).²⁷ As a result, highly controlled chemical gradients can be generated by laminar flow splitting and mixing in microfluidic channels, which has found use in many applications, such as high throughput drug screening and chemotaxis (**Figure 1.7B**).³¹

Similarly, compartmentalization can also be achieved by manipulation of laminar flows. For example, multiple hydrogel precursor solutions containing cells can be co-injected into “Y” shaped channels and subsequently gelled, resulting in separate but adjacent hydrogel compartments (**Figure 1.7C**).³² Alternatively, physical confining structures, such as micropillar arrays (**Figure 1.7D**) or porous membranes (**Figure 1.7E**), are widely utilized to realize compartmentalization in microfluidic devices.³³

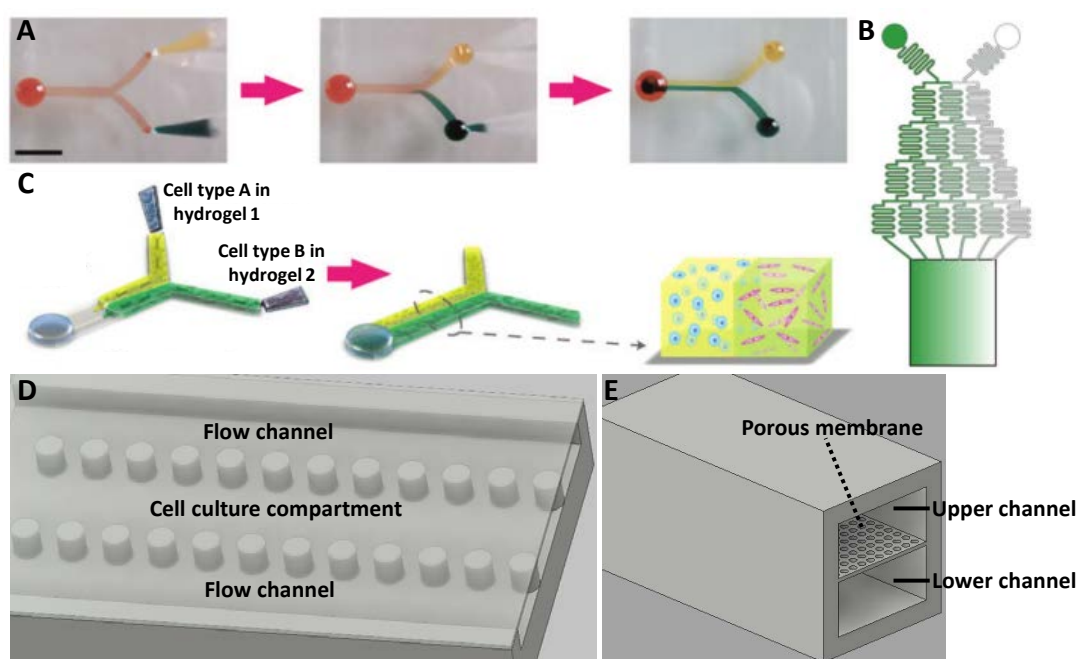


Figure 1.7 A) Yellow and green dyed solutions were pumped into Y-shaped PDMS microchannels by passive pumping to form parallel laminar streams.³² Scale bar represents 6 mm. B) A schematic diagram of microfluidic gradient generation. Green color indicates the spatial distribution of a potential soluble factor of interest in a microfluidic device.³⁴ C) A schematic diagram of loading and compartmentalization of cell-encapsulated hydrogels in a microfluidic device.³² Adapted from ref. 32 (A,C) and ref. 34 (B). D) A schematic diagram of an array of micropillars separating a single microfluidic channel into three compartments: a central cell culture compartment and two side media perfusion compartments. E) A schematic diagram of a microfluidic channel composed of upper and lower chambers sandwiching a porous membrane.

1.5.3 “Organs-on-chips”

The combination of laminar flow manipulation and compartmentalization enables spatiotemporal control over arrangements of multiple cell types, delivery of different soluble factors and physicochemical communications between differentiated environments in microfluidic cell cultures, which is very difficult, if not impossible, to achieve in conventional culture models.³⁵ Consequently, the emerging field of “organs-on-chips” have been continuously developed and shown to mimic important aspects of the biochemically dynamic characteristics *in vivo*. This approach has made it possible to engineer models of brain,^{36,37} nerve,^{38,39} heart,^{40,41} kidney,^{42,43} liver,^{44–51} blood vessels,^{52–57} breast,^{32,58,59} lung,⁶⁰ gut⁶¹ and so on (Figure 1.8A-C).^{62,63} As a step forward, “human/body-on-a-chip”, where different cell types representing different organs are cultured in a fluidically-linked fashion within a single chip, has been developed to mimic and investigate organ-organ interactions (Figure 1.8D).^{64,65} A microfluidic chip with cultures of multiple cell types representing the liver, tumor and marrow, was used to test the cytotoxic effect of Tegafur, a well-studied oral prodrug of an anti-cancer drug, 5-fluorouracil, and the results were consistent with previously published clinical test results. Although still in the conceptual phase, “human/body-on-a-chip” demonstrates the potential of such approach to test metabolism-dependent toxicity of drugs and subsequently to partially replace animal models for pre-clinical trials.⁶⁴

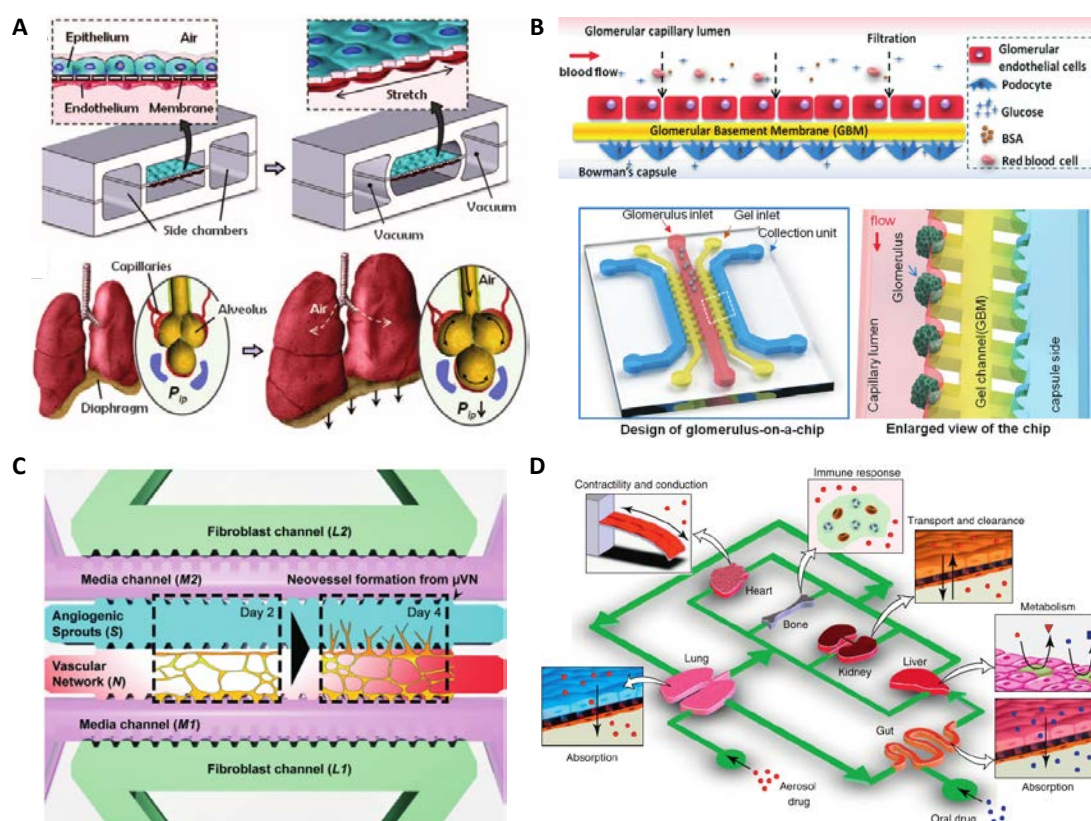


Figure 1.8 A) A schematic diagram of a “lung-on-a-chip” device using compartmentalized PDMS microchannels to form an alveolar-capillary barrier on a porous PDMS membrane coated with ECM.

By applying vacuum to the side chambers and subsequently causing mechanical stretching of the membrane, the device recreates physiological breathing movements of lungs.⁶⁰ B) A schematic diagram illustrating the glomerular filtration barrier in a kidney composed of glomerular endothelial cells, podocytes and a basement membrane that is selectively permeable to small molecules and water, as well as the design of a “glomerulus-on-a-chip” device composed of capillary channels, gel channels and collection channels, representing the capillary lumen, the glomerular basement membrane and Bowman’s capsule in glomerular microenvironment, respectively. The crescent microstructures were used to capture the glomerular microtissues.⁴³ C) A schematic diagram of a “microvessel-on-a-chip” device reconstituting the formation and expansion of microvascular networks in response to pro-angiogenic factors (fibroblast-secreted factors from fibroblast channels) and interstitial flow (between two media channels).⁶⁶ D) A schematic diagram of the “human/body-on-a-chip” concept. Cell cultures of different cell types representing different organs are integrated into a single device and linked by a fluidic circulatory system in a physiologically relevant manner to model complex organ-organ interactions, which can find many uses such as in systematically evaluating drug efficacy and toxicity.²⁹ Adapted from ref. 60 (A), ref. 43 (B), ref. 66 (C) and ref. 29 (D).

1.5.4 Limitations of planar microfluidic cell culture models

Despite various advantages that microfluidic cell culture models provide for better mimicking the dynamic characteristics of *in vivo* conditions, there are still many limitations that need to be addressed.

Firstly, the fabrication process of PDMS microfluidic devices usually involves substantial labor due to multiple non-automated steps, and requires sophisticated equipment such as clean room facilities (for photolithography), which is not easily accessible to general users. Such manufacturing hurdles make PDMS devices difficult to disseminate outside of the microfluidics community.²⁸ For example, despite the fact that microfluidic technologies are uniquely qualified for performing chemotaxis assays due to highly controlled fluidic dynamics at this scale, none of them has been routinely adopted in biological research and traditional methods such as “Transwell” assay developed in 1962 are still predominantly used by researchers for chemotaxis studies.²⁷

Secondly, PDMS microfluidic devices usually possess planar architectures due to the nature of their fabrication process. Limited 3D complexity can be achieved by stacking a series of patterned PDMS slabs, however, it is a tedious process where different layers must be carefully aligned and sealed (**Figure 1.9**).^{67,68} Although microfluidic devices can provide flows supplying oxygen and nutrients, which to some extent mimic native vascular networks, their planar configurations still limit their capability to fulfill vascularization in 3D. Instead, cellular components in microfluidic devices are either directly exposed to flow inside microchannels (which is not desired for most of cells *in vivo* except for endothelial cells) or flanked by flow in adjacent channels, while most *in vivo* tissues are perfused through an independent pervasive vascular network.

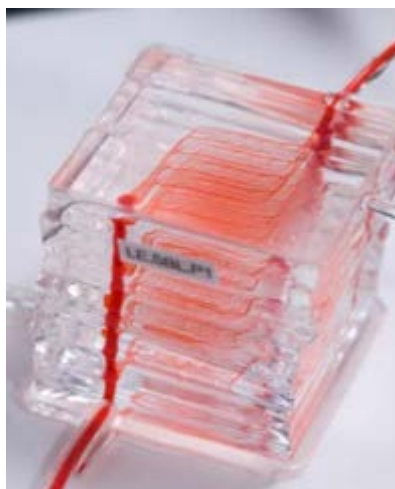


Figure 1.9 A) Stacking of 2D patterned PDMS slabs.⁶⁸ Adapted from ref. 68.

Thirdly, despite various advantages of using PDMS in microfluidic devices, it also possesses some major disadvantages. PDMS permits diffusion of compounds in vapor phase but not in the liquid phase.⁶⁹ Consequently, cells can only be cultured on PDMS but not within and extra structural elements such as micropillars or porous membranes have to be included to realize mass transport of soluble factors between different compartments. Furthermore, PDMS has been reported to deplete the transported media of low polarity compounds by absorption, which can be problematic for many applications.⁶⁹ As a result, other materials, such as thermoplastics,^{70,71} thermosets,⁷² and hydrogels,^{73–78} have been reported to manufacture PDMS-free microfluidic devices. Among them, microfluidic devices made of hydrogels are of particular interest due to their ability to recapitulate the properties of ECM, however, they are also often fabricated based on molding and replication process, which results in limited 3D complexity (**Figure 1.10**) and subsequently calls for new approaches to manufacturing true 3D hydrogel microfluidic devices.

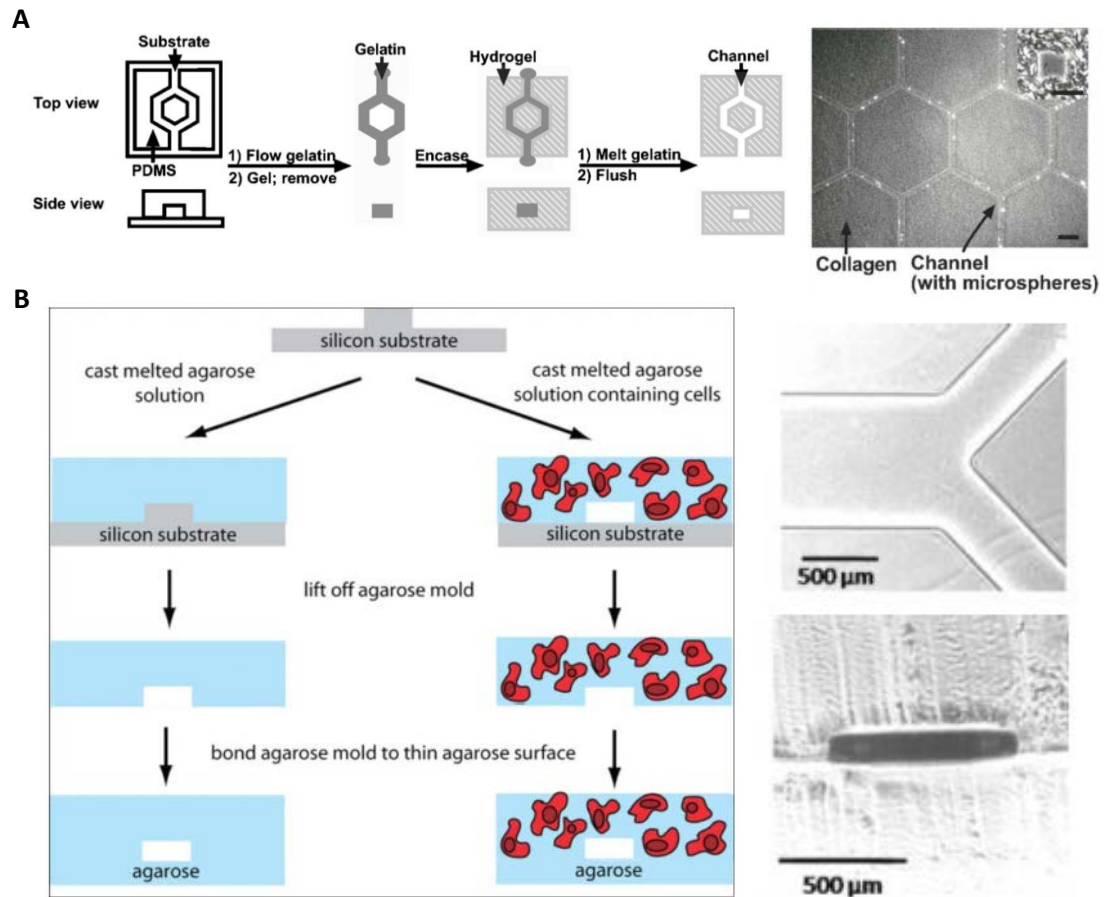


Figure 1.10 A) A schematic diagram of fabrication of microfluidic collagen gels using sacrificial gelatin molds and overlaid phase-contrast and fluorescence images (top view) of a hexagonal channel network within a matrix of collagen and perfused with fluorescent microbeads.⁷⁵ Insert is an image of a cross-section of a collagen channel. Scale bar represents 200 μm . B) A schematic diagram of fabrication of agarose microfluidic devices with or without embedded cells and phase contrast images (top and cross-sectional views) of a bifurcated channel in agarose hydrogel.⁷⁶ Adapted from ref. 75 (A) and ref. 76 (B).

Fortunately, the advent of 3D printing techniques offers new opportunities for addressing the abovementioned obstacles and producing next-generation *in vitro* 3D cell culture models.

1.6 3D printing based cell culture models

3D printing, or additive manufacturing has emerged as a versatile approach to constructing 3D objects. Unlike most conventional manufacturing techniques which remove material from a bulk piece of material such as milling and drilling, additive manufacturing works on adding materials in small volumes at a time or following a layer-by-layer fashion. 3D printing based cell culture models basically integrate conventional culture models with a computer-aided fabrication process that transforms digital designs into 3D objects without masks or molds and thus allows for precise control over both external (macroscale) and internal (microscale) structures of the models. Such automated fabrication process also

drives the design and innovation cycle. A new idea of design can be easily implemented by computer-aided design (CAD) that is accessible to a larger audience, while in case of conventional planar microfluidics each new design requires fabrication of a new photomask, which is time consuming and restricted to well-trained personnel.

Conventional culture models such as cell spheroids and cell-laden hydrogels are commonly used as modules to create 3D spatially defined constructs by 3D printing. Therefore, many materials used for conventional culture models can often be used for 3D printing as well.

As mentioned before, compared to conventional culture models, the key advantage of microfluidic culture models is the spatiotemporal control over model elements, such as spatial arrangement of different cell types, dynamic control of soluble factors including chemical gradients, nutrients and oxygen supply. However, the general planar nature of current microfluidic devices limits their further use as true 3D culture models at clinically relevant scale. 3D printing has the potential to achieve spatiotemporal control over model elements in a full 3D manner. There are many existing 3D printing techniques based on various mechanisms and none of them has complete superiority over others.

Regardless of the applications of constructed culture models, either as clinically useful replacements for damaged tissues/organs or as *in vitro* models for scientific studies such as drug development and *in vitro* disease modeling, vascularization in 3D is essential for maintaining healthy cultures. Since the construction of microfluidic channel networks is not inherently enabled by all 3D printing techniques, an overview of different 3D printing techniques will be given in the following sections while focus will be on those techniques that are most relevant for creating 3D models with embedded fluidic networks as vasculature.

Researchers have categorized different printing techniques based on materials, solidifying mechanism, machinery, *etc.* In this thesis, different techniques are grouped according to the form in which each technique delivers the material: droplet-based, powder-based, extrusion-based and stereolithography.

1.6.1 Droplet-based printing

Droplet-based printing, such as inkjet printing and laser-assisted printing, delivers materials in the form of droplets using various energy sources (thermal, electric, laser beam, acoustic or pneumatic mechanisms) onto a substrate (**Figure 1.11A**).⁷⁹ It offers great advantages such as simplicity and precise control on deposition of biomaterials with or without cells.⁷⁹ However, materials of low viscosity are usually used for inkjet printing due to the potential clogging of printhead nozzles and therefore when a dispensed droplet hits the substrate it tends to spread over, which makes it difficult to sustain the printed 3D structures.^{80,81} Although laser-assisted droplet-based printing can work with high viscosity liquids due to its nozzle-free approach, it suffers from high cost and bulky instrumentation.⁹ Overall, droplet-based printing techniques have limited 3D capabilities (**Figure 1.11B,C**).

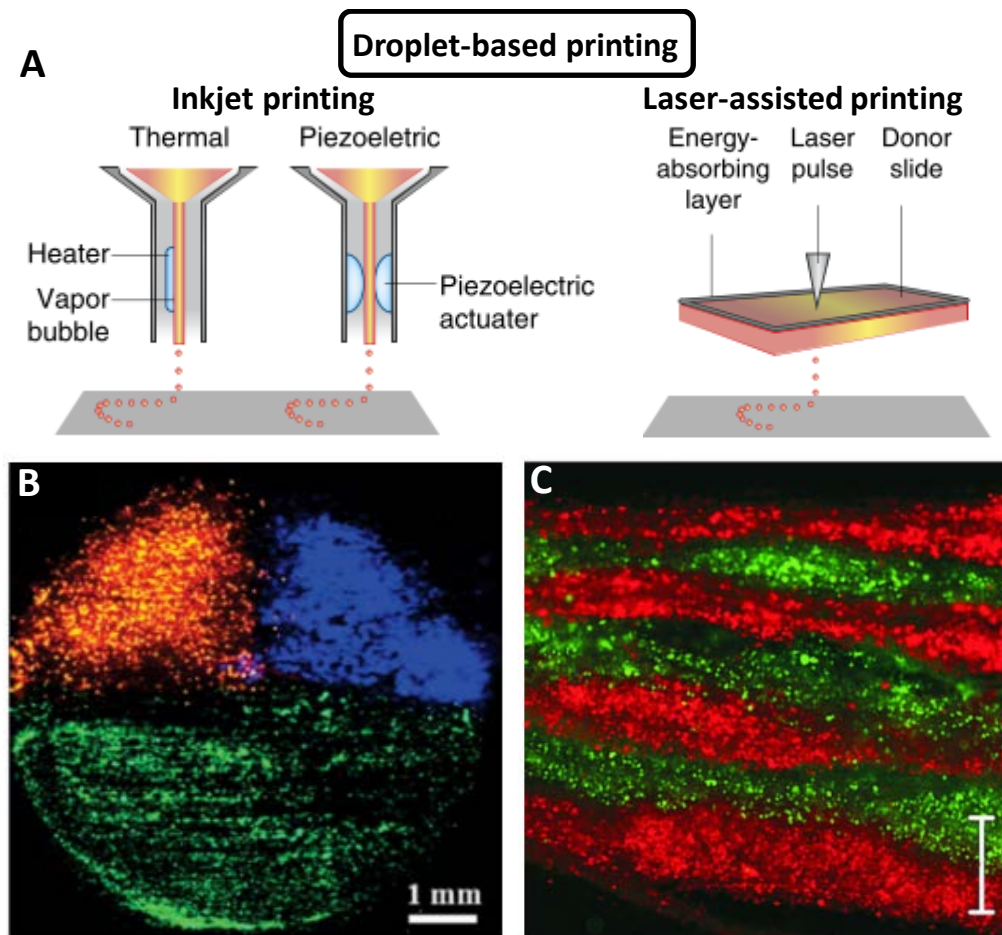


Figure 1.11 A) A schematic diagram of droplet-based printing techniques. Thermal inkjet printers electrically heat the printhead nozzle to produce air-pressure pulses to form droplets, whereas acoustic printers use pulses formed by piezoelectric or ultrasound pressure. Laser-assisted printers use lasers focused on an absorbing substrate to generate pressures that propel materials onto a collector substrate.⁸² B) Microscopic top views of a complete 3D multi-cell construct using inkjet printing. Three different types of cell were labeled with three different dyes.⁸³ C) Seven alternating color-layers of red and green stained cells printed by laser-assisted printing viewed in cross-section.⁸⁴ Scale bar represents 500 μm . Adapted from ref. 82 (A), ref. 83 (B) and ref. 84 (C).

1.6.2 Powder-based printing

Powder-based printing works on the fusion of powders, which can be induced by laser sintering or a liquid binder that bonds adjacent powder particles together. The general printing process can be described in the following steps (**Figure 1.12A**): 1) the powder supply platform is lifted and the fabrication platform is lowered one layer; 2) the roller spreads the powder into a thin layer; 3) a printhead nozzle that inkjets a liquid binder (similar to droplet-based printing) or a high-power laser scanning system selectively fuses powder particles together based on a computer-aided design (CAD) pattern; 4) cycling the above steps generates 3D structures.^{79,85} Since the non-bonded powders in each layer serve as structural supports, arbitrary 3D geometries can be created by powder-based printing. However, the resolution of powder-based printing is largely dependent on the powder particle size and it

is very difficult to completely remove excess powders from small cavities, which makes it unsuitable for manufacturing microfluidic channel networks (**Figure 1.12B**).²⁸

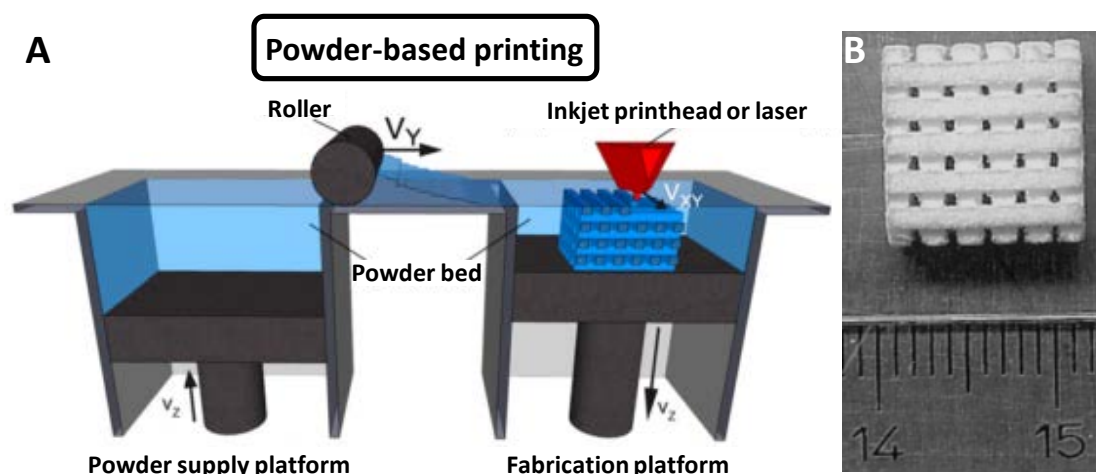


Figure 1.12 A) A schematic diagram of powder-based printing technique.⁸⁵ B) Top view of a 3D scaffold fabricated by powder-based printer with an inkjet printhead.⁸⁶ Adapted from ref. 85 (A) and ref. 86 (B).

1.6.3 Extrusion-based printing

Extrusion-based printing is similar to droplet-based printing. Instead of depositing a single droplet, extrusion-based printing can dispense uninterrupted cylindrical filaments of viscous liquids by applying a continuous force (**Figure 1.13A**).⁸¹ Because of the continuous deposition of filaments, extrusion-based printing provides better structural integrity during rapid fabrication compared to droplet-based printing. However, it is unsuitable for printing elements of dots.⁸⁷

A wide range of materials can be used for extrusion-based printing. The two most commonly used are thermoplastics and shear-thinning hydrogels. Extrusion printing of thermoplastics is usually termed fused deposition modeling (FDM), where thermoplastic filaments are heated to their molten state, extruded from a printhead nozzle and instantly solidified onto a cool substrate without any additional crosslinking requirement. Degradable biomaterials such as poly(caprolactone) (PCL) and poly(lactic acid) (PLA) have been printed using FDM for hard tissue engineering applications (**Figure 1.13B**).⁷⁹ However, due to the high temperature usually adopted in FDM, this technique is not cell compatible and therefore it is often used to create scaffolds that can be seeded with cells post-fabrication or molds that can be cast against using cell-laden biomaterials.

Hydrogels possessing shear-thinning behavior can be printed without elevated temperature. When they are exposed to shear stress passing through the printhead nozzles, the resultant decreased viscosity makes them behave like liquid and hence become extrudable. Once extruded and upon removal of shear stress, the increased viscosity enables them to stay in shape. Due to its mild operating condition, cells and biomaterials can be

simultaneously printed by simply loading cells into hydrogels, a process usually termed bioprinting.^{9,10,19,79,82,88} Furthermore, by implementing multiple printhead nozzles, different types of cells and biomaterials can be spatially deposited at desired positions (**Figure 1.13C**). Such versatility makes extrusion-based printing currently the most widely used approach for bioprinting.¹⁰

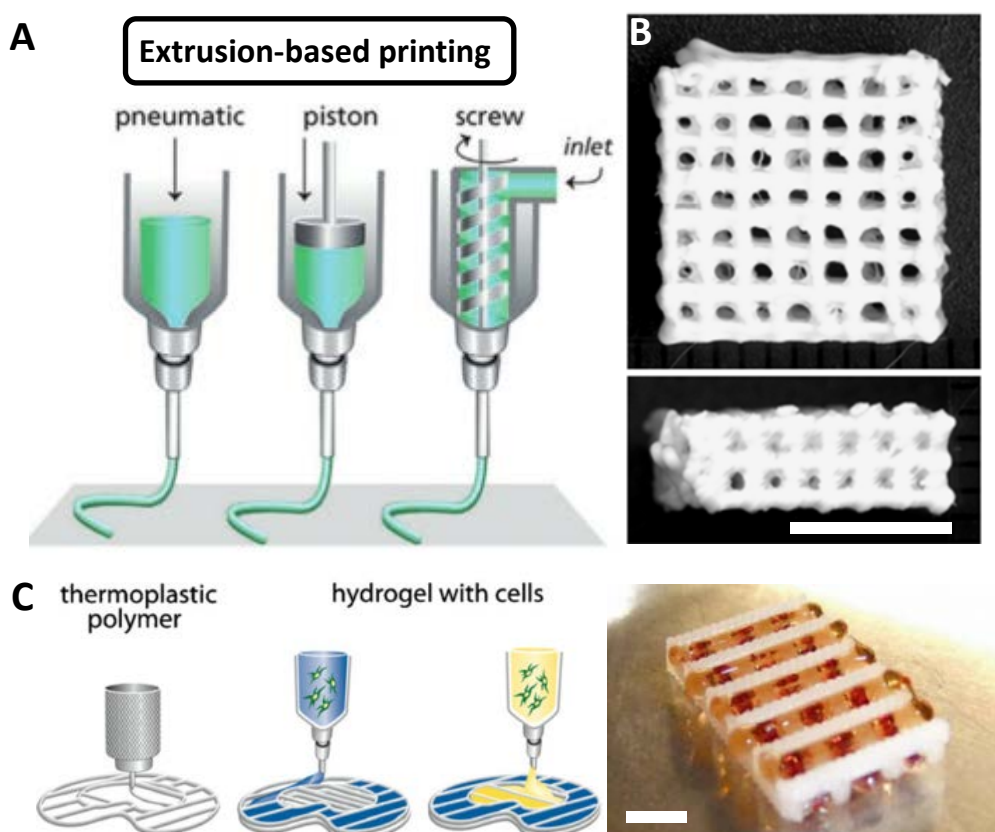


Figure 1.13 A) A schematic diagram of extrusion-based printing techniques.⁸¹ B) A PLA scaffold printed by fused deposition modeling.⁸⁹ Scale bar represents 5 mm. C) A schematic of diagram of a multi-printhead extrusion printer capable of printing different biomaterials as well as different cell types (left) and an actual printed construct (right) using this approach composed of a thermal plastic material (PCL) and two types of alginate hydrogels stained with different fluorescent beads.⁹⁰ Scale bar represents 2 mm. Adapted from ref. 81 (A), ref. 89 (B) and ref. 90 (C).

Although extrusion-based printing provides better structural integrity than droplet-based printing, an additional crosslinking/hardening process is usually required because extruded materials tend to fold or collapse under their own weight.⁹¹ Hence, direct extrusion printing of overhanging structures is still challenging and so far most 3D constructs demonstrated in extrusion printing have been rectilinear lattice architectures with limited topological complexity. This limitation has recently been overcome by extruding material into a support bath with particular rheological properties (**Figure 1.14A**).^{92–96} Printhead nozzles can move freely within the bath while deposited materials stay in place upon extrusion, thus leading to the construction of highly intricate architectures without any support structures (**Figure 1.14B**). However, upon the removal of support bath, it is difficult

to handle the remaining free-stranding structures that are usually composed of highly compliant materials such as hydrogels and therefore this technique has found limited use and applications so far other than the demonstration of constructing complex geometries.

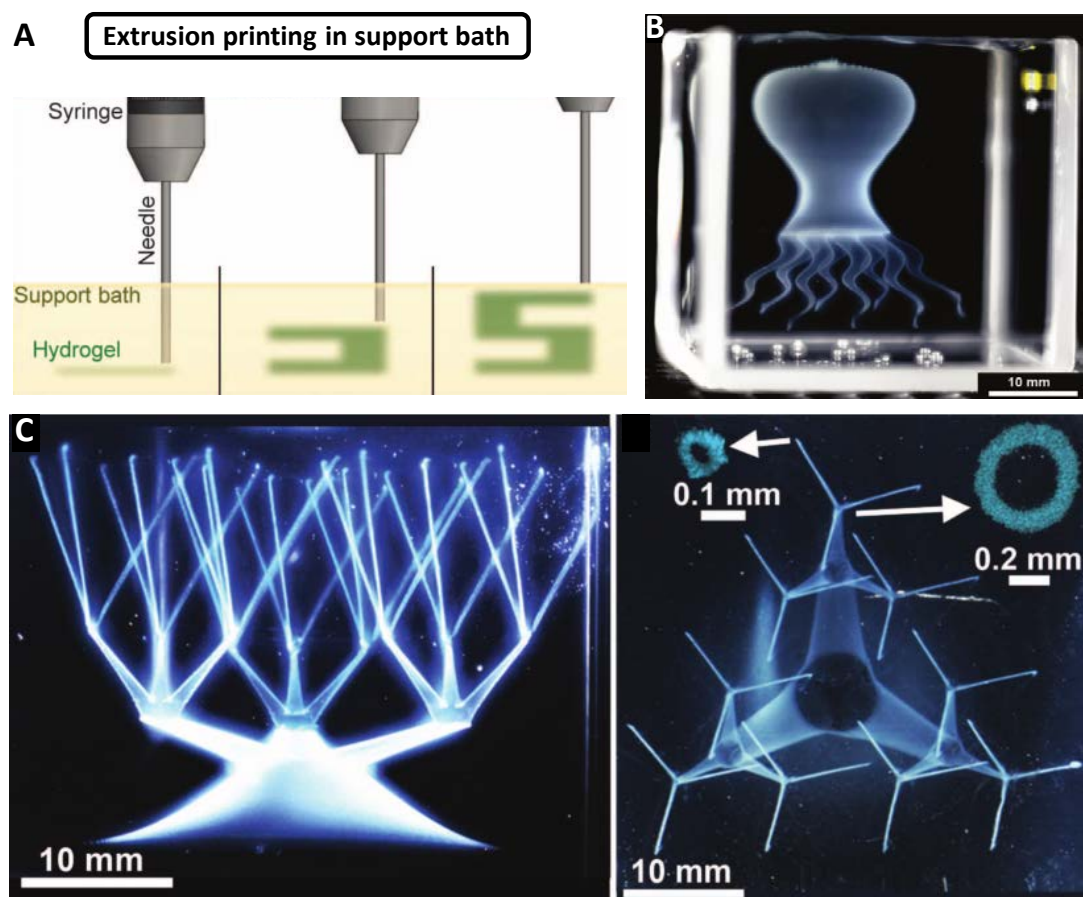


Figure 1.14 A) A schematic diagram of extrusion printing in a support bath.⁹² B) A thin-shell model octopus made of polyvinyl alcohol (PVA) hydrogel printed in a granular gel bath.⁹⁵ C) Side and top views of a continuous network of hollow vessels made of PVA hydrogel printed in a granular gel bath (inserts: confocal microscopy cross sections).⁹⁵ Adapted from ref. 92 (A) and ref. 95 (B,C).

Construction of fluidic networks is not inherently enabled by extrusion-based printing. However, with recent development extrusion-based printing has been used in printing vascular-like networks supporting thick tissue constructs either through direct or indirect approaches.

By applying a support bath (as previously mentioned) or a coaxial printhead nozzle configuration, hollow tubular structures can be directly printed using extrusion-based printing. Highly branched channel networks such as support-free arterial trees have been printed by extrusion printing in a support bath (**Figure 1.14C**).⁹⁵ Despite the intricate architectures, such approach can usually only print relatively large diameter channels ($\varnothing > 500 \mu\text{m}$) at comparatively low speeds, and has not yet been shown to produce directly perfusable constructs due to the difficulty in handling printed structures after the removal of support bath.^{92,93,95}

Alternatively, a coaxial extrusion configuration has been proposed to produce hollow tubular structures mimicking the blood vessels by delivering a pre-polymer solution such as aqueous alginate solutions in the sheath flow and a crosslinking solution such as calcium chloride in the core, where in situ crosslinking of the pre-polymer solution through the diffusion of crosslinkers occur upon extrusion to obtain hollow tubular structures (**Figure 1.15A**).^{97–111} Coaxial extrusion configuration has been almost exclusively applied to alginate/calcium hydrogels. Cells can be directly embedded in tubular structures by using cell-laden alginate (**Figure 1.15B**)^{103,106,107} or later included by embedding printed hollow tubes in other cell-laden matrices (**Figure 1.15C**).^{97,100} However, coaxial extrusion printing cannot print bifurcated channel structures since it has inherent limitations in connecting newly printed hollow tubular structures to already printed ones.

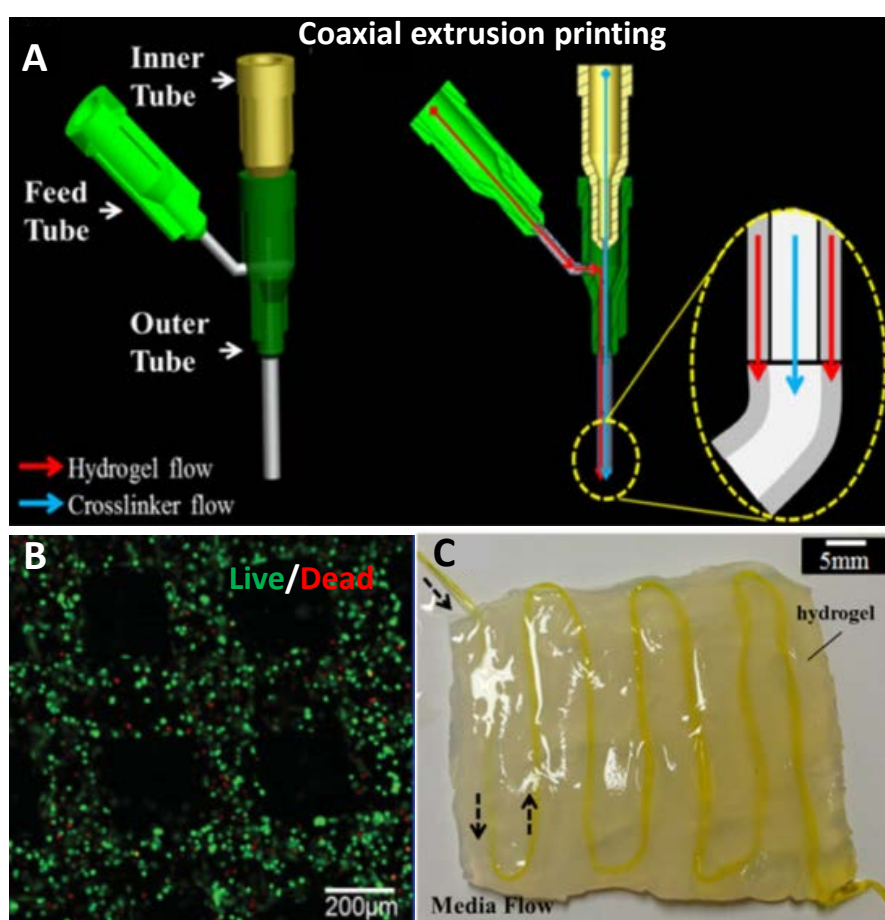


Figure 1.15 A) A schematic diagram of coaxial extrusion configuration.⁹⁸ B) Confocal live (green)/dead (red) staining of human umbilical vein endothelial cells (HUVECs) encapsulated in alginate/gelatin hydrogel tubular structures printed using coaxial configuration.¹⁰⁷ C) Alginate hollow tubes printed using coaxial configuration were embedded in bulk hydrogels.⁹⁸ Arrow indicates medium flow direction. Adapted from ref. 98 (A,C) and ref. 107 (B).

Fluidic channel networks can also be indirectly printed by extrusion-based printing when used in combination with sacrificial molding. Sacrificial filaments, such as carbohydrate glass,¹¹² gelatin,¹¹³ agarose¹¹⁴ and fugitive inks of Pluronics,^{115–117} are first extrusion printed and later cast into cell-laden hydrogels (**Figure 1.16**). Upon removal of those sacrificial

materials, fluidic channel networks are formed and subsequent perfusion of channels can maintain long-term cell viability in 3D cell cultures that exceed 1 cm in thickness.¹¹⁶

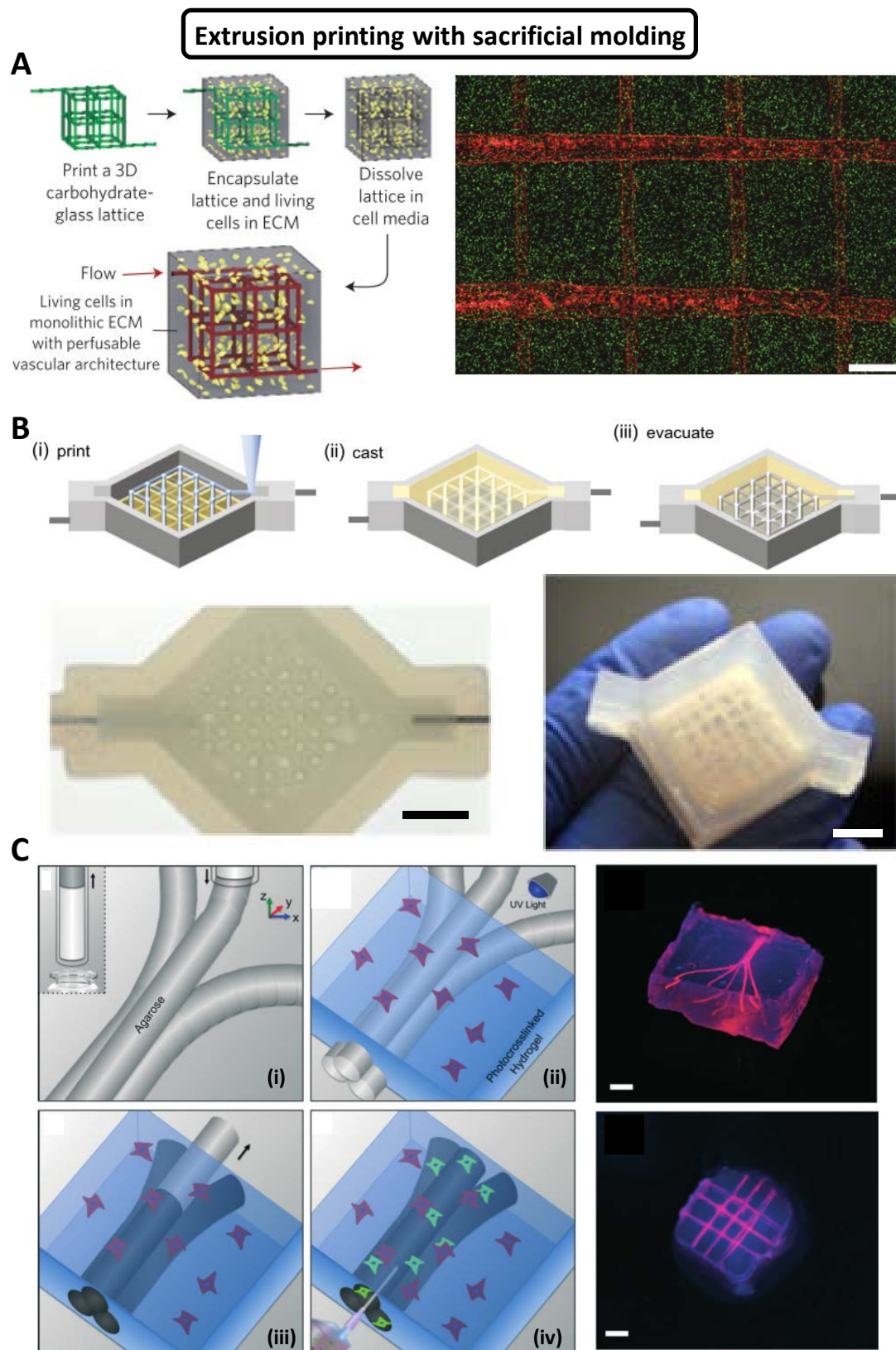


Figure 1.16 A) Sacrificial carbohydrate filaments were extrusion printed and then cast in a cell-laden fibrin hydrogel. The carbohydrate template was removed by dissolving it in culture medium. HUVECs

(red) were then seeded throughout the channel network by a single injection and fibroblasts (green) were encapsulated in fibrin gel.¹¹² Scale bar represents 1 mm. B) Sacrificial Pluronics filaments were first extrusion printed and then cast in a gelatin/fibrin hydrogel. The template was liquefied at low temperature (4 °C) and removed by vacuum suction. Top and perspective views of a printed construct containing lattice channel networks were shown in the photographs.¹¹⁶ Scale bar represents 5 mm. C) Sacrificial agarose filaments were first extrusion printed and then cast in a gelatin methacrylate (GelMA) hydrogel. The template was removed by pulling or vacuum suction. The resultant channel networks were perfused with a fluorescent microbead suspension (pink).¹¹⁴ Scale bar represents 3 mm. Adapted from ref. 112 (A), ref. 116 (B) and ref. 114 (C).

Construction of fluidic channel networks using extrusion-based printing either with coaxial configuration or in combination with sacrificial molding represents a major step forward in constructing 3D hydrogel microfluidics for next-generation cell culture models. However, most fluidic channel networks generated by such approach lack sufficient 3D complexity, a common problem observed in extrusion-based printing as previously discussed. Furthermore, the formed channel networks are ultimately defined only by the hydrogels used for cell encapsulation, which are usually highly compliant materials based on natural polymers such as alginate, collagen and gelatin. Such materials are very well suited for 3D cell culture with *in vivo*-like mechanical properties and the possibility for cell-induced matrix remodeling, but the resulting constructs' high compliance and limited long-term structural fidelity and stability challenge their use as self-contained perfusable *in vitro* systems.

1.6.4 Stereolithography

1.6.4.1 The basics of stereolithography

Stereolithography (SLA) is the technique used in this thesis and its working mechanism is fundamentally different from the techniques introduced previously. Stereolithography is considered to be the first commercialized 3D printing technique, developed by 3D systems in 1986.¹¹⁸ The manufacturing of 3D objects by stereolithography is based on the spatially controlled solidification of a liquid resin by photopolymerization following a layer-by-layer fashion. The originally proposed SLA apparatus is composed of: 1) a reservoir/vat to accommodate a liquid photocurable resin; 2) a light source and a system that subsequently controls the XY-movement of the light beam; 3) and finally a fabrication platform that printed structures can adhere to and that permits movement in the vertical direction and thus layer-by-layer fabrication (**Figure 1.17A**).⁸⁵ Before fabrication, a computer-aided design (CAD) file of a 3D object is sliced to generate a series of planar patterns and the spacing between each neighboring planar pattern is defined as slicing thickness (usually in the range of 25-100 µm) (**Figure 1.17B**).¹¹⁹ Smaller slicing thickness improves structural fidelity but also increases fabrication time by having more slices. The patterned light defined by the CAD design is first irradiated on the photosensitive resin surface to create a solid phase of the material. The first layer of polymerized materials is adhered to the fabrication platform, which provides support for structures as they are fabricated. The platform is then moved a

defined step height usually equivalent to the slicing thickness, allowing for polymerization of the subsequent layer (**Figure 1.17A**). This process is repeated until a 3D structure is completed.¹²⁰

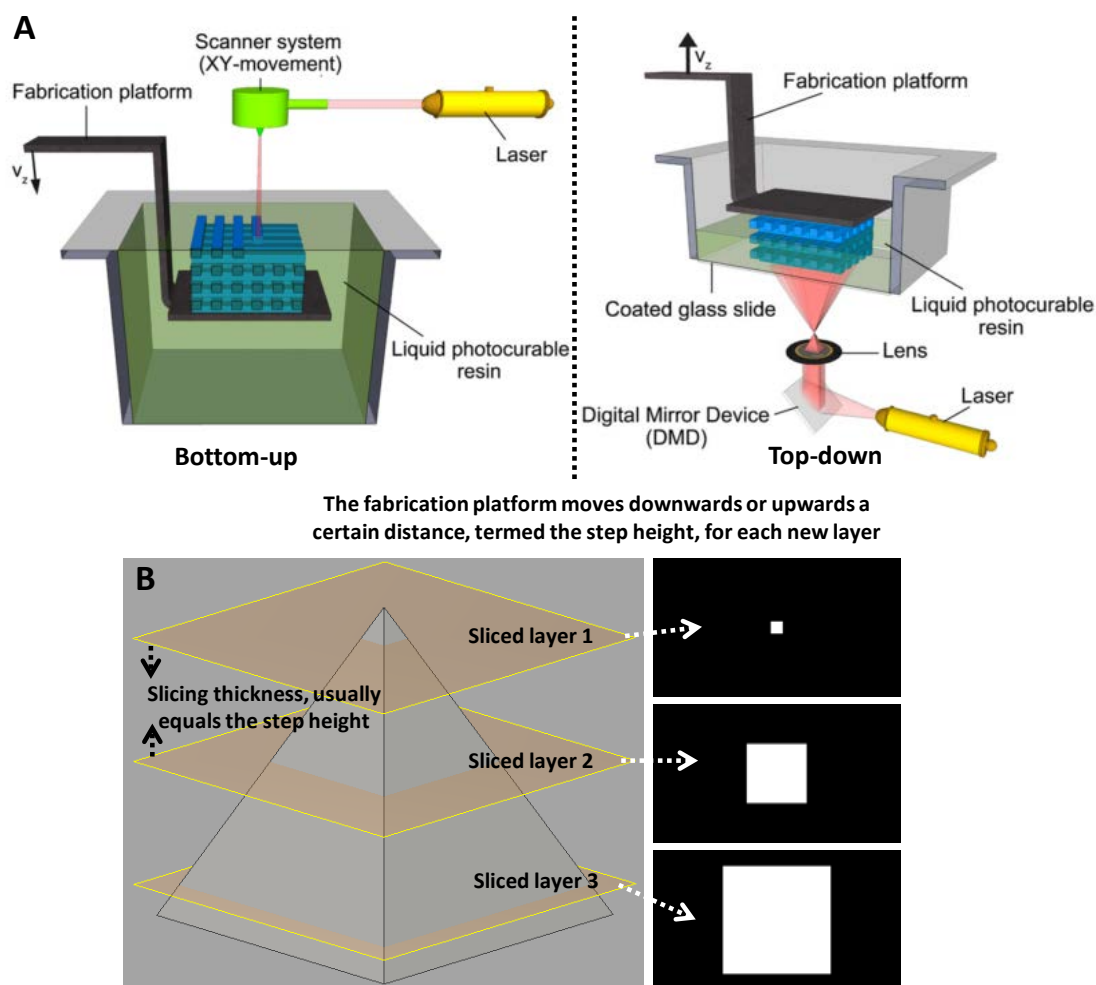


Figure 1.17 A) A schematic diagram of two different setups of SLA apparatus: bottom-up and top-down.⁸⁵ Adapted from ref. 85 (A). B) A schematic diagram of slicing a pyramid 3D CAD model into 3 layers.

In case of traditional SLA, each feature in a patterned layer is cured by sequential laser scanning (**Figure 1.17A**, left). However, an alternative form of SLA using digital light projection (DLP) has been recently developed and gained ever increasing interest to cure an entire layer at once (**Figure 1.17A**, right). This approach was first demonstrated with a liquid crystal display (LCD), but is now evolved into an inexpensive, commercially available projection system based on a digital micromirror device (DMD) functioning as dynamic pattern generator.¹²¹ Using a DLP, each patterned layer is sequentially projected onto the resin at once as a digital mask, which substantially reduces fabrication time compared to traditional laser scanning.

Depending on whether polymerization occurs at the top or the bottom surface of the vat, there are generally two setups for SLA: bottom-up and top-down (**Figure 1.17A**).^{28,85,121} In a so-called bottom-up setup, the resin is polymerized at its topmost surface interfacing with

air and accordingly the fabrication platform is translated downwards into the vat after each layer is printed. Conversely, in a top-down setup, the resin is cured at the bottom surface of the vat. After each layer is printed, the fabrication platform suspended upside down above the vat is moved upwards to allow for printing of subsequent layer. Usually, a laser scanning system adopts the bottom-up setup while a DLP system adopts the top-down approach. Although the bottom-up set was developed earlier and is still widely used in SLA, the more recent top-down setup offers certain advantages: 1) object height is not limited by the vat depth, which usually leads to less resin consumption; 2) since the polymerization, usually radical polymerization in SLA, takes place away from the liquid-air interface, therefore oxygen inhibition is minimized compared to the bottom-up setup and the resin can be cured faster. However, in the top-down setup, separating every newly formed layer from the vat bottom subjects the structure to larger mechanical forces compared to the bottom-up setup, which can damage fragile and delicate features, and therefore a non-adhesive bottom is usually required to facilitate gentle separation. In this thesis, a DMD based projection SLA with the top-down setup is utilized.

1.6.4.2 Resins used for stereolithography

Resins used for SLA consist of two essential components: monomer and photoinitiator. Often, they also contain non-reactive substances such as a diluent/solvent to reduce resin viscosity and a photoabsorber to control light penetration depth. When a photoinitiator is activated by light, the resultant reactive species polymerize the monomers to form a solid crosslinked polymer network.¹²² It should be noted that usually the photoinitiator is activated by absorbing a single photon in the UV or near UV range. However, in certain circumstance, a suitable photoinitiator can absorb two photons simultaneously through the irradiation with near-infrared femtosecond laser pulses of about 800 nm, causing them to act as one photon of 400 nm with equivalent energy to UV or near UV range. Unlike single photon absorption which is a linear excitation process, the probability of two-photon absorption is proportional to the square of the laser intensity and therefore the absorption rate decreases steeply with distance from the focal plane when using high numerical aperture objectives.^{85,123} Such non-linear excitation process triggers polymerization only in the focal point while other regions remain unaffected. Subsequently, two-photon polymerization (2PP) inherently gives 3D capability through direct laser writing within a liquid matrix and it can achieve submicron resolution, a resolution basically no other 3D printing techniques can achieve. However, due to the fact that polymerization only occurs at the focal point, 2PP is an extremely slow process. In addition, 2PP requires expensive and sophisticated equipment, and therefore it is not widely adopted for practical uses. So far, only single photon absorption has been adopted for SLA.

As different resins have different light absorption spectra, they have different light penetration depths thus different curing depths.^{121,122} Curing depth is the key characteristic of a resin formulation and hence very important for SLA process (**Figure 1.18**). The curing

depth should be slightly larger than the step height/slicing thickness adopted for the fabrication process so that mechanically stable structures can be printed through strong bonding between neighboring layers (unreacted functional groups in the preceding layer can polymerize with the subsequent layer).¹¹⁹ Curing depth should be well controlled so that light does not penetrate too deep into the preceding layer causing undesired features (light penetrates into and subsequently polymerizes the uncured resin). Specifically in case of printing fluidic channels, too large curing depth can cause overcuring of the channel ceiling into the channel volume, resulting in reduced vertical dimensions and sometimes even complete occlusion of the channel (**Figure 1.18A**). High photoinitiator concentration can be used to reduce curing depth by increasing the absorption of the resin, but also results in the formation of very brittle structures due to high crosslinking densities. Also, a high initiator concentration is not desired if the printed structures are intended for biomedical applications due to cytotoxicity of the initiator either on its own or its residues. Therefore, a non-reactive photoabsorber is commonly added to control light penetration depth, effectively restricting the polymerization to a thin layer. In addition to photoinitiator and photoabsorber, curing depth is also dependent on light dose and monomer concentration. Therefore, optimization of the resin formulation based on various parameters including monomer concentration, photoinitiator type and concentration, photoabsorber type and concentration and light dose, is crucial and far from trivial in order to fabricate constructs with both required structural stability and fidelity (especially in the vertical dimension). Resin optimization is one major part of this thesis.

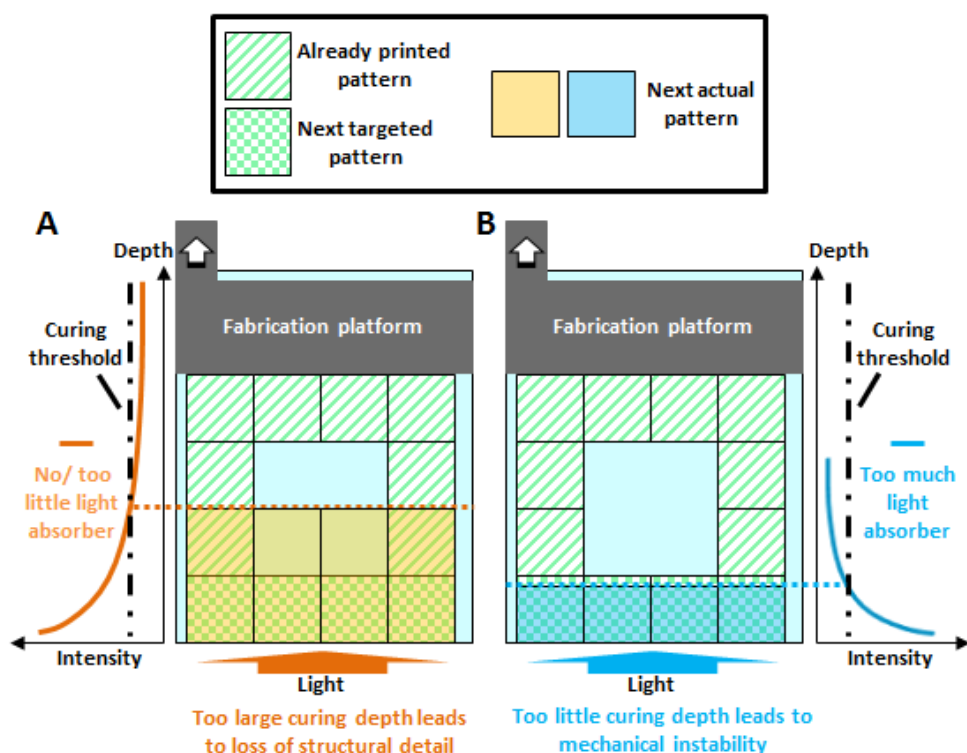


Figure 1.18 A,B) A schematic diagram shows how curing depth affects SLA printing. In (A), the resin contains no or too little photoabsorber so the light can penetrate way beyond the next targeted

pattern and subsequently polymerize the unreacted resin in the channel volume, resulting in the reduction of the vertical dimension of the channel. On the contrary, in (B), the resin contains too much photoabsorber, and therefore the curing depth is too little for the next printed layer to adhere to or form a strong bonding with the previous one, resulting in mechanically instable prints.

Conventional SLA resins are based on multi-functional acrylates and epoxies that are usually diluted by organic solvents, which predominantly produce glassy, rigid and brittle structures due to highly crosslinked networks. Such conventional resins are commonly used for industrial applications, but they are not suitable for biomedical applications. Recently, more and more materials such as acrylate functionalized polyester, polyether and naturally derived polymer have been developed for SLA use, which opens avenues for more applications. However, the limited number of resins that are commercially available for SLA is still considered one of the main limitations of the technique.¹¹⁹

1.6.4.3 Stereolithography in constructing cell culture models

Compared to extrusion-based printing, SLA has the potential for 3D freeform printing at high spatial resolution and high fabrication speed. So far, SLA is mainly used to fabricate cell scaffolds with repetitive internal pore architectures such as woodpile, hexagonal or gyroid geometries for hard tissue engineering such as bones (**Figure 1.19A-C**).^{124–141} Unlike scaffolds fabricated using conventional techniques such as gas foaming, microscale structural characteristics including porosity, pore interconnectivity, pore size and geometry are well defined in SLA printed constructs, which allows researchers to study structure-property relations. Furthermore, medical images obtained from magnetic resonance imaging (MRI) or computed tomography (CT) scans can be used to create 3D models *via* CAD and then printed by SLA to create structures with patient-specific anatomically correct geometries (**Figure 1.19D**).¹⁴² However, transport of oxygen and nutrients in such scaffolds is still only mediated by passive diffusion instead of perfusion by convective flow.

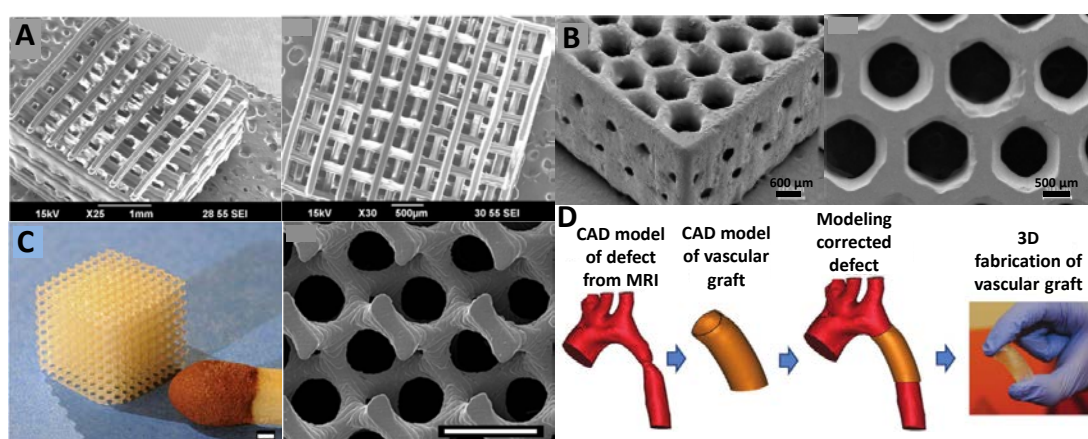


Figure 1.19 A) Scanning electron microscopic (SEM) images (perspective and top views) of a SLA printed scaffold with woodpile features using poly(propylene fumarate) (PPF).¹³³ B) SEM images (perspective and top views) of a SLA printed PPF scaffold with hexagonal pores.¹²⁶ Scale bars represent 600 (left) and 500 μm (right), respectively. C) A photographic image (perspective view) of a SLA printed scaffold

with gyroid architectures using polylactide and a SEM image (top view) of the same scaffold.¹²⁹ Scale bar represents 500 μm . D) A schematic diagram of design and fabrication process of 3D SLA printed graft to treat a coarctation of the aorta. Images obtained from medical imaging such as MRI are used to create a CAD model and a customized vascular graft is then SLA printed using PPF.¹⁴³ Adapted from ref. 133 (A), ref. 126 (B), ref. 129 (C) and ref. 143 (D).

Unlike extrusion-based printing, embedding fluidic channel networks within 3D constructs is inherently enabled by SLA and so far SLA has been used to print simple 3D branched networks (**Figure 1.20A**)¹⁴⁴ as well as to manufacture 3D microfluidic devices without cell culture components (**Figure 1.20B**).^{145,146} However, there have been very limited reports on construction of 3D structures with both embedded fluidic channel networks and cell culture units using SLA techniques.¹⁴⁷

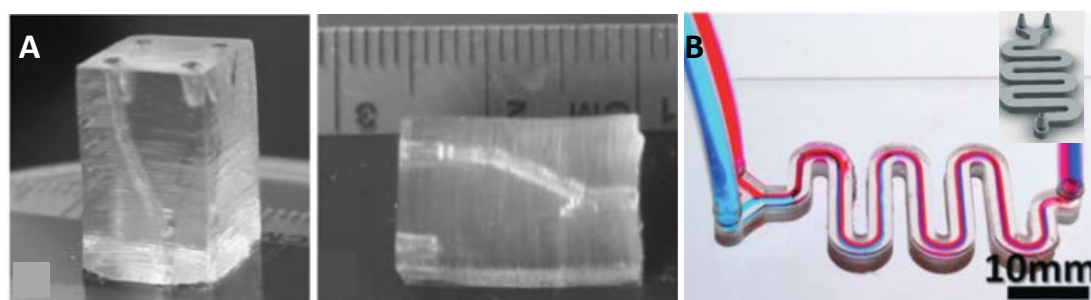


Figure 1.20 A) Photographic images (perspective and side views) of a PEG SLA printed scaffold embedded with a bifurcated channel network.¹⁴⁴ B) Photograph of a SLA printed laminar flow device.¹⁴⁸ The insert is the 3D model design. Adapted from ref. 144 (A) and ref. 148 (B).

1.6.4.4 Limitations of stereolithography

Although stereolithography has the potential for constructing complex 3D structures with high resolution and high fabrication speed, the use of SLA for *in vitro* cell culture models is still in its infancy due to several limitations.

Firstly, SLA is mostly restricted to the use of a single material, unlike extrusion-based printing where multiple materials can be easily deposited by simply implementing multiple printhead nozzles. To some extent, multi-material deposition can be achieved by manually switching to a new photopolymerizable resin between each layer fabrication.^{125,134,144,147,149–151} However, such process is labor-intensive and therefore the structures fabricated by this approach have limited 3D complexity and limited number of layers. In addition, manual operation between each layer also diminishes the point of using SLA as an automated rapid prototyping technique. Hence, to realize full capacity of multi-material printing in SLA requires sophisticated chemistries to allow for independent polymerizations of different monomers induced by different photoinitiators.

Secondly, although with optimized resin formulation cell encapsulation during fabrication with adequate cell viability has been achieved in SLA,^{138,144,147,149,152–155} the general toxicity of reactive species produced by photoinitiators requires the commonly adopted post-fabrication cell seeding strategy. In addition to the toxicity, cell settlement in

liquid resin during fabrication also poses a limitation that leads to uneven cell distribution. Some density gradient adjusting agents have been used to match the buoyant density of the cells with the resin to keep them suspended during fabrication.¹³⁸ However, such approach further complicates the process by requiring more optimizations. Furthermore, because SLA printed structures are mostly composed of irreversible chemically crosslinked polymer networks due to photopolymerization and therefore cannot be easily removed under mild and cell compatible conditions, SLA is usually not used in combination with sacrificial molding to create cell-laden structures with embedded fluidic channel networks.

Thirdly, the shortage of suitable resins hinders SLA's further applications towards constructing *in vitro* cell culture models. Since cells are usually post-fabrication seeded, 3D constructs with both embedded fluidic channel networks and cell culture compartments should be first created using SLA. However, currently most resins adopted for SLA are composed of rigid and non-diffusion-open materials. Because SLA cannot usually achieve a resolution that is seen in photolithography, microstructural elements (< 50 μm) such as micropillars cannot be easily printed to establish mass transport between culture compartments and fluidic channel networks,¹⁴⁸ unlike the case in conventional planar microfluidic cell culture models. Therefore, a diffusion-open material is in great demand. Although hydrogels fulfill the requirements, their generally low stiffness makes it difficult for SLA to print structures with both structural complexity and required mechanical stability, especially in the case of a top-down setup where structures are subject to larger mechanical forces as previously discussed. Hence, development of resins that can generate cell compatible, diffusion-open and mechanically stable culture units will be crucial to constructing advanced *in vitro* cell culture models using SLA techniques.

1.6.4.5 Summary

The main advantages and disadvantages of both SLA and extrusion-based printing (the most widely used technique for bioprinting) in constructing cell culture models with embedded vascular-like channel networks are summarized in **Table 1.1**. Stereolithography is chosen for this project due to its superior manufacturability in terms of high resolution and reproducibility compared to extrusion-based printing, thereby aiming to bridge the gap between high biological relevance usually sought in academia and robust production process usually sought in industry.

	Advantages	Disadvantages
Extrusion-based bioprinting	<ul style="list-style-type: none"> • Capability of simultaneous deposition of multiple materials and cell types • A larger selection of materials that can be used 	<ul style="list-style-type: none"> • Limited resolution and limited control of structural elements (can only print filament but not dots) • The formed channel networks are usually maintained by the same materials used for cell encapsulation after the removal of sacrificial template, namely highly compliant hydrogels and therefore lack long-term mechanical stability
SLA	<ul style="list-style-type: none"> • High resolution and 3D freeform printing capability • Direct embedding fluidic networks without sacrificial molding and flexibility of using different materials for vascularized constructs (mechanically stable) and cell encapsulation (compliant hydrogels) 	<ul style="list-style-type: none"> • Limited capability of deposition of multiple materials/cell types • Shortage of suitable resins for printing diffusion-open yet mechanically stable structures

Table 1.1 A summary of main advantages and disadvantages of extrusion-based bioprinting and stereolithography.

Chapter 2:

Hydrogel 3D microfluidics based on a modified commercial stereolithography printer

Initial studies were conducted on a commercial stereolithography printer (Perfactory micro, EnvisionTEC) that uses projection-based stereolithography adopting the top down setup and features a light source at 405 nm as well as a fixed step height of 25 μm (**Figure 2.1**). Detailed information regarding the printer can be found in the experimental section.

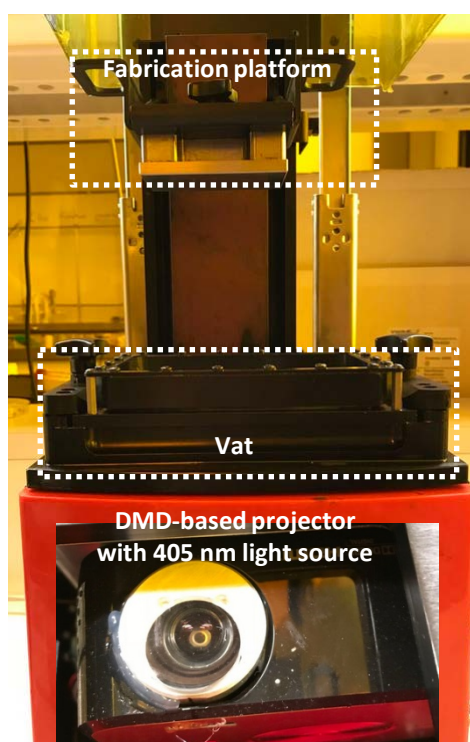


Figure 2.1 A photograph of our commercial stereolithography printer from EnvisionTEC company containing three major components: DMD-based projector with 405 nm light source, a resin vat and fabrication platform.

2.1 Choice of resin components

An aqueous pre-polymer solution composed of monomer, namely poly(ethylene glycol) diacrylate (PEGDA, M_n 700 g mol^{-1}), photoinitiator (lithium phenyl-2,4,6-trimethylbenzoylphosphine, LAP) and photoabsorber (quinoline yellow, QY) was employed for stereolithography. An aqueous resin is essential for perfusion structures since printed constructs will be eventually used in aqueous environment. Direct printing in aqueous solution minimizes structural changes caused by post-printing swelling. PEGDA (**Figure 2.2C**), a synthetic polymer, has commonly been used for cell encapsulation in biomedical studies due to its cell compatibility and non-fouling property. Cell encapsulation typically uses higher MW PEGDA ($M_n > 2000 \text{ g mol}^{-1}$) since the resulting more compliant hydrogels of lower cross-linking density permit cells to proliferate and migrate.^{156–158} Other researchers have used

undiluted highly crosslinked low MW PEGDA (M_n 250 g mol⁻¹) to manufacture microfluidic devices that resist swelling and are impermeable to water, and consequently impermeable to water-soluble nutrients.^{145,146,148} Our aim is to manufacture the perfusion chip unit surrounding the encapsulated cells, and we consequently selected a medium MW PEGDA to produce mechanically stable, yet diffusion-open, compliant hydrogel constructs.¹⁵⁹ In addition, PEGDA (M_n 700 g mol⁻¹) is commercially available at a much cheaper price compared to its analogues with higher MW, which is cost-efficient for large scale production using SLA that usually requires high resin consumption. The commercial printer has a light source at the wavelength of 405 nm, while the majority of photoinitiators is activated by UV light and not water soluble. A recently developed water soluble as well as cytocompatible photoinitiator, namely LAP, has been reported to absorb, albeit weakly, also in the visible range between 400 and 420 nm (**Figure 2.2A**).^{159,160} Thus it has been widely used for cell encapsulation in photopolymerizable hydrogels^{159,160} and is chosen as photoinitiator in this thesis. LAP has also been recently commercialized. QY, a commonly used food dye is selected in this thesis because of its high absorption around 405 nm (maximum absorption at 413 nm) (**Figure 2.2B**), excellent water solubility (in the form of its sulfonic acid sodium salt) and low cytotoxicity. The photoabsorber was used to limit the light penetration into the pre-polymer solution and thereby to achieve an optical Z resolution of the printer by matching its concentration to the printing process, as discussed previously.

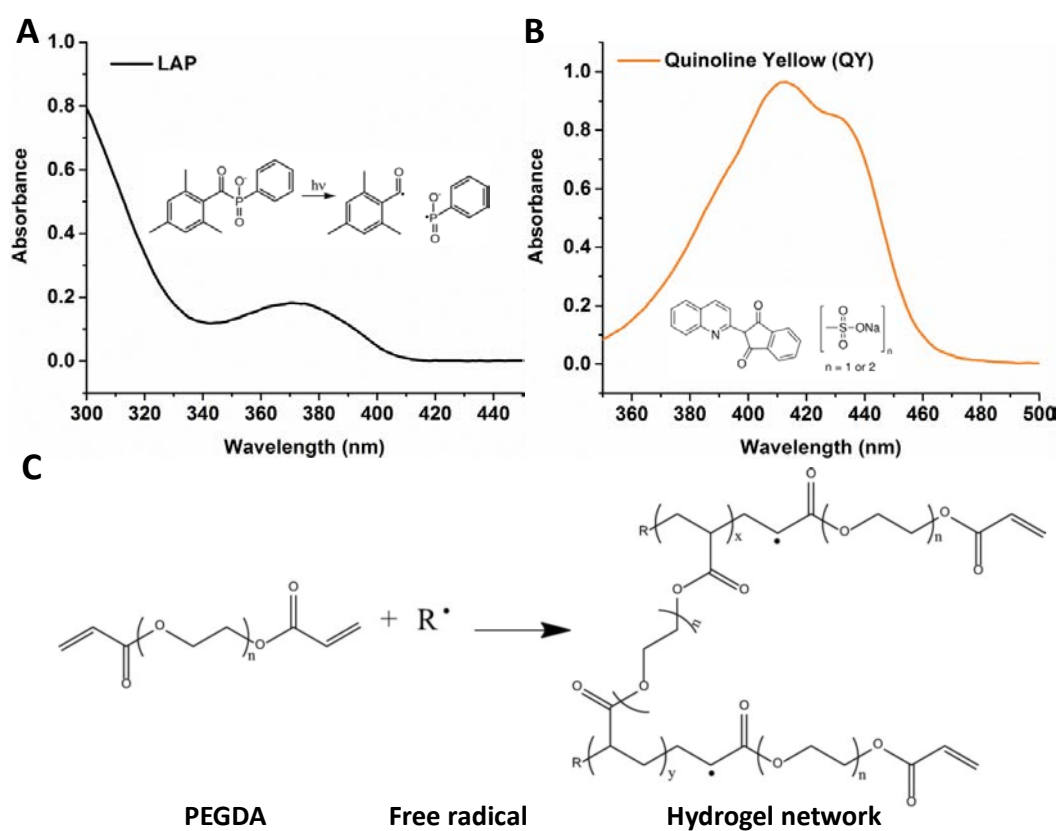


Figure 2.2 A) UV-Vis absorption spectrum of 200 µg/mL LAP in DI water in a quartz cuvette with 10 mm light path. B) UV-Vis absorption spectrum of 12 µg/mL QY in DI water in a quartz cuvette with 10 mm light path. C) A schematic diagram of radical polymerization of PEGDA to form hydrogel networks.

2.2 The effect of photoabsorber on resin curing depth

Based on the previous work in the group on photo-patterning PEGDA hydrogels using LAP and the same light exposure unit from the printer as a standard visible light projector, 200 mg/mL PEGDA, 5 mg/mL LAP and illumination times of 60 s were used as base experimental parameters for the remaining work.¹⁵⁹ As discussed before, photoabsorber is essential for stereolithography to achieve optimal vertical resolution. Therefore different concentrations of QY were first tested for their effect on the curing depth. Resins composed of 200 mg/mL PEGDA, 5 mg/mL LAP, 10 µg/mL fluorescein o-acrylate and different QY concentrations were placed in a multi-well plate containing a pre-treated cover slip (with methacrylate-functional silane) at the bottom of each well and then exposed to a projected light pattern for 60, 90 or 120 s. The thickness of formed gels was characterized using confocal microscopy to obtain the curing depth. Acrylate-functional fluorescein was added for the purpose of visualization. Although the absorption of fluorescein around 400 nm is very low, the addition of 100 µg/mL acrylate-functional fluorescein was found to inhibit polymerization while 1 µg/mL was not sufficient for visualization. A concentration of 10 µg/mL was then selected due to easy visualization and insignificant inhibitory effect on polymerization. The formed gels were chemically linked to the pre-treated cover slip due to coated methacrylate groups and thus can be easily handled for characterization. A grid pattern (for better contrast under the microscope) was projected to form pattern gels and the resultant gel thickness was measured using z-stack in confocal microscopy (**Figure 2.3A,B**). As shown in **Figure 2.3C**, the gel thickness decreased with increasing QY concentration as expected. Moreover, as shown in **Figure 2.3D**, with the same QY concentration, the gel thickness slightly increased with enhanced exposure time and remained the same after 90 s exposure. Therefore, 0.8 mg/mL QY, which gave a curing depth of 40 µm under 60 s exposure, was chosen as a starting concentration for 3D printing test to match the step height of 25 µm so strong bonding between neighboring layers can be achieved.

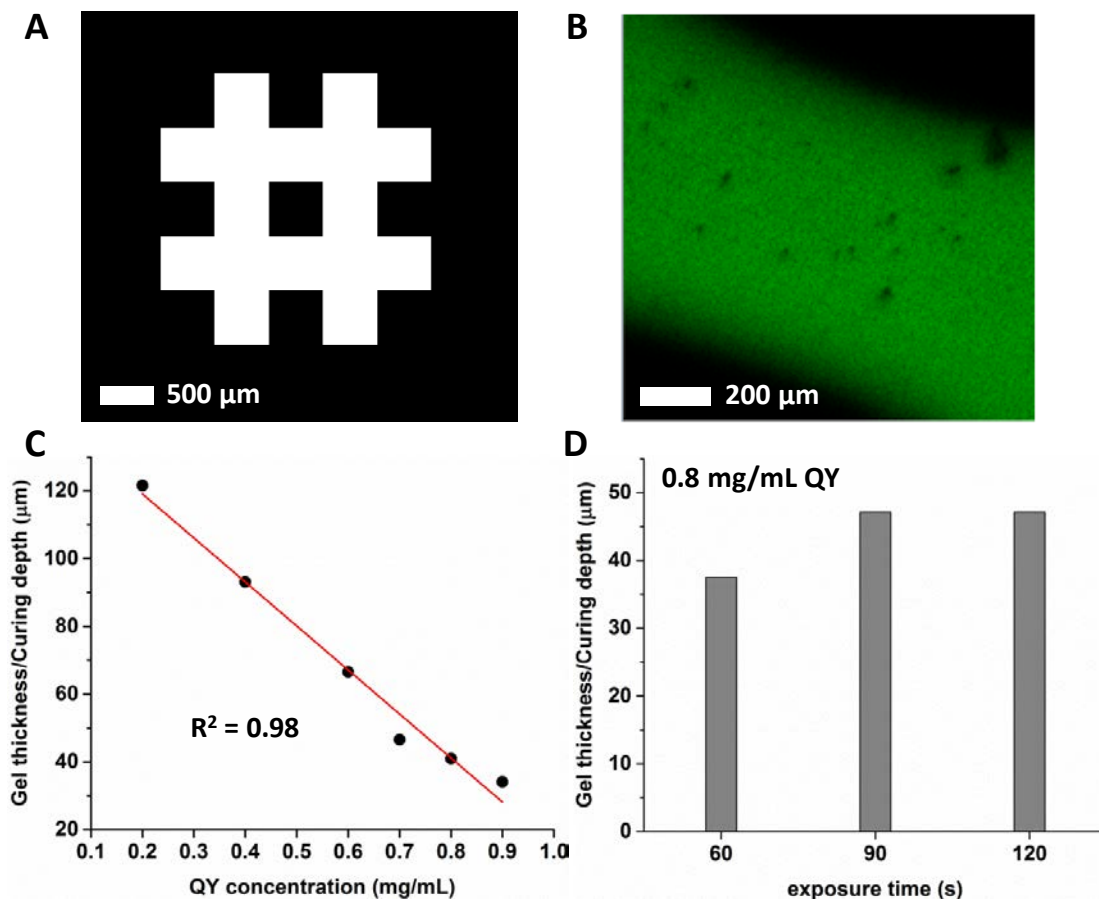


Figure 2.3 A) A grid pattern design used for patterning PEGDA hydrogels. B) A representative fluorescence microscopic image of the patterned gels. C) The thickness of the formed PEGDA hydrogels with different QY concentrations at an exposure time of 60 s. D) The thickness of the formed PEGDA hydrogels with different exposure times at a QY concentration of 0.8 mg/mL.

2.3 Modification of the commercial printer

The original vat requiring at least 20 mL resin for each print was oversized for preliminary test and therefore a home-made vat was made using a commercial fused deposition printer (Makerbot) in order to reduce resin consumption. A 3D printed PLA plate, a transparent poly(methyl methacrylate) (PMMA) slab and a 3D printed PLA well-shaped resin container ($\varnothing = 26$ mm, depth of 5 mm) were assembled to make the home-made vat using double-sided adhesive tapes (**Figure 2.4**). Since the reduced resin container cannot accommodate the original fabrication platform, a home-made fabrication platform was also made by assembling a 3D printed PLA hanger, a PMMA cylinder ($\varnothing = 10$ mm, height of 5 mm) and a pre-treated cover slip ($\varnothing = 20$ mm, thickness between 130 and 160 μm) to which printed gels adhere to using double-sided adhesive tapes (**Figure 2.4**). With the home-made vat, only 2 mL resin was required for each print. The fabrication platform needs to make its initial approach towards the bottom of the vat until it is close enough for the first layer to adhere to the cover slip. This initial approach process has been calibrated by the manufacturer and cannot be changed. Therefore, in order to calibrate the same process with our modified vat and fabrication platform, the height of the assembled home-made

fabrication platform was designed to be slightly smaller than the original platform, thus allowing for dimensional deviation stemming from the printing process. The optimal height was then calibrated by adjusting the number of adhesive tape layers (each glue layer about 150 μm thick) between the hanger and the PMMA cylinder until a cover slip placed at the bottom of the vat can be picked up by the cylinder with one adhesive tape layer on the other side when the platform makes its initial approach and afterwards return to its home position.

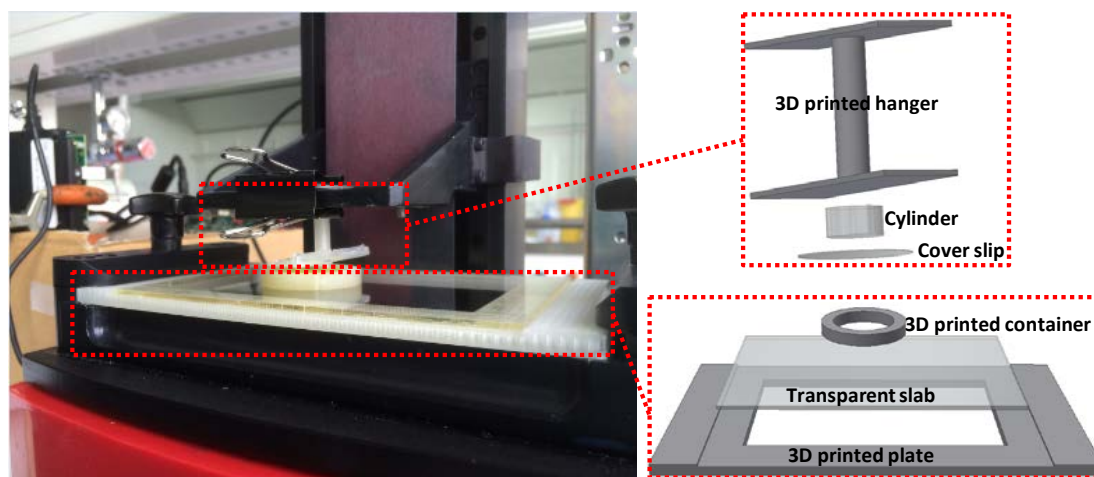


Figure 2.4 A photography of the modified commercial printer and a schematic diagram showing how the home-made vat and fabrication platform were built and assembled.

2.4 Optimization of printing configurations

2.4.1 The importance of a non-adhesive surface at the vat bottom

As mentioned before, a resin composed of 200 mg/mL PEGDA, 5 mg/mL LAP and 0.8 mg/mL QY, as well as exposure time of 60 s for each layer was first selected for 3D printing test. A simple block design (5 mm \times 5 mm \times 1.5 mm) was implemented. However, the printing was unsuccessful. The majority of the structure was found in the vat instead of attached to the cover slip after printing. It was suspected that the structure broke during the printing due to the larger mechanical force the structure was subject to during the separation of each new layer from the bottom. Thus a non-adhesive fluorinated ethylene propylene (FEP) foil (130 μm thick) was applied to the vat bottom to facilitate smooth release of each printed new layer from the vat. Consequently a hydrogel block was successfully printed with nothing left in the vat after printing. Later, a tapered design was implemented to further test the printability (**Figure 2.5A-C**). Since the top square is larger than the bottom one, each subsequent layer has some overhanging structures that are more subject to mechanical forces. Such a tapered structure is not easy to print using other 3D printing techniques without any structural support such as extrusion-based printing. However, with the applied non-adhesive foil, the tapered structure was successfully printed and characterized by confocal microscopy. The same resin formulation and exposure time was adopted, except for the addition of 10 $\mu\text{g/mL}$ acrylate fluorescein for visualization. As

shown in **Figure 2.5D**, the tapering angle matched well with the design. The same tapered structure was then printed with increasing QY concentrations and the highest QY concentration allowing for successful printing was found to be 1.2 mg/mL. Hence, QY concentration of 1.2 mg/mL was adopted for the remaining work so the optimal vertical resolution can be achieved with this resin formulation.

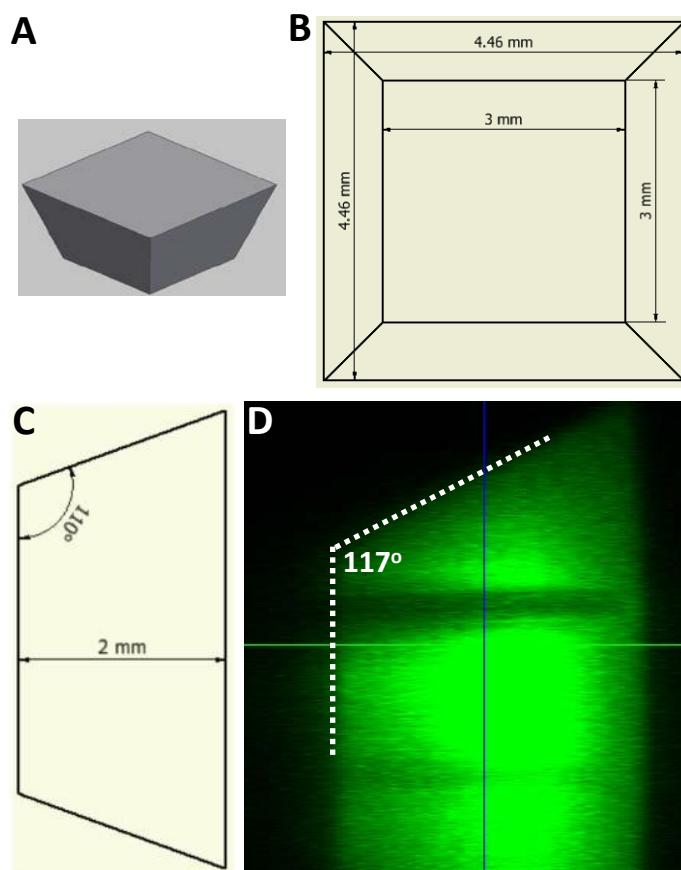


Figure 2.5 A) A 3D design of a tapered structure (perspective view). B) The orthographic view (top) of the design in (A). C) The orthographic view (side) of the design in (A). D) An orthogonal confocal fluorescence image (side view) of the printed tapered structure using 200 mg/mL PEGDA, 5 mg/mL LAP, 0.8 mg/mL QY and exposure time of 60 s.

2.4.2 The spatial printing resolution for microchannels

Since the aim of this project is to print hydrogel constructs with fluidic networks, the spatial resolution of the printer setup for printing microchannels was then explored. The concept of stereolithographic printing resolution is not consistently considered in the literature where the reported achievable spatial resolution often refers to the level of detail of open-surface features instead of closed channel structures.¹⁴⁸ The distinction between open and closed channels using stereolithography is important, since the structural fidelity of a closed rectangular channel largely depends on the light penetration depth into the pre-polymer solution (Z resolution), as previously discussed, while that of an open channel mainly depends on XY resolution pre-determined by the light exposure units of the printer. Therefore, a more relevant resolution assessment of channel structures is the deviation of

the printed dimensions of a sealed perfusable channel from the design dimensions.^{146,148} A series of rectangular channels were printed and both their horizontal and vertical dimensions were subsequently characterized using optical microscopy, as shown in **Figure 2.6**. Overall, the printed dimensions of microchannels matched the design ones well. The channels with 100 μm in vertical dimension were more poorly defined compared to the other channels, especially for 100 μm \times 100 μm channel which was almost occluded.

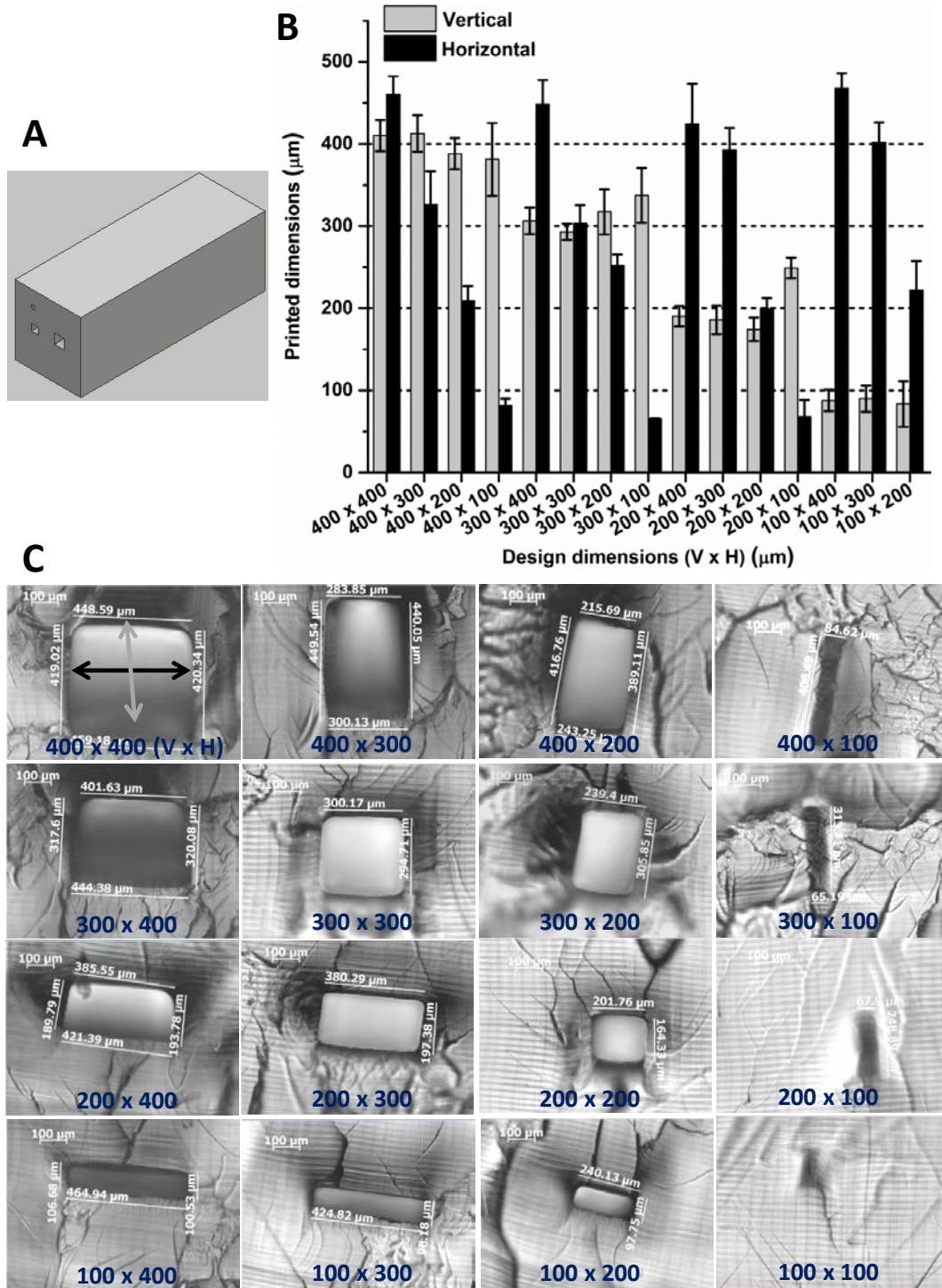


Figure 2.6 A) A representative 3D design of a block with microchannels of desired dimensions. B) Measured printed channel dimensions versus design dimensions (error bars show the standard

deviation, $n = 3$) from optical micrographs of cross-sections of a series of rectangular channels. The resin was composed of 200 mg/mL PEGDA, 5 mg/mL LAP and 1.2 mg/mL QY. The exposure time for each layer was 60 s. C) Representative optical micrographs of cross-sections of a series of rectangular channels.

Native vascular networks use circular channel geometries that lead to homogenous wall shear stress, in contrast to the variable wall shear stress in rectangular channels.¹⁶¹ Therefore, we also evaluated printing of circular geometries of decreasing diameters using the same resin formulation. The resulting channel cross-sections were less well-defined compared to rectangular channels, as shown in **Figure 2.7**. The channels adopted elliptic geometry and the channel with 100 μm diameter was almost occluded, similar to what was observed in rectangular channels.

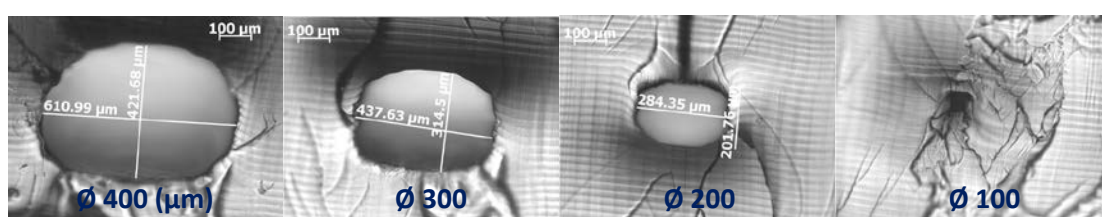


Figure 2.7 Representative optical micrographs of cross-sections of a series of printed circular microchannels with decreasing diameters from 400 μm to 100 μm . The resin was composed of 200 mg/mL PEGDA, 5 mg/mL LAP and 1.2 mg/mL QY. The exposure time for each layer was 60 s.

2.4.3 The effect of PEGDA concentration on printing

PEGDA concentration affects crosslinking density. Generally speaking, higher concentration leads to higher crosslinking density and thus produces stiffer hydrogels with better mechanical stability. However, higher crosslinking density also poses enhanced diffusion barrier for larger molecules such as proteins. Therefore, different PEGDA concentrations were tested for printing in order to determine the optimal PEGDA concentration that produces mechanical stable structures with the lowest crosslinking density as possible. Hydrogels constructs with rectangular microchannels were printed using 100, 150, 200 and 250 mg/mL PEGDA. As shown in **Figure 2.8**, channels printed using 100 and 150 mg/mL PEGDA were distorted compared to the ones printed using 200 and 250 mg/mL. Although the highest concentration tested so far (250 mg/mL) produces the most well-defined channel structures, 200 mg/mL is still selected for the remaining work due to its lower crosslinking density and thus minimized diffusion barrier for large molecules.

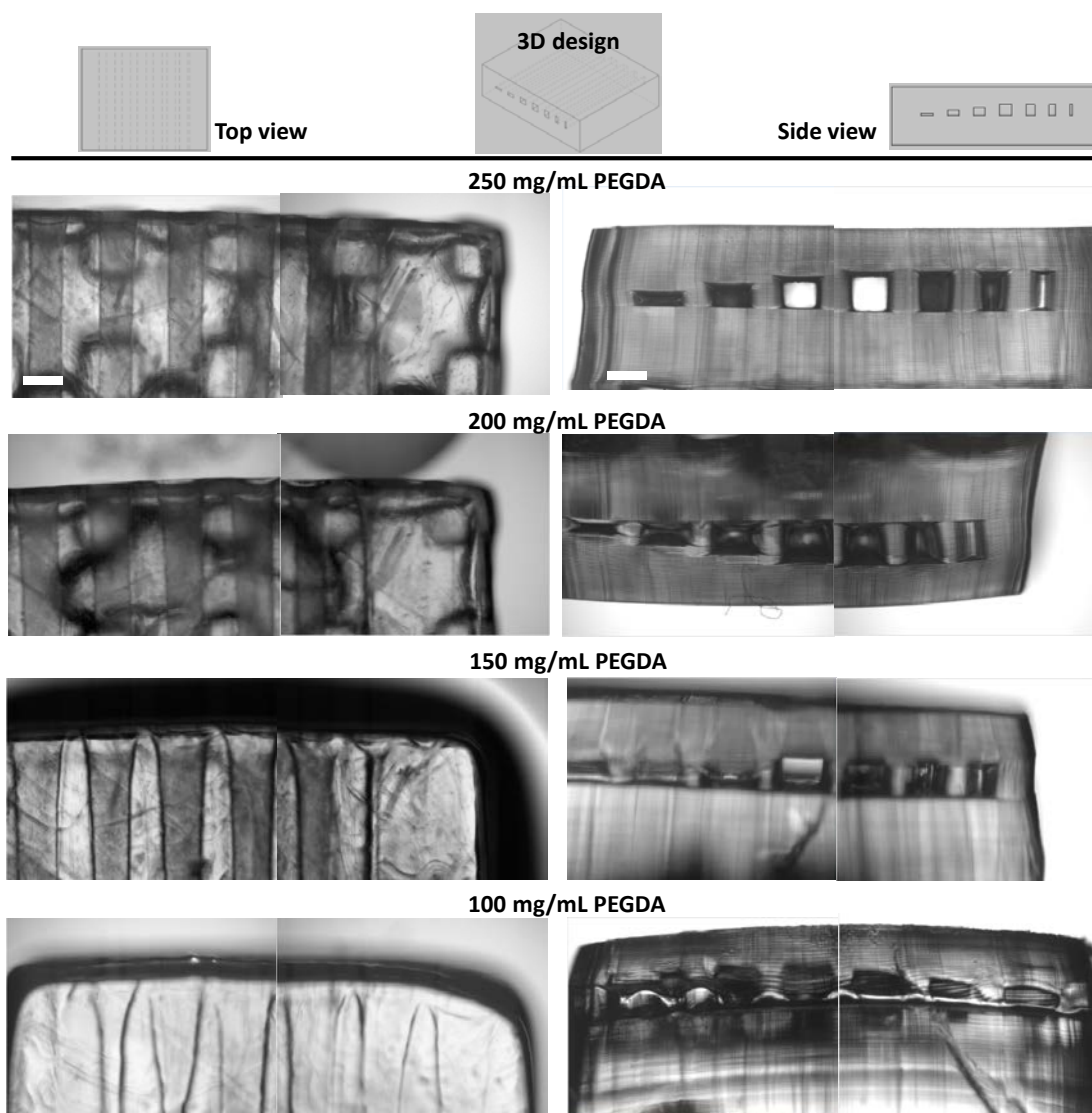


Figure 2.8 Optical micrographs (top and side views) of printed hydrogel blocks with microchannels of various sizes. The resin was composed of 100, 150, 200 or 250 mg/mL PEGDA, 5 mg/mL LAP and 1.2 mg/mL QY. The exposure time for each layer was 60 s. Scale bars represent 500 μm .

2.5 Cell compatibility of the printed PEGDA hydrogel constructs

Cell compatibility is a key characteristic of materials or constructs used for biomedical applications. Although all the resin components used in this thesis has shown to be cell compatible based on extensive previous studies,^{125,127,136,138,140,149,156–160,162–170} we investigated their combined effect on cell compatibility on SLA printed hydrogel sheets ($\varnothing = 11$ mm, thickness of 0.4 mm) (**Figure 2.9A**). An endothelial cell line (CRL-2922) was selected because ideally endothelial cells should line the synthetic vascular-like channel wall to regulate solute transport and facilitate homeostasis as in the *in vivo* situation.¹⁷¹ Prior to cell seeding, the surfaces of printed hydrogel sheets were coated with cell adhesive arginine-glycine-aspartic acid (RGD) peptides since pristine PEGDA hydrogels surfaces do not support cell attachment. Printed hydrogel sheets with unreacted acrylate groups on the surfaces were exposed to LAP-containing acrylated RGD peptide solution and subsequently to UV-A illumination.

Hydrogel sheets seeded with cells were visualized using phase contrast microscopy 8, 24 and 48 h after cell seeding. As shown in **Figure 2.9B**, after 8 h of incubation, most cells seeded on non-functionalized hydrogels remained spherical indicating minimal cell adhesion while cells seeded on functionalized hydrogels started to adhere and spread. After 48 h of incubation, cells seeded on non-functionalized hydrogels remained unattached while a notable increase in cell density was observed in functionalized hydrogels indicating cell proliferation. Therefore, SLA printed PEGDA hydrogels are cell compatible and can promote cell adhesion and proliferation with proper bio-functionalization.

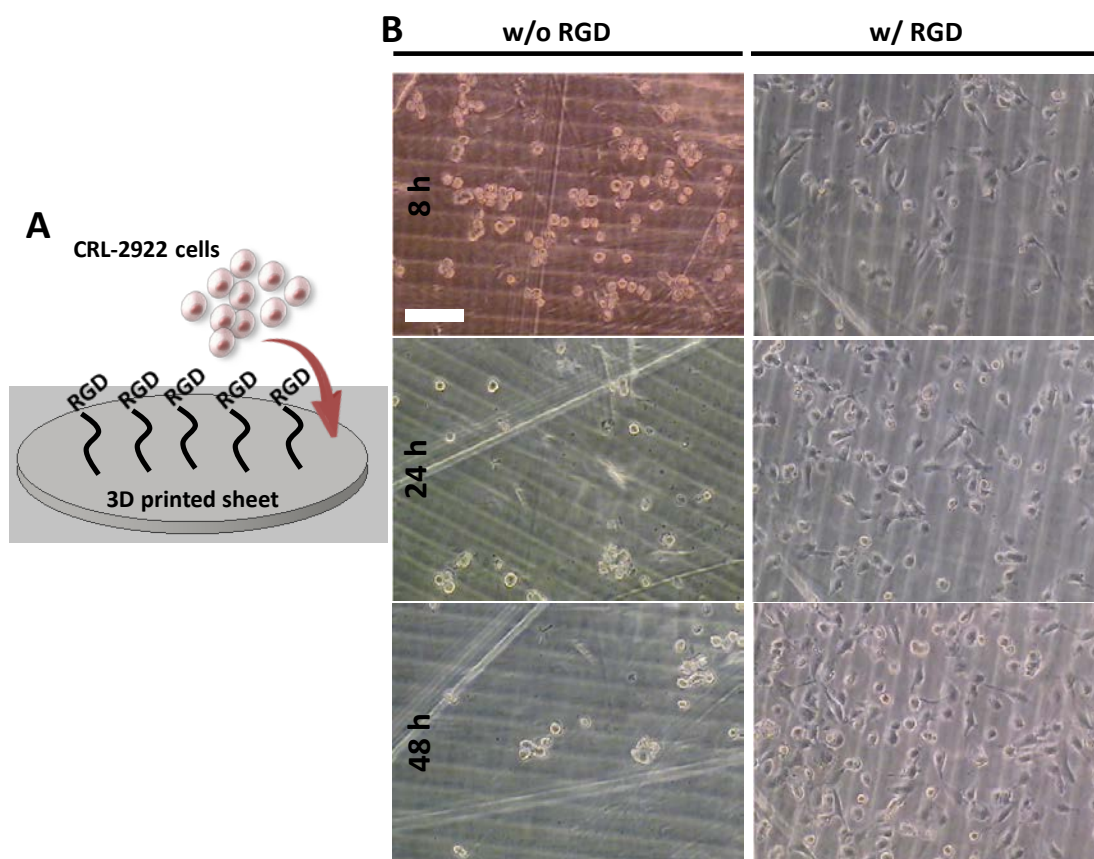


Figure 2.9 A) A schematic diagram illustrating CRL-2922 cells seeded on RGD peptides functionalized printed hydrogel sheets. The resin was composed of 200 mg/mL PEGDA, 5 mg/mL LAP and 1.2 mg/mL QY. The exposure time for each layer was 60 s. B) Phase contrast microscopic graphs of cells seeded on both functionalized and non-functionalized hydrogels sheets after 8, 24 and 48 h of incubation. Scale bar represents 100 μ m.

2.6 Perfusion of printed PEGDA microchannels with full 3D design freedom

First, we verified that printed fluidic channels can be perfused. Cylinder channel connectors (**Figure 2.10A**) were incorporated and printed in order to connect printed microchannels to external pumping. Blunt needles ($\phi_{\text{out}} = 0.8$ mm), fixed onto a micromanipulator device with two stages that allow for xyz multi-axis motion, was carefully aligned with printed channel connectors through a stereo microscope and subsequently inserted into the connectors (**Figure 2.10A**). The connector inner diameter (0.7 mm) was designed to be slightly smaller than the needle outer diameter to attempt a tight seal to the

needle. Perfusion tubing was then used to connect the needles and an external peristaltic pump. The whole perfusion setup is illustrated in **Figure 2.10B**. Successful perfusion of a single straight microchannel with a cross-section of $300\ \mu\text{m} \times 300\ \mu\text{m}$ was routinely observed.

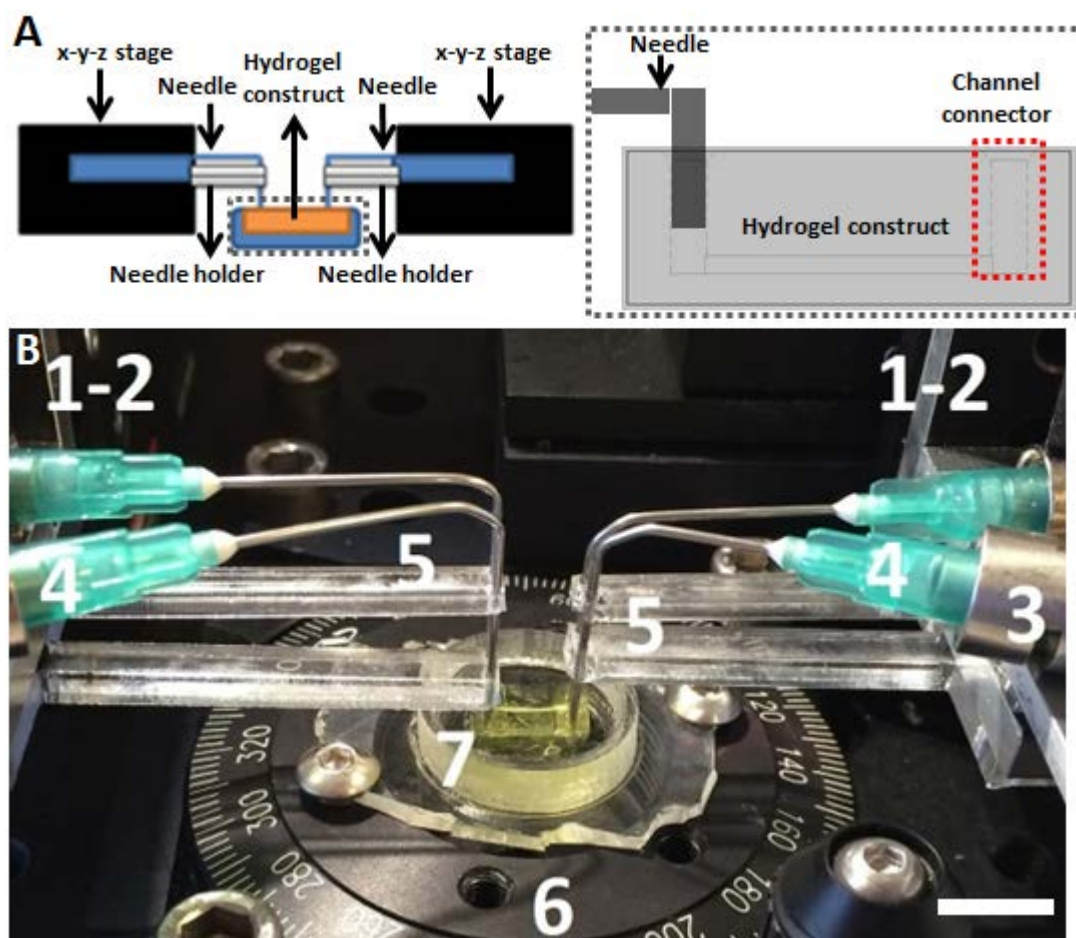


Figure 2.10 A) A schematic diagram illustrating the perfusion setup based on a micromanipulator device. B) A photograph of the perfusion setup composed of the following components: 1-2) the stages with metal joints; 3) the metal adapter connecting needles and perfusion tubing; 4) needles; 5) PMMA needle holder; 6) rotation stage that helps to align channel connector with needle; 7) hydrogel construct container. Scale bar represents 1 cm.

Secondly, a series of channel systems with the same square channel cross-section of $300\ \mu\text{m} \times 300\ \mu\text{m}$ yet increasing 3D complexity, namely single 1D channel, double 2D channel, triple 3D channel and spiral 3D channel (**Figure 2.11**), were printed and perfused using the same perfusion setup. However, it was found that in case of spiral channels, channel occlusion was constantly observed despite well-defined features of the printed $300\ \mu\text{m} \times 300\ \mu\text{m}$ channels as previously showed. A larger channel cross-section ($400\ \mu\text{m} \times 400\ \mu\text{m}$) was then implemented and afterwards the spiral channels were successfully perfused. These results show that perfusable channels with full 3D design freedom are easily accessible by our approach, which is difficult to achieve using other 3D printing techniques such as

extrusion-based printing. However, there was much room left for further resin optimization to achieve better vertical resolution.

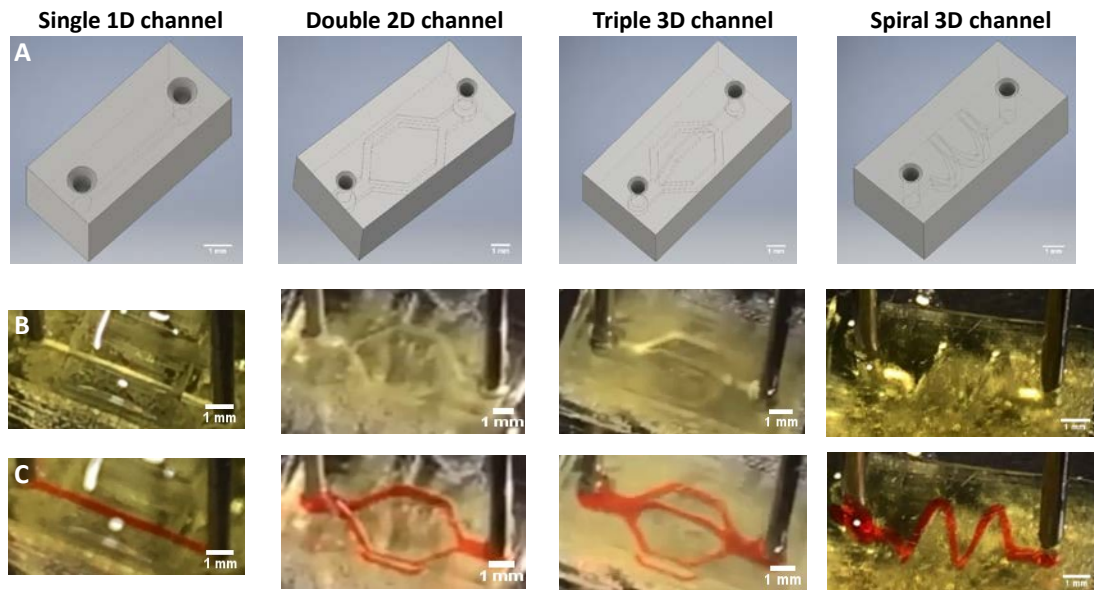


Figure 2.11 A-C) Channel system designs of increasing 3D complexity ($400\ \mu\text{m} \times 450\ \mu\text{m}$ channel cross-section for triple 3D channel and $400\ \mu\text{m} \times 400\ \mu\text{m}$ for the rest of channels) before (B) and after (C) perfusion using red dyed liquid. The resin was composed of 200 mg/mL PEGDA, 5 mg/mL LAP and 1.2 mg/mL QY. The exposure time for each layer was 60 s.

It should be noted that in case of triple 3D channel system, more than often only the two horizontal channels were perfused when all the three channels had the same square channel cross-section ($400\ \mu\text{m} \times 400\ \mu\text{m}$) (**Figure 2.12A**). We suspected this was due to the higher fluidic resistance in the upwards and downwards sloped channel segments caused by reduced channel dimensions during printing. Fluidic resistance in microchannels can be calculated using the formula:

$$R = \frac{12\mu L}{wh^3F} \text{ (rectangular geometry) and } R = \frac{8\mu L}{\pi r^4} \text{ (circular geometry)}$$

where R is fluidic resistance, μ is fluid viscosity, L is the channel length, w and h are the width and height of the rectangular channel, respectively, F represents a geometric form factor related to the rectangular shape and r is the channel radius.^{12,172} Based on the formula, channel cross-section size has a major effect on fluidic resistance. The reduced channel dimensions caused by printing are due to the light penetration into the preceding layer, as discussed previously. The difference between the two horizontal channels and the vertical channel in case of the triple 3D channel system is that the vertical channel has a slope in vertical plane (**Figure 2.12B**). In case of the two horizontal channels, overcuring unreacted resin in the channel volume is mostly significant when the channel ceiling is printed (the last layer of a channel structure) while in case of the vertical channel it occurs in

every layer of the sloped part (**Figure 2.12C**). Therefore, more reduced channel dimensions in the vertical channel leads to higher fluidic resistance. The channel cross-section was then changed to $400\ \mu\text{m}$ (V) \times $450\ \mu\text{m}$ (H) to reduce the fluidic resistance and subsequently all the channels were perfused (**Figure 2.12B**).

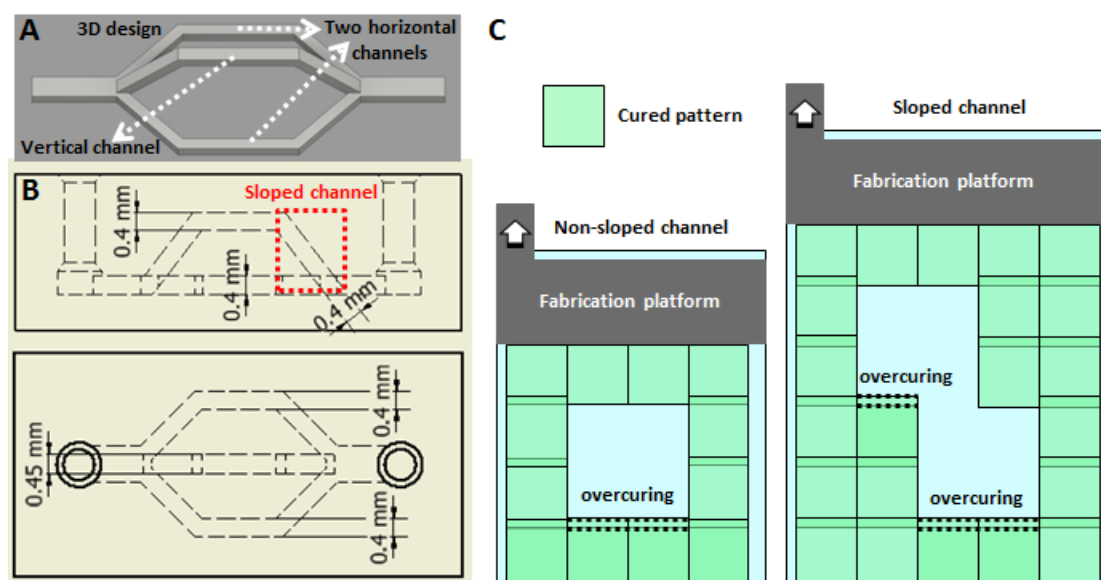


Figure 2.12 A,B) The 3D design of the triple 3D channel system (A) and orthographic views (top and side) of the design (B). C) A schematic diagram illustrating how printing causes more reduced channel dimensions in sloped channel structure. The dashed line indicates the curing that leads to reduced channel dimension.

The perfusion setup is generally adequate for testing if printed microchannels can be perfused. However, there are also some major limitations. Firstly, the equipment is cumbersome and thus makes it difficult to be utilized for perfusion cell culture studies which require a sterilized environment. Sterilization of the equipment with 70% ethanol and placing it in a laminar flow bench are not impossible but inconvenient. Secondly, once the alignment is done and the needles start to move downwards approaching the channel connectors, there is limited flexibility for movement in x-y plane and subsequently even slight misalignment could damage the structures when inserting the needles. Thirdly, due to the difficulty in perfectly aligning needles with channel connectors, leakage from the connectors is often observed shortly after the perfusion starts. Therefore, long-term, steady and leak-free perfusion cannot be easily achieved by this setup.

2.7 Conclusion

A commercial stereolithography printer was modified for hydrogel printing. An aqueous resin composed of PEGDA, LAP and QY was developed for SLA printing. Although microchannels with cross-section as small as $200\ \mu\text{m} \times 200\ \mu\text{m}$ can be printed, perfusion of printed microchannels can only be achieved in channels with larger cross-section (at least $300\ \mu\text{m} \times 300\ \mu\text{m}$). A perfusion setup based on a micromanipulator system was developed

and successful perfusion of a series of microchannels with increasing 3D complexity demonstrated that full 3D design freedom can be realized by our approach. We believe this demonstrated approach can serve as a useful guideline for researchers who want to work on stereolithographic 3D printing of hydrogels but do not have access to customized equipment and system. However, this proposed approach based on the commercial printer also poses some major limitations: 1) many experimental parameters are fixed by the manufacturer, such as fabrication platform step height and its initial approach distance, which offers limited flexibility; 2) the equipment for the perfusion setup is cumbersome and printed hydrogel constructs need to be carefully aligned with the needles, which is not easy.

2.8 Experimental section

2.8.1 Materials

Poly(ethylene glycol) diacrylate (M_n 700 g mol⁻¹, PEGDA) and Quinoline Yellow (QY) were acquired from Sigma-Aldrich and used as purchased.

2.8.2 LAP synthesis

LAP was synthesized based on a previously reported procedure.¹⁶⁰ Briefly, at room temperature and in a nitrogen atmosphere, 3.2 g of 2,4,6-trimethylbenzoyl chloride (TCI America) was added dropwise to an equimolar amount of continuously stirred dimethyl phenylphosphonite (3.0 g, Sigma-Aldrich). The reaction mixture was stirred overnight, followed by the addition of a four-fold excess of lithium bromide (6.1 g, Sigma-Aldrich) dissolved in 100 mL acetone. The reaction mixture was then heated to 50 °C. After about 10 min, a white solid precipitate formed. The mixture was cooled to room temperature and then filtered under vacuum. The filtrate was washed 3 times with acetone to remove unreacted lithium bromide, and the remaining solvent was removed in vacuum.

2.8.3 Pre-treatment of cover slip surfaces

The PEGDA hydrogels were printed onto pre-treated cover glasses for the purpose of easy handling, calling for prior chemical activation of the glass surface to secure the printed PEGDA to the glass support. The treatment was based on a previously reported procedure.¹⁷³ The circular cover glasses (Ø 20 mm, VWR) were first cleaned via plasma treatment to remove organic contaminants. The cleaned glasses were then soaked in a 2% v/v 3-(trimethoxysilyl)propyl methacrylate (Sigma-Aldrich) solution in 95% v/v ethanol/water (pH adjusted to 5 by acetic acid) for 10 min, washed with pure ethanol for 3 times, and eventually baked at 105 °C for another 10 min.

2.8.4 Projection stereolithography of PEGDA hydrogels

Stereolithographic printing used a commercial printer (EnvisionTEC, Perfactory family, Type HX300T-JE) containing a DMD device (43 µm projected pixel pitch) and using a 405-nm

LED light source. The power density at the vat bottom was 0.9 mW cm^{-2} as measured using a UV power meter (OAI 306, Optical Associates). The home-built vat and fabrication platform were printed using a fused deposition printer (MakerBot: Replicator 2). Pre-treated cover slips were mounted to the fabrication platform using double-sided adhesive tapes. Non-adhesive fluorinated ethylene propylene (FEP) foil ($130 \text{ }\mu\text{m}$ thick) was applied to the vat bottom to facilitate smooth release of each printed layer from the vat. 3D models were designed using Autodesk Inventor 2016 (Autodesk). The resulting design was sliced into a series of digital masks with a slicing thickness of $25 \text{ }\mu\text{m}$ using the Perfactory software that comes with the printer. The aqueous resin consisted of 200 mg mL^{-1} PEGDA, 5 mg mL^{-1} LAP and 1.2 mg mL^{-1} QY. After adding resin to the vat, the fabrication stage was moved close to the vat bottom. After the formation of the first layer, the stage was raised by $25 \text{ }\mu\text{m}$ for each additional digital mask exposure. Exposure time for each layer is 60 s . After printing, the object was immediately immersed in DI water for at least overnight to leach out remaining reagents and allowing it to reach its equilibrium swollen state prior to further use.

2.8.5 Perfusion of printed PEGDA microchannels

The two x-y-z stages were placed in front of each other with two fixed perpendicular metal joints on the sides, where the metal plate and needle holders were horizontally fixed. The metal adapters were fixed by metal clamps, connecting the stainless blunt needles (\varnothing_{out} 0.8 mm , Sterican) with perfusion tubing and external pump. The needles were bent 90° and subsequently were fixed onto the PMMA needle holders, keeping the needles stable and directly vertical. A rotation stage was placed between the two stages. The rotation stage made it easy to rotate the container where hydrogel constructs were placed so that channel connectors were aligned with the needles. A peristaltic pump (MasterFlex) was used. Printed constructs were fixated onto the container using double sided adhesive tapes, and the container filled with DI water. Aqueous solutions of red food dye (Dr. Oetker) were used as perfusion fluids. The tubing was pre-perfused with fluid to get rid of remaining air bubbles, and then the needles were inserted into the 3D printed channel connectors (\varnothing 0.7 mm). Pumping proceeded at a flow rate of $200 \text{ }\mu\text{L min}^{-1}$ and the channel perfusion was recorded by a phone camera.

2.8.6 Cell culture

CRL-2922 cells (ATCC) were cultured in Dulbecco's modified Eagle's medium with high glucose (DMEM, Biowest) supplemented with 10% v/v fetal bovine serum (FBS, Sigma-Aldrich) and 1% v/v penicillin-streptomycin (P/S, Sigma-Aldrich). Cell cultures were passaged following the vendors' manuals.

2.8.7 Cell compatibility of printed PEGDA hydrogel sheets

Circular hydrogel sheets (\varnothing 11 mm, 0.4 mm thick) were printed and immersed in DI water for 24 h with two intermediate changes of water bath to allow the leaching of unreacted reagents. The hydrogel sheets were then placed in a 24-well plate and 300 μ L aqueous solution of 0.2 mg mL⁻¹ acrylated RGD peptides and 5 mg mL⁻¹ LAP was added to each well, followed by 2 min of UV-A illumination (330-380 nm, peaking at 365 nm, 18 mW cm⁻²).¹⁷⁴ The reaction mixture was removed and the structures were washed with DI water 3 times. The hydrogel sheets were immersed in CRL-2922 culture medium containing 2% v/v P/S overnight to exchange the water in the hydrogel for culture medium. Before cell seeding, culture medium was removed and 500 μ L of cell suspension (4×10^4 cells mL⁻¹) was added to each well. Cells were then cultured at 37 °C in 5% CO₂ for 48 h. Each sample was then visualized by phase contrast microscopy. Images of cells were taken at 8, 24 and 48 h after cell seeding. Acrylated RGD peptides were synthesized by conjugating acrylic acid N-hydroxysuccinimide ester onto KG₆RGDS peptides (CASLO). Acrylic acid N-hydroxysuccinimide ester was first dissolved in dimethylformamide (DMF) at 4 mg mL⁻¹ and RGD peptides in NaHCO₃ buffer (50 mM, pH 8-8.5) at 1 mg mL⁻¹. 500 μ L of 4 mg mL⁻¹ acrylic acid N-hydroxysuccinimide ester solution in DMF was added dropwise to 1 mL of 1 mg mL⁻¹ RGD peptide solution. The mixture was stirred for 2 h and transferred to a 100-500 Da molecular weight cutoff (MWCO) dialysis tubing (Spectra/Por), and dialyzed against DI water for 48 h. The final product was obtained through lyophilization.

Chapter 3:

Hydrogel 3D microfluidics based on a home-built polychromatic stereolithography printer

The polychromatic printer was built by Prof. Niels B. Larsen (**Figure 3.1**). It has projected $13.68\text{ }\mu\text{m}$ pixel pitch, which is much better than the commercial printer ($43\text{ }\mu\text{m}$). The light exposure unit consists of a high power LED (light emitting diode) with multiple wavelengths, namely 365 nm and 450 nm , which has the potential for true multi-material SLA printing based on independent photopolymerization through different wavelengths. The printing process is controlled using custom written MATLAB code that synchronizes digital mask exposure on the DMD, light exposure, and fabrication stage movement via a linear stage. Such automated process based on programming code gives much flexibility in adjusting several experimental parameters according to resin performance, such as step height/slicing thickness. Detailed information regarding the home-built printer can be found in the experimental section.

Based on the experience gained from printing PEGDA hydrogels using the commercial printer, the resin optimization for the home-built printer was conducted following similar procedures. However, due to the wavelength change regarding the light exposure unit, adjustments were made accordingly.

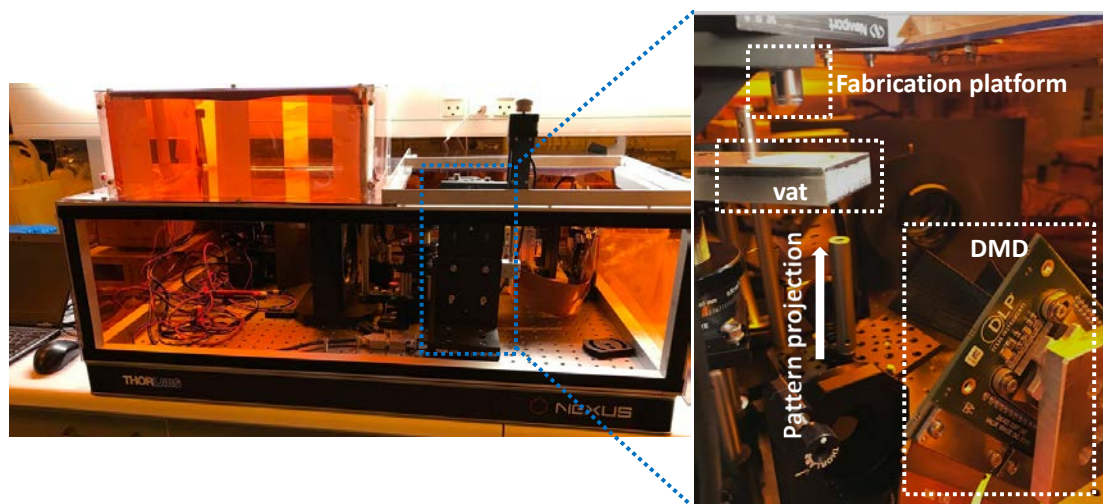


Figure 3.1 A photograph of our home-built polychrome stereolithography printer.

3.1 Optimization of the spatial printing resolution for microchannels

The same resin components were used and the concentrations of PEGDA and LAP were kept the same as before. However, based on the UV-Vis spectra of LAP and QY as shown in **Figure 2.2**, the absorbance of LAP at 365 nm is about 20 times the value of that at 405 nm while the absorbance of QY at 365 nm is only about one-fifth of the value at 405 nm . Several other dyes with higher absorption at 365 nm , such as methyl orange and

diaminobenzophenone, were initially considered to replace QY. However, their poor water solubility prevents their practical use. Adjustments to the resin formulation was made according to Beer-Lambert law, $A = \epsilon lc$, where A is absorbance, ϵ is molar extinction coefficient of a solute, l is the length of light path and c is the concentration of the solution. As an approximation, QY concentration was increased from 1.2 to 6 mg/mL, and exposure time was decreased from 60 to 3 s. The step height/slicing thickness was kept 25 μm as used before. This formulation was then used for preliminary test and hydrogel constructs with microchannels of various sizes were printed to evaluate the spatial printing resolution as before. The results showed that the home-built printer produced less well-defined microchannels using the aforementioned resin formulation (**Figure 3.2**). Even for the largest microchannel tested (square cross-section 400 $\mu\text{m} \times 400 \mu\text{m}$), a notable reduction in vertical dimension was observed when using the home-built printer.

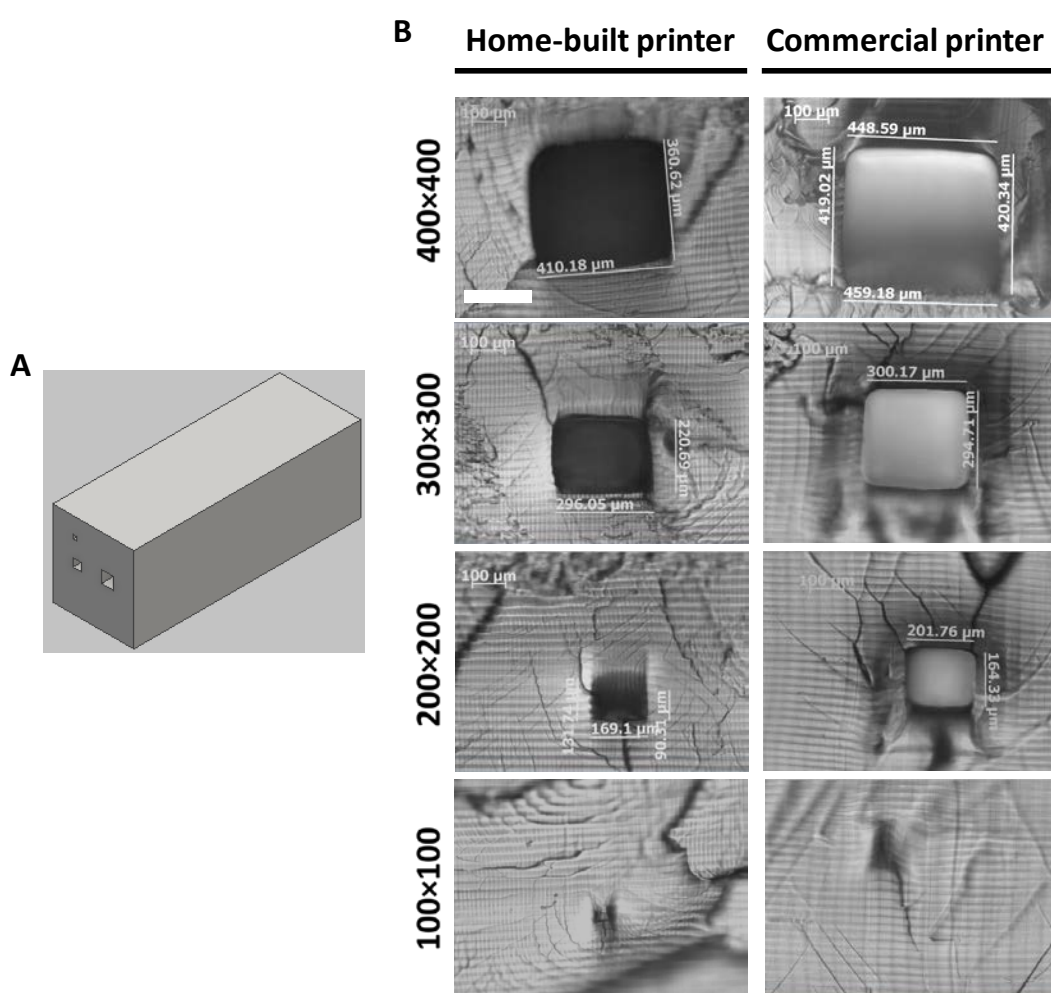


Figure 3.2 A) A representative 3D design of a block with microchannels of desired dimensions. B) Optical micrographs of cross-sections of a series of printed square channels using both the home-built and commercial printer. The resin used for the commercial printer was composed of 200 mg/mL PEGDA, 5 mg/mL LAP and 1.2 mg/mL QY, and the exposure time for each layer was 60 s. The resin used for the home-built printer was composed of 200 mg/mL PEGDA, 5 mg/mL LAP and 6 mg/mL QY, and the exposure time for each layer was 3 s. Scale bar represents 200 μm .

The reduced vertical dimension was suspected to stem from overcuring and therefore the effect of both exposure time and QY concentration on the spatial printing resolution was investigated. First, microchannels printed with the same QY concentration yet different exposure times were characterized. It should be noted that since light exposure is controlled by custom programming code, multiple patterns in the same layer can be sequentially projected. As a result, various structures can be simultaneously printed using the same resin components yet different exposure times. Such flexibility allows for a more efficient optimization approach. In addition, due to the stronger absorption of LAP at 365 nm, photoinitiation is much faster, resulting in reduced fabrication time and subsequent enhanced optimization efficiency. As shown in **Figure 3.3A**, exposure times of 2.5 and 3.0 s resulted in more notable decrease in printed vertical dimensions, while exposure times between 1.7 and 2.0 s did not show significant difference in printed channel dimensions. Exposure times below 1.7 s were also explored, however, mechanically stable structures cannot be printed, as shown in **Figure 3.3B**.

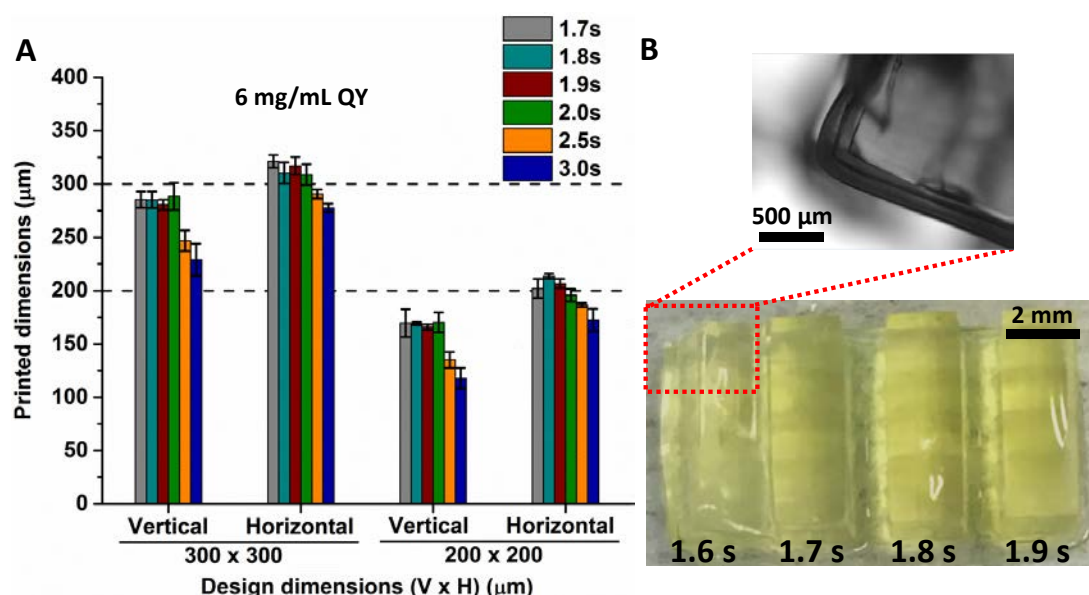


Figure 3.3 A) Measured printed channel dimensions versus design dimensions (error bars show the standard deviation, $n = 3$) from optical micrographs of cross-sections of a series of square channels printed using the same resin components yet different exposure times for each layer. The resin was composed of 200 mg/mL PEGDA, 5 mg/mL LAP and 6 mg/mL QY. B) A photography (top view) of four hydrogel blocks with microchannels printed using the same resin components yet different exposure times. In case of exposure time of 1.6 s, layers started to detach from each other, indicating a weaker bonding between neighboring layers and thus mechanical unstable structures.

Although decreasing exposure time helped to print better defined microchannels, overall QY concentration of 6 mg/mL is not sufficient for high spatial printing resolution. Therefore, QY concentration was increased to 9 mg/mL and microchannels were printed and characterized as before. Different exposure times were also explored, however, it was found that exposure times below 2.5 s could not produce mechanical stable structures when using 9 mg/mL QY. Exposure times between 2.5 and 3.0 s did not show significant difference

(**Figure 3.4A**). Hence, exposure time of 3.0 s was selected in order to keep a balance between mechanical stability and fabrication speed. As shown in **Figure 3.4B**, increased QY concentration largely improved the spatial printing resolution. Moreover, microchannels of square cross-section as small as $100\ \mu\text{m} \times 100\ \mu\text{m}$ were clearly visible using optical microscopy, while in case of 6 mg/mL QY they were completely occluded (**Figure 3.4C**).

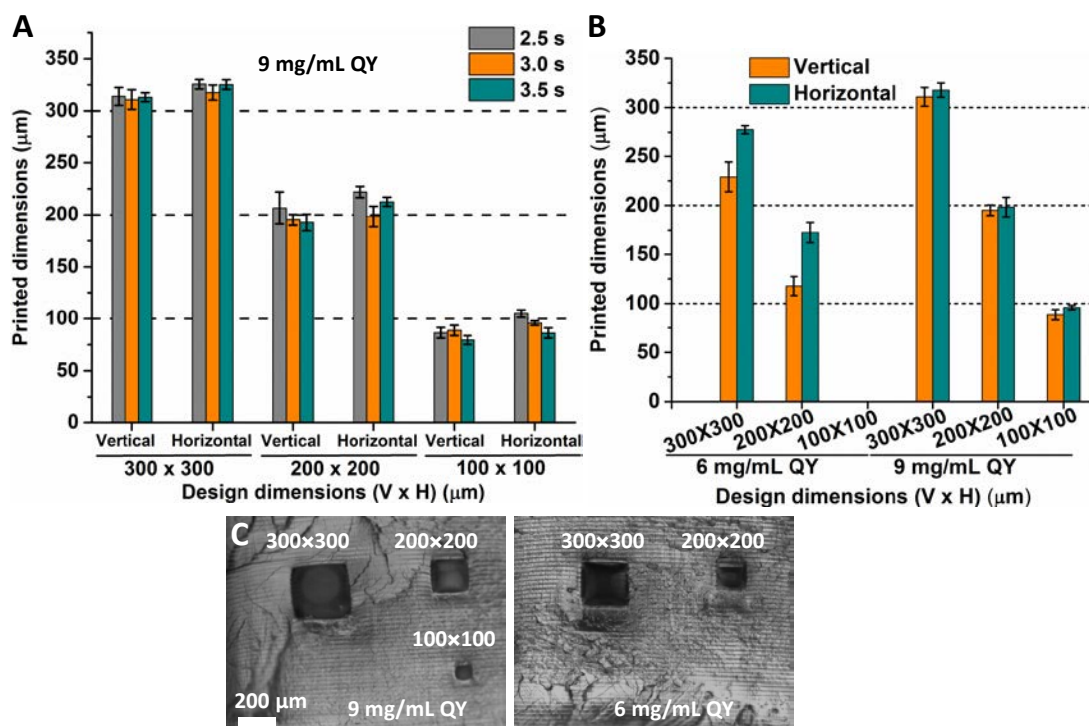


Figure 3.4 A) Measured printed channel dimensions versus design dimensions (error bars show the standard deviation, $n = 3$) from optical micrographs of cross-sections of a series of printed square channels. The resin was composed of 200 mg/mL PEGDA, 5 mg/mL LAP and 9 mg/mL QY. B) Measured printed channel dimensions versus design dimensions (error bars show the standard deviation, $n = 3$) from optical micrographs of cross-sections of a series of printed square channels using different QY concentrations yet the same exposure time for each layer (3 s). C) Optical micrographs of cross-sections of a series of printed square channels using different QY concentrations yet the same exposure time for each layer (3 s).

Despite well-defined features of the printed $100\ \mu\text{m} \times 100\ \mu\text{m}$ channels using 9 mg/mL absorber, as observed by optical microscopy, the resulting channels could not be perfused. A higher absorber concentration (12 mg/mL) was employed to minimize the risk of random channel occlusion as well as to further push the spatial printing resolution, but this resulted in mechanically unstable structures, similar to what was observed in **Figure 3.3B**. The step height/slicing thickness was then decreased from $25\ \mu\text{m}$ to $20\ \mu\text{m}$ to enhance the bonding between neighboring layers and consequently robust structures were successfully printed using 12 mg/mL absorber. With the adjusted resin formulation and printing procedure, microfluidic channels with cross-sections of $100\ \mu\text{m} \times 100\ \mu\text{m}$ can be faithfully printed (**Figure 3.5A,B**) and are fully functional, as demonstrated by successful perfusion of a single

channel stepwise narrowing from a cross-section of $400\ \mu\text{m} \times 400\ \mu\text{m}$ to $100\ \mu\text{m} \times 100\ \mu\text{m}$ after printing (**Figure 3.5C**).

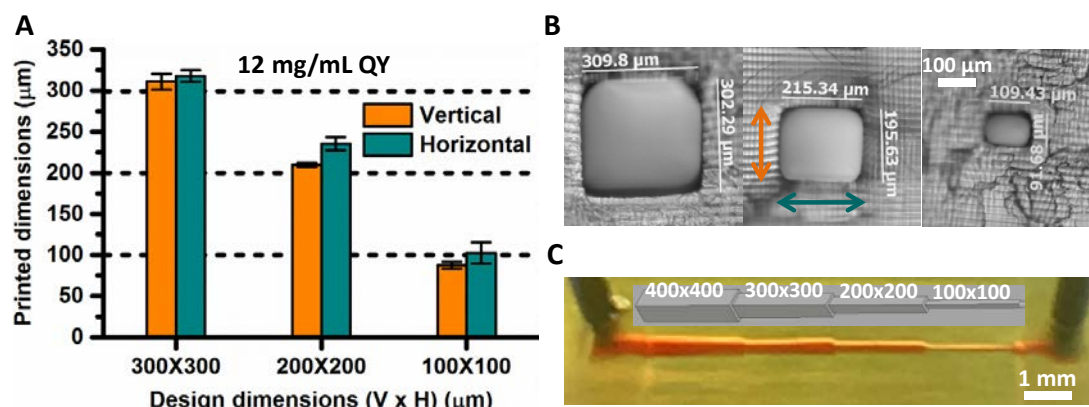


Figure 3.5 A) Measured printed channel dimensions versus design dimensions (error bars show the standard deviation, $n = 3$) from optical micrographs of cross-sections of a series of printed square channels using the resin formulation consisting of 200 mg/mL PEGDA, 5 mg/mL LAP and 12 mg/mL QY. Exposure time of 3 s for each layer and a step height of $20\ \mu\text{m}$ are adopted along with the resin formulation. B) Optical micrographs of cross-sections of a series of printed square channels using the optimized resin formulation. C) Stepwise narrowing channel with square cross-section from $400\ \mu\text{m} \times 400\ \mu\text{m}$ to $100\ \mu\text{m} \times 100\ \mu\text{m}$ printed using optimized resin formulation and perfused with red dyed fluid. The insert shows the design of the narrowing channel.

Later, we also evaluated printing of circular geometries of decreasing diameters and the resulting channel cross-sections are well defined, although the intrinsic grid geometry of the light exposure unit (a Digital Mirror Device) causes jagged perimeters of the smallest diameter designs (**Figure 3.6**). To our best knowledge, few reports have shown the printing of perfusable micro-channels approaching the dimensions of larger arterioles and venules¹⁷⁵ within hydrogel materials.

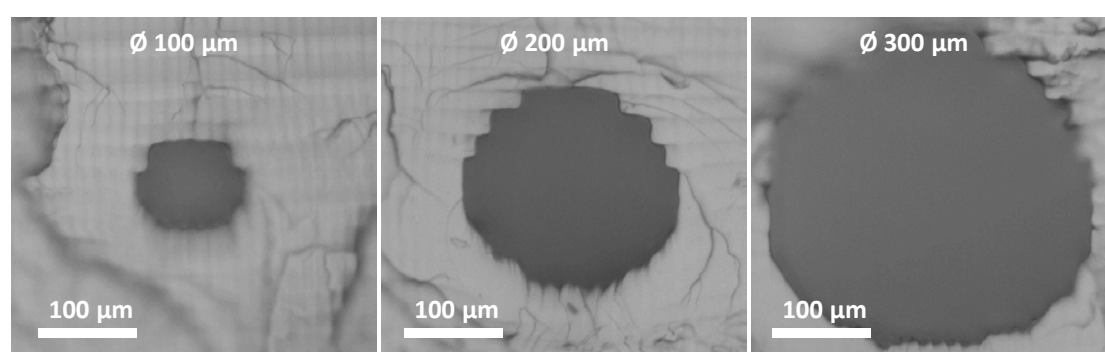


Figure 3.6 A) Optical micrographs of cross-sectioned 3D printed channels of circular design with diameters of $\varnothing 100$, 200 and $300\ \mu\text{m}$. Resin consisted of 200 mg/mL PEGDA, 5 mg/mL LAP and 12 mg/mL QY. Exposure time of 3 s for each layer and a step height of $20\ \mu\text{m}$ are adopted along with the resin formulation.

The effect of LAP concentration on printing was also investigated, and as shown in **Figure 3.7**, LAP concentration less than 5 mg/mL resulted in mechanically unstable structures. In theory, mechanically stable structures could be printed with doubled exposure time (thus

doubled light dose) when using 2.5 mg/mL LAP, however, that would also double the fabrication time. Although the value of 5 mg/mL was used based on our group's previous work on patterning PEGDA hydrogels through single light exposure rather than 3D printing, it turns out to be translated to 3D printing process well.

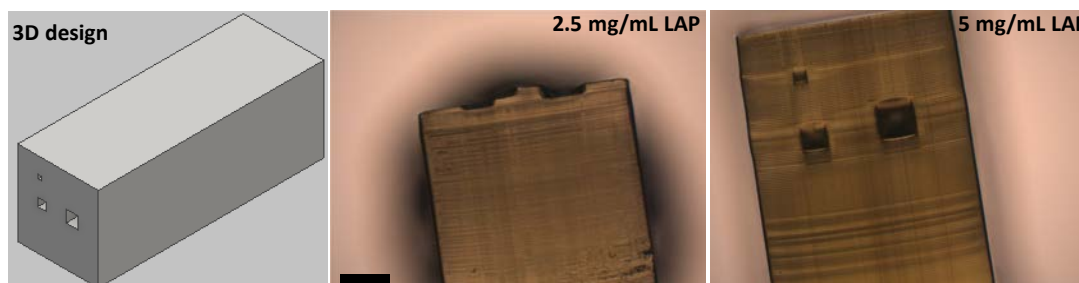


Figure 3.7 The 3D design of a hydrogel block containing microchannels and optical micrographs of 3D printed hydrogel blocks with microchannels using different LAP concentrations. The rest of the resin consisted of 200 mg/mL PEGDA and 12 mg/mL QY. Exposure time of 3 s for each layer and a step height of 20 μm are adopted along with the resin formulation. When using 2.5 mg/mL, channel structures failed to be printed out while the whole block structure was not printed out when using a even lower LAP concentration (1 mg/mL). Scale bar represents 500 μm .

Therefore, the resin composed of 200 mg/mL PEGDA, 5 mg/mL LAP and 12 mg/mL QY along with exposure time of 3 s for each layer and step height of 20 μm , was adopted for the remaining work as optimal printing configuration unless specified otherwise.

Those results collectively suggest that experimental parameters regarding resin optimization are often not completely independent of each other. Increasing absorber concentration generally results in better spatial printing resolution, however, exposure time as well as step height needs to be adjusted accordingly in order to produce mechanically stable structures. Therefore, the combined effect of different experimental parameters is essential for the resin optimization process. Also, well defined features indicated by optical microscopy do not necessarily lead to functional microchannels in terms of perfusion due to random channel occlusion caused by curing of unreacted resin trapped in small cavities, therefore perfusion test should always be performed to confirm that printed microchannel can actually be perfused.

3.2 Swelling and mechanical properties of 3D printed PEGDA hydrogels

As mentioned in the previous chapter, an aqueous resin is essential because it minimizes dimensional changes caused by post-printing swelling in aqueous medium. In a hydrogel, it is the chemical potential that drives water in between chains and the elastic retractive forces of the network that push the water out.¹⁷⁶ The equilibrium is called the equilibrium degree of swelling and is defined either as the mass equilibrium degree of swelling (q) or the volumetric equilibrium degree of swelling (Q).¹⁷⁶

$$q = \frac{M_s}{M_d}, Q = \frac{V_s}{V_d} = 1 + \frac{\rho_p}{\rho_s} (q - 1)$$

with M_s and M_d being the mass of the swollen and the dry gel, V_s and V_d being the volume of the swollen and dry gel, and ρ_p and ρ_s being the density of the polymer and the solvent, respectively. q is easy to measure by weighing both the swollen and dry samples. Since the dimensional change due to post-printing swelling is more of interest, the printed sample is also weighed immediately after printing and then transferred to a water bath where its weight is continuously measured until it remains constant. As shown in **Figure 3.8**, the printed hydrogels reach their equilibrium slightly swollen state within 4 h after being transferred to a water bath, and only a 10% increase in volume was observed when reaching swollen state, which indicates only a 2% increase in each dimension. Therefore, structures can just be printed as designed without extra consideration for compensating dimensional changes due to post-printing swelling. Additionally, all the dimensional measurements presented so far were performed after the printed structures were immersed in water for at least overnight.

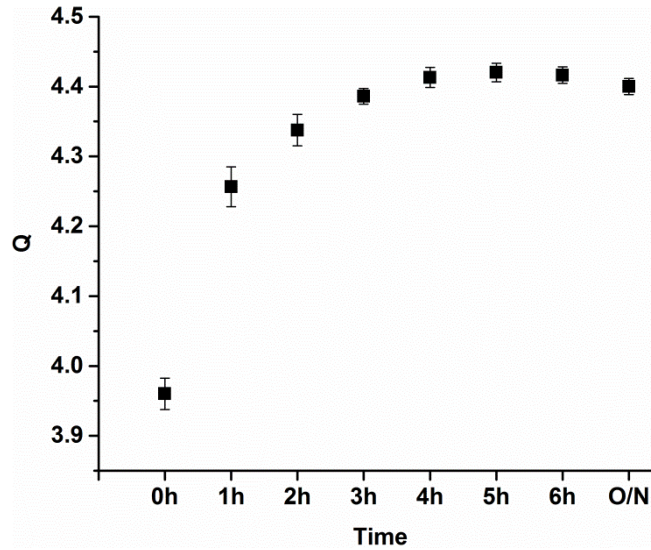


Figure 3.8 Time-dependent volumetric swelling ratio of 3D printed solid PEGDA objects (10 mm × 10 mm × 3.5 mm) immediately after printing (0 h) and after selected times of immersion in DI water (O/N = overnight). Error bars show the standard deviation, $n = 3$.

It should be noted that it is not trivial to obtain the dry weight of samples. Initially samples were dried at 140 °C to speed the process. However, it was found that the weight kept decreasing even after 2 days (**Figure 3.9A**). It was suspected that PEGDA underwent thermal/oxidative degradation at such high temperature.^{177–179} Therefore, several other approaches were adopted in order to make sure samples are completely dried but without degradation: 1) dry at a lower temperature, namely 60 °C; 2) dry at 50 °C in a vacuum chamber; 3) exchange water in samples with methanol and then dry at 50 °C in a vacuum

chamber. As shown in **Figure 3.9B**, all those three approaches gave similar results and the weight obtained was used as dry weight of samples.

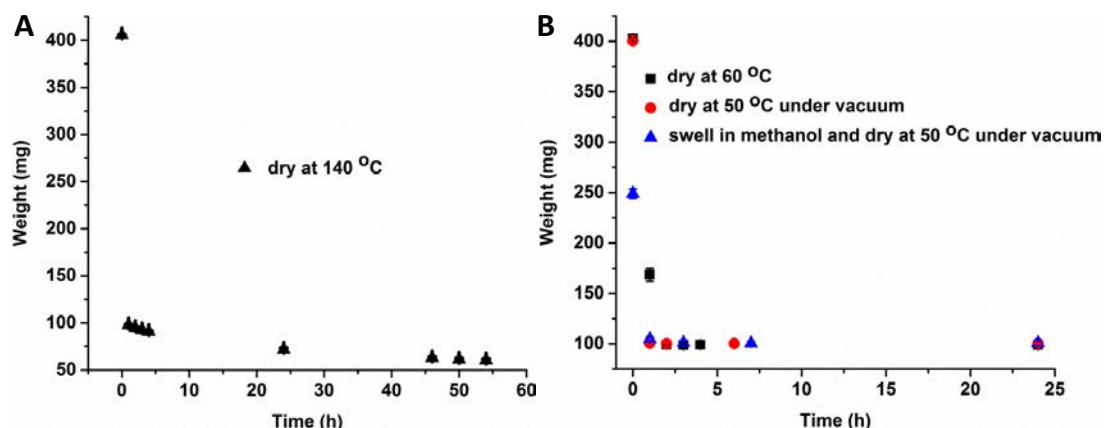


Figure 3.9 A) Time-dependent weight change of 3D printed solid PEGDA objects (10 mm × 10 mm × 3.5 mm) when drying at 140 °C. Time of 0 h denotes the swollen weight in water. Error bars show the standard deviation, n = 3. B) Time-dependent weight change of 3D printed solid PEGDA objects (10 mm × 10 mm × 3.5 mm) when drying at 60 °C, at 50 °C under vacuum or first swelling in methanol and then drying at 50 °C under vacuum. Time of 0 h denotes the swollen weight either in water or methanol. Printed hydrogels swell less in methanol than water. Error bars show the standard deviation, n = 3.

Since mechanical properties are important for long-term use of printed constructs, the shear modulus of printed PEGDA hydrogels were characterized. Shear modulus is defined as the ratio of shear stress to the shear strain, and it is one of several quantities for measuring the stiffness of materials. As shown in **Figure 3.10**, our printed PEGDA hydrogels have a shear modulus of about 0.4 MPa, which enables printed constructs to withstand the needle insertion during perfusion. In comparison, a 15% gelatin hydrogel has a shear modulus of only about 5 kPa,¹⁸⁰ suggesting that it might not be a good candidate material for hydrogel constructs used for long-term flow perfusion.

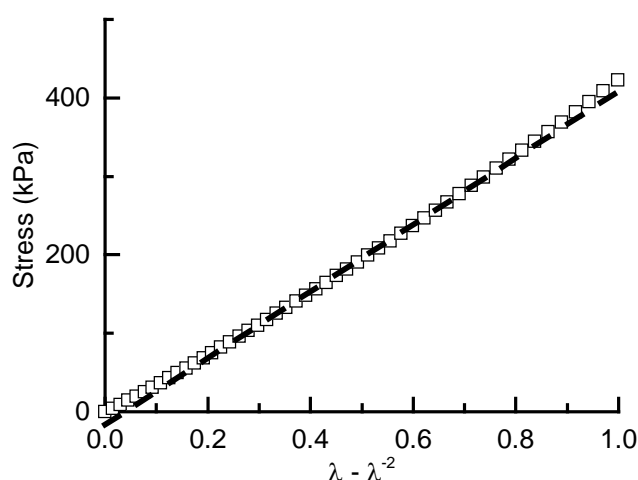


Figure 3.10 Uniaxial compression of a 3D printed solid PEGDA cylinder (Ø6 mm; height 5 mm). The measured stress is displayed versus $\lambda - \lambda^{-2}$, where λ is the extension ratio. Linear fitting using ordinate values from 0.2 to 0.8 (dashed line) yields a shear modulus of 0.43 MPa.

3.3 Perfusion of printed PEGDA microchannel networks

In the previous chapter, a perfusion setup based on a micromanipulator device was introduced. However, the setup was cumbersome and even slight misalignment could cause irreversible damages to the hydrogel constructs. Therefore, a more facile perfusion setup was developed and adopted for the remaining work (**Figure 3.11**).

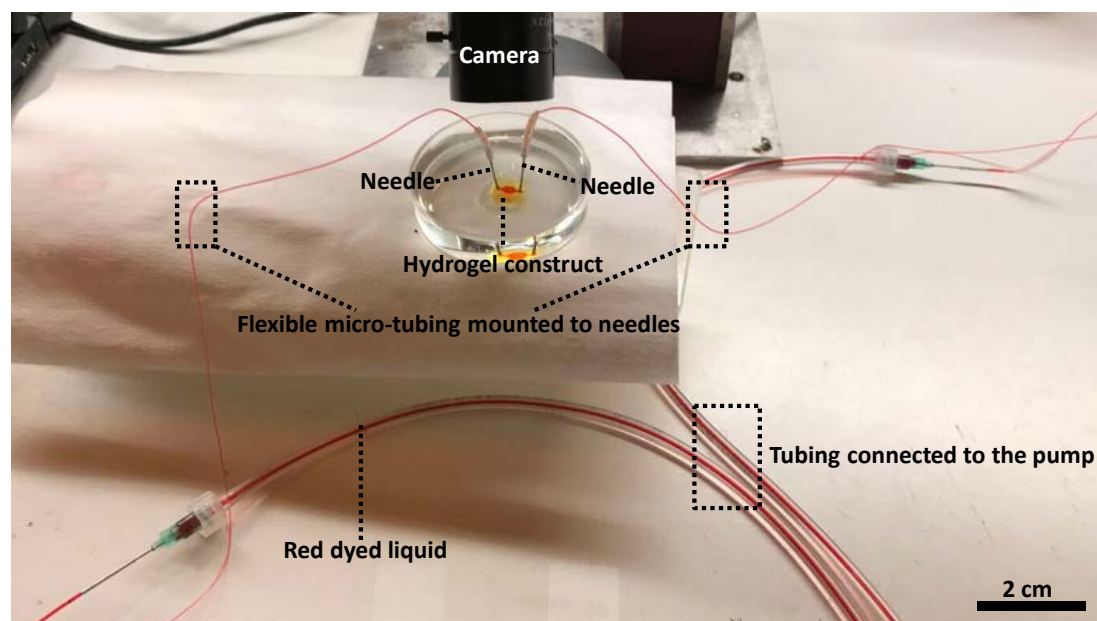


Figure 3.11 A photography of a facile perfusion setup based on flexible micro-tubing. Needles are manually inserted to channel connectors.

The needle insertion can easily be handled manually, which offers much flexibility during insertion and thus make it much easier to form tight seals. However, the use of a micromanipulator device in the first place was to fixate needles onto the stage so no/limited stress would be placed on hydrogel constructs when connecting the needles to the pump. When needles are manually inserted, hydrogel constructs must maintain the stability of needles as well as withstand any stress generated during and/or after connecting the needles to the pump through tubing. In order to minimize any potential stress placed on the hydrogel constructs, flexible micro-tubing was used between the needles and the tubing connected to the pump. Also, mechanical stability of our printed hydrogel constructs also contributes to the successful application of this modified perfusion setup. With such facile and flexible setup, simultaneous independent perfusion of the separate channels of a dual channel scaffold is steadily achieved, while leakage was often observed using the micromanipulator based perfusion setup (**Figure 3.12**).

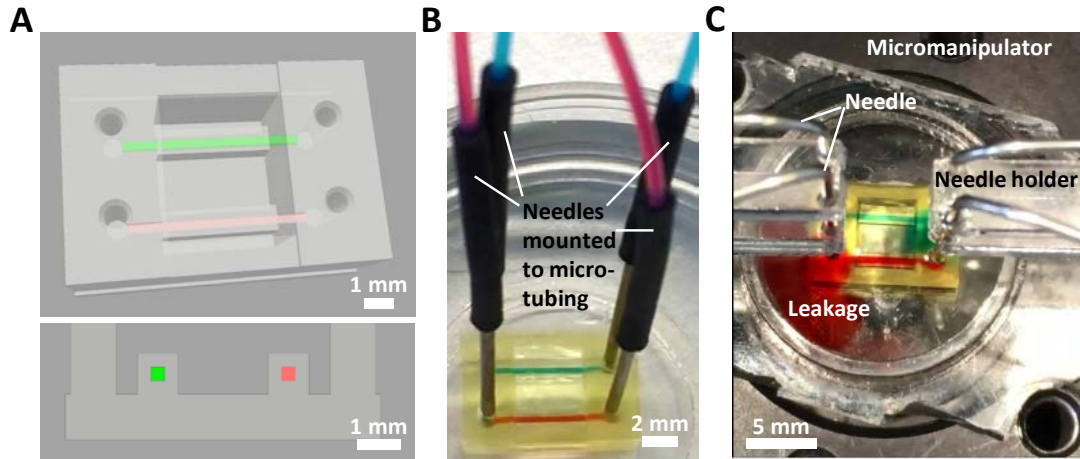


Figure 3.12 A) Design of a dual-channel model in perspective and in cross-section with square channels of side length 300 μm. B) Printed PEGDA dual-channel construct perfused with separate dyed liquids simultaneously using flexible micro-tubing. C) Printed PEGDA dual-channel construct perfused with separate dyed liquids simultaneously using a micromanipulator device. Leakage of dyed liquids was observed at either inlet or outlet.

Furthermore, stable leak-free perfusion for at least one week is routinely observed, documented by time-lapse video of steady-state diffusion concentration gradients of a perfused dye solution across the channel walls (**Figure 3.13A,B**). As an approximation of one dimensional diffusion situation, time-dependent diffusion distance of dye molecules was measure by analyzing snapshots of a recorded perfusion video at different time points, and the results (**Figure 3.13C**) fit the one-dimensional Einstein-Smoluchowski relation ($d^2 = 2Dt$) well, indicating well-defined diffusion characteristics can be realized within our printed PEGDA hydrogels using such facile perfusion setup.

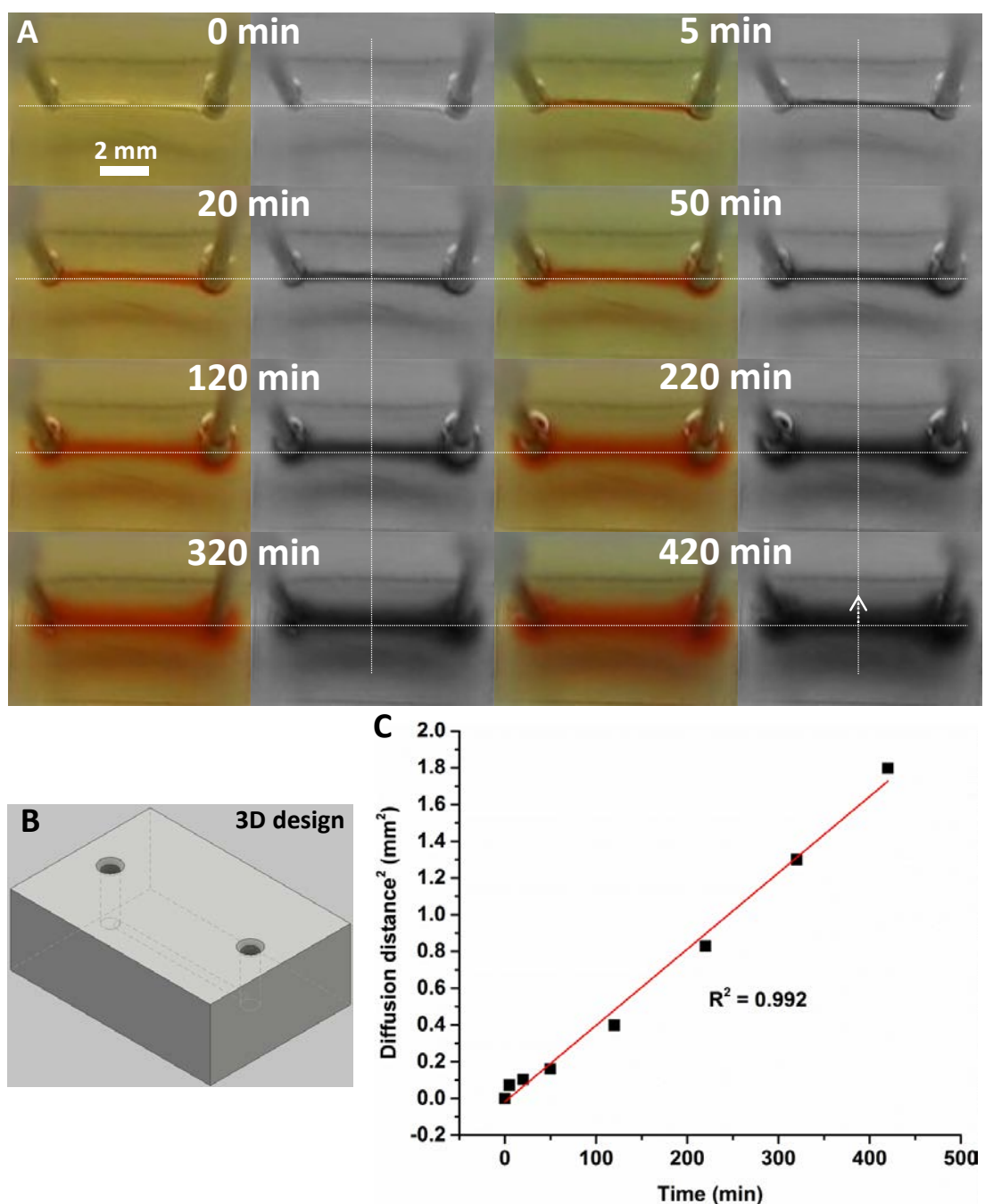


Figure 3.13 A) Snapshots of a 7 day-perfusion video at different time points during the first 7 h and their converted grey scale images. The intersection point of the horizontal and vertical dash line was defined as the starting point (zero distance) and the diffusion distance was measured along the vertical dash line starting from the intersection, as indicated by the white arrow in the grey scale image at 420 min. B) 3D design of the hydrogel construct used in this study, which contains a single straight circular channel (\varnothing 300 μ m). C) The squares of measured one dimensional diffusion distance plotted against diffusion time.

Later, as what was discussed in the previous chapter, we printed a series of channel systems with increasing 3D complexity, which were afterwards successfully perfused (**Figure 3.14**). These results show that perfusable channels with full 3D design freedom are easily accessible by our approach, while being a significant challenge using current PDMS-based

microfluidic manufacturing processes or extrusion printing. Furthermore, with the home-built printer, a 3D spiral microchannel of square cross-section as small as $200\text{ }\mu\text{m} \times 200\text{ }\mu\text{m}$ can be faithfully printed as well as perfused, while the commercial printer could only print perfusable 3D spiral microchannel of square cross-section no smaller than $400\text{ }\mu\text{m} \times 400\text{ }\mu\text{m}$.

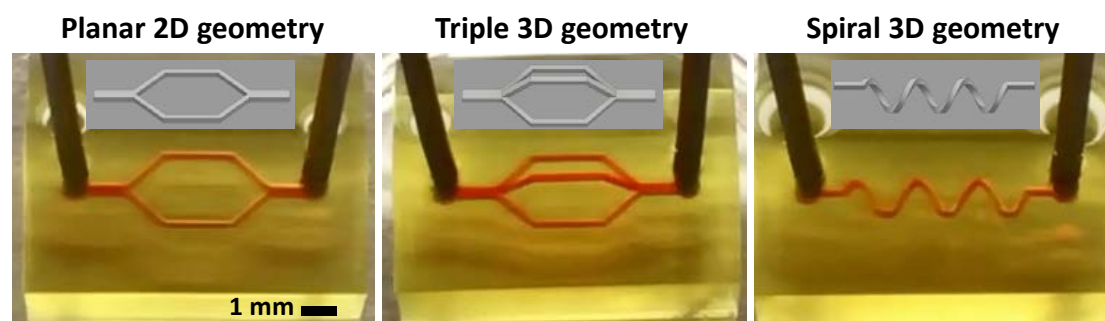


Figure 3.14 Optical micrographs of 3D printed and perfused PEGDA channel networks ($200\text{ }\mu\text{m}$ (V) \times $250\text{ }\mu\text{m}$ (H) rectangular channel cross-section for the channel in the vertical plane in triple 3D geometry and $200\text{ }\mu\text{m} \times 200\text{ }\mu\text{m}$ square channel cross-section for the rest of channels) of increasing 3D complexity from dual planar configuration, triple 3D geometry to spiral geometry. The inserts show the respective CAD designs.

Also, it should be noted that similar to what was discussed in the previous chapter, the dimension of the channel in vertical plane in case of triple 3D geometry needs to be enlarged a bit to compensate for the higher fluidic resistance due to printing process. However, as shown in **Figure 3.15**, all the channels in the triple 3D geometry printed by our home-built printer can be simultaneously perfused with identical square cross-section of $300\text{ }\mu\text{m} \times 300\text{ }\mu\text{m}$. When channel dimensions are further decreased to $200\text{ }\mu\text{m} \times 200\text{ }\mu\text{m}$, the channel in the vertical plane needs to be enlarged a bit in order to achieve perfusion of all the channels. Those results collectively suggest that the spatial resolution of the home-built printer is much better than the commercial one since such compensation is only necessary for microchannels with cross-sections smaller than $300\text{ }\mu\text{m} \times 300\text{ }\mu\text{m}$ while in case of the commercial printer the compensation is required even for microchannels with cross-section of $400\text{ }\mu\text{m} \times 400\text{ }\mu\text{m}$. It stands to reason that the degree of overcuring, which depends on resin formulation and light exposure, should be similar regardless of the design dimensions of microchannels and therefore its effect is more significant in case of microchannels with small dimensions. Therefore, proper adjustments need to be made when necessary in order to compensate for the deviation of the printed channel dimensions from the design dimensions due to the resolution limit.

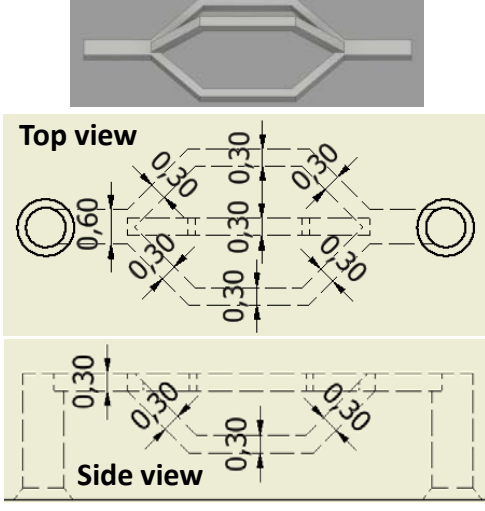
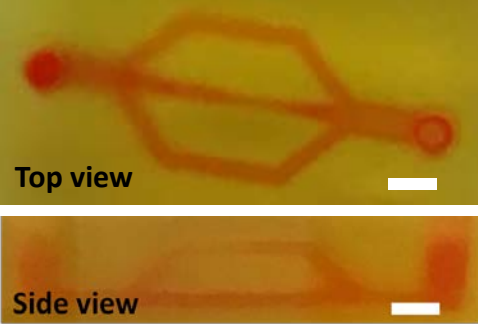
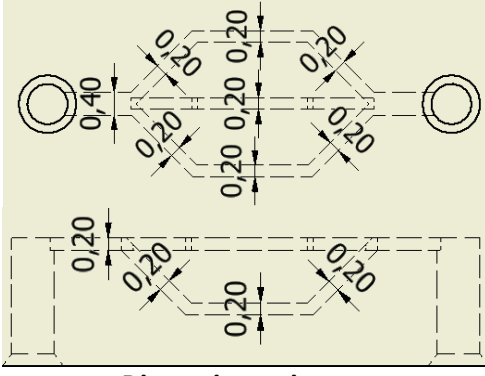

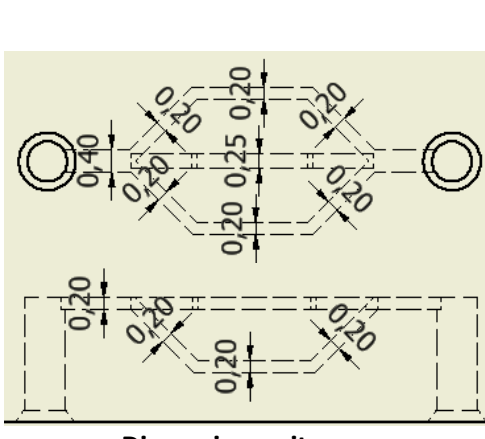
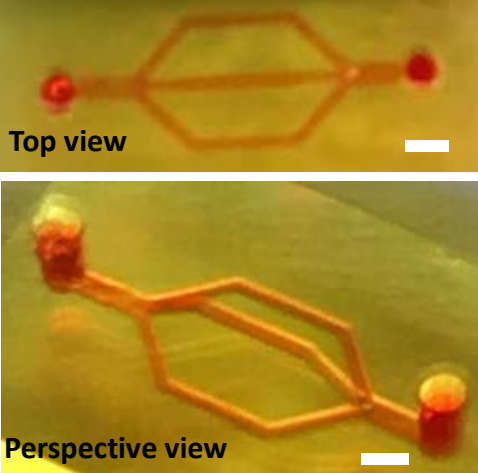
Design	Perfusion images
 <p>Top view</p> <p>Side view</p> <p>Dimension unit: mm</p>	 <p>Top view</p> <p>Side view</p> <p>Scale bar represents 500 μm.</p>
 <p>Top view</p> <p>Side view</p> <p>Dimension unit: mm</p>	 <p>Top view</p> <p>Scale bar represents 400 μm.</p>
 <p>Top view</p> <p>Side view</p> <p>Dimension unit: mm</p>	 <p>Top view</p> <p>Perspective view</p> <p>Scale bar represents 400 μm.</p>

Figure 3.15. 3D design of a triple geometry channel system and the orthographic views (top and side) of a 3D design of a triple geometry microchannel system and the photographs of actually printed hydrogel construct with microchannels perfused with red dye liquid. When microchannels have a cross-section smaller than $300\ \mu\text{m} \times 300\ \mu\text{m}$, the channel in the vertical plane needs to be enlarged in order to compensate for the higher fluidic resistance stemming from the reduced channel dimensions

during printing process and subsequently to ensure simultaneous perfusion of all the channels. Therefore proper adjustments need to be made due to the resolution limit.

3.4 Cell compatibility of the printed micro-perfusable chip constructs

Similar to what was discussed in the previous chapter, we first investigated the cell compatibility of SLA printed bowl-shaped constructs (**Figure 3.16**). Bowl structures were used because their overall planar bottom surface greatly facilitated the visualization of cells by microscopy compared to sealed microchannels. Human umbilical vein endothelial cells (HUVEC) instead of endothelial cell line CRL-2922 were used for better biological relevance. As discussed before, the surfaces of printed constructs need to be functionalized with cell adhesive ligands prior to cell seeding. However, gelatin methacrylate (GelMA) is used instead of RGD peptides because GelMA can be used in a large quantity at a much lower cost than RGD peptides. GelMA is widely used as a photocrosslinkable hydrogel matrix for accommodating live cells.¹⁸¹ In order to avoid the formation of bulk GelMA hydrogels during functionalization, a low GelMA concentration (10 mg mL^{-1}) is adopted.¹⁸² PEGDA structures with pendant unreacted acrylate groups were exposed to LAP-containing GelMA solution and subsequently to UV-A illumination. Seeded HUVECs adhered and assembled into a nearly confluent layer with negligible observable cell death after culture for 24 h (**Figure 3.16**), demonstrating the cell compatibility of the printed and modified constructs.

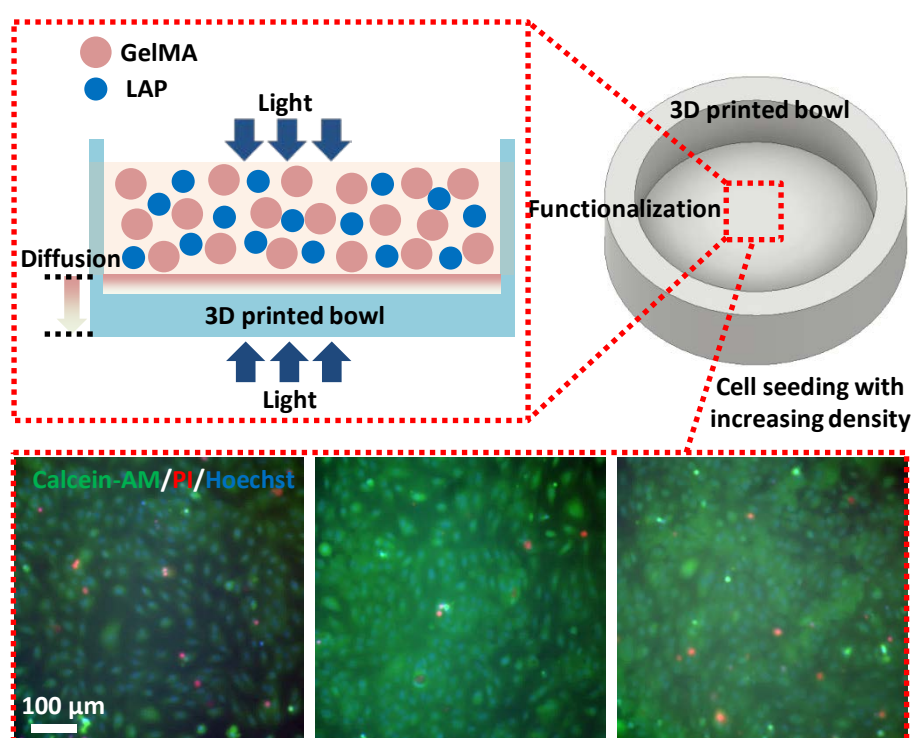


Figure 3.16 A schematic diagram of bio-functionalization of printed bowl structures using cell adhesive protein, gelatin methacrylate (GelMA), and composite fluorescence images of human umbilical vein endothelial cells (HUVECs) 24 h after being seeded on functionalized PEGDA bowl structures: live cells (calcein-AM, green), dead cells (propidium iodide, red) and nuclei (Hoechst 33342, blue). The seeding densities were 7×10^4 , 1.4×10^5 and $2.1 \times 10^5 \text{ cells cm}^{-2}$ (from left to right).

Next, we printed and exposed a circular channel (\varnothing 300 μm) with its inner wall functionalized with GelMA to a HUVEC cell suspension by perfusion. The use of a low GelMA concentration (10 mg mL^{-1}) resulted in specific channel wall functionalization without unwanted bulk GelMA hydrogel formation in the fluidic channels. After incubation for 24 h HUVEC cells lined the vessel-like wall (**Figure 3.17**). This demonstrates the applicability of our light-based synthetic hydrogel printing and biofunctionalization approach to produce *in vitro* endothelialized fluidic channel systems with physiological complexity.

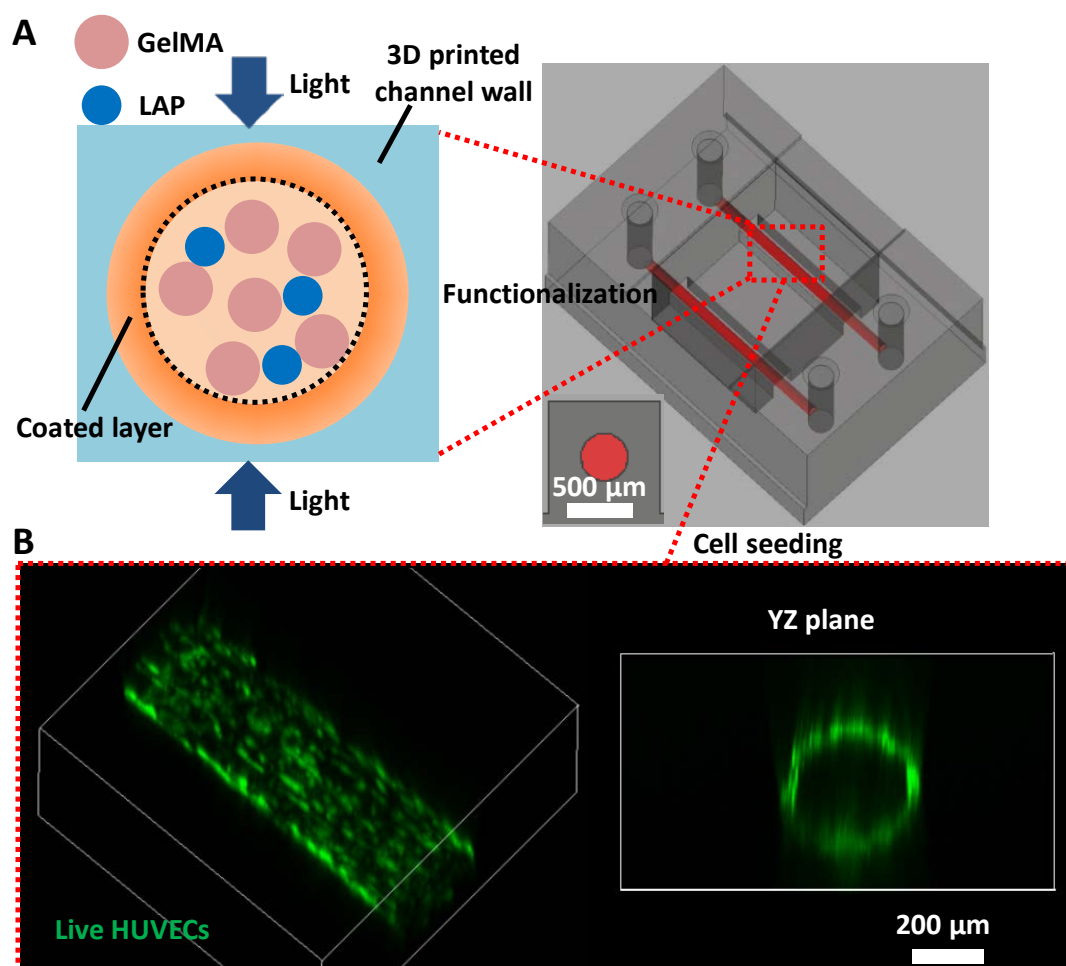


Figure 3.17 A) A schematic diagram of bio-functionalization of printed microchannel walls using cell adhesive protein, gelatin methacrylate (GelMA), and a design of a dual-channel model with cylindrical \varnothing 300 μm channels, with the insert showing the channel cross-section in red. B) Confocal laser scanning micrographs of live HUVEC cells lining the printed and functionalized PEGDA micro-channel walls.

It should be noted that microchannels seeded with endothelial cells were initially sectioned using a blade prior to visualization because the pixelated nature of printed structures stemming from digital mirror device strongly scatters the light and subsequently prevents 3D imaging through an intact microchannel structure, as shown in **Figure 3.18A**. However, due to the microscale size of printed microchannels, sectioning samples proved to be very challenging. Therefore, the printing configuration was adjusted by Prof. Niels B.

Larsen and samples that minimize the light scattering were printed and used for visualization, as shown in **Figure 3.18B**.

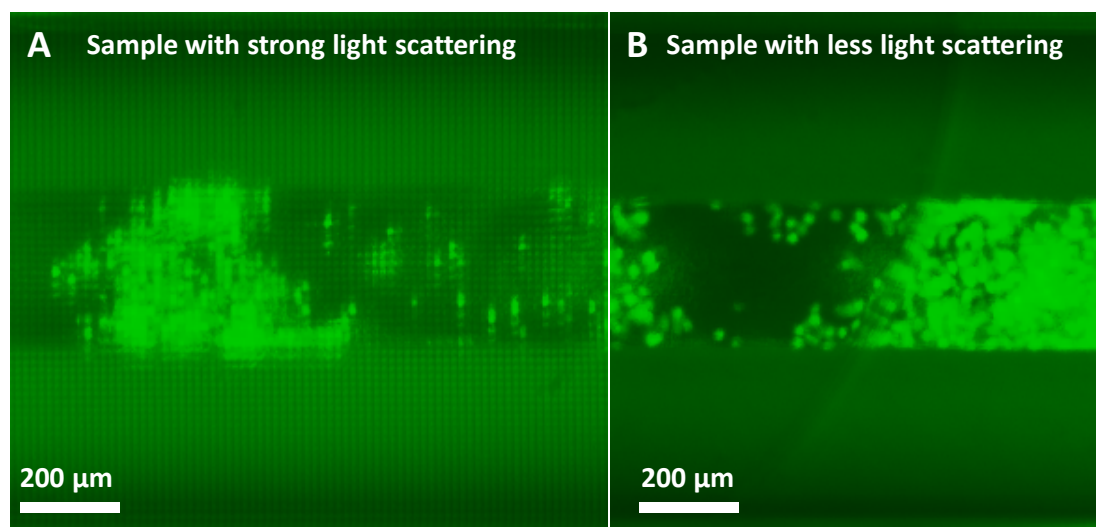


Figure 3.18 A,B) Fluorescence microscopic images of seeded endothelial cells in non-sectioned microchannels in case of strong (A) and less light scattering (B), respectively. Cells were stained with calcein-AM (green) and printed PEGDA hydrogel constructs also give green autofluorescence.

3.5 Embedding of cell-laden matrices in printed perfusable hydrogel chips

As a next step, we fabricated a true 3D chip unit with separate cell culture chamber and vascular-like fluidic networks, as illustrated in **Figure 3.19**, to address the current fabrication limitations for creating advanced *in vitro* models. The central culture chamber is surrounded by a multi-furcated perfusion network composed of 8 circular channels ($\sim \varnothing 200 \mu\text{m}$) and traversed by a center channel ($\varnothing 180 \mu\text{m}$, **Figure 3.19A,B**) only supported by a narrow bridge with diamond shaped fenestrations (**Figure 3.19A**, insert). This design enables tissue cells to reside on all sides of the center channel. All the channels that are not in horizontal plane are designed to be slightly larger based on what was discussed in the previous section. The center channel is designed to be even smaller to compensate for the reduced fluidic resistance due to its overall shorter length. All those adjustments are based on the fluidic resistance formula as listed in the previous chapter and to ensure a more or less equivalent fluidic resistance among all the channels so they can be simultaneously perfused. First, the independent perfusion of the channel network and the culture chamber using aqueous dye solutions demonstrates the ability to introduce different materials into distinct chip construct volumes (**Figure 3.19C**). The observed slight blur along the chamber and channel perimeters is caused by fast diffusion of the small dye molecules into the surrounding diffusion-open PEGDA hydrogel in the time between loading the channels and recording the micrograph. Then, we separately perfused the channel network with LAP-containing acrylated rhodamine solution and the chamber with GelMA solution containing LAP and live-stained 3T3 fibroblasts. Subsequent UV-A illumination of the printed device induced covalent binding of the rhodamine molecules diffused into the walls of the channel network

and cross-linking of the cell-laden hydrogel in the culture chamber. Confocal imaging confirmed the coexistence of perfused fluidic channels and encapsulated live cells (**Figure 3.19D-F**).

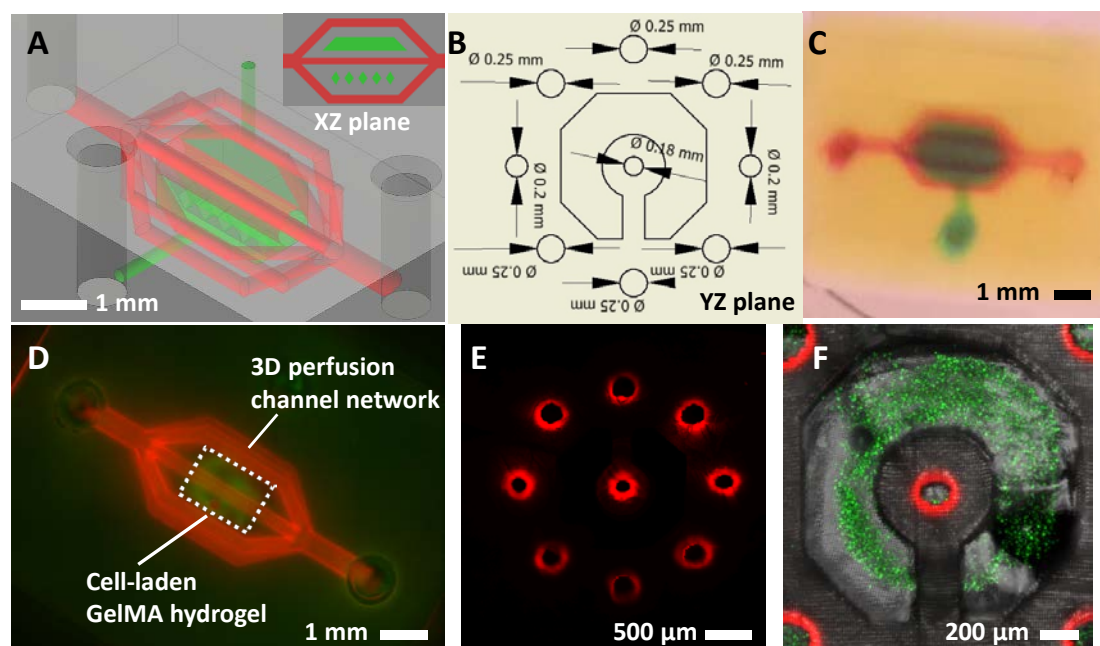


Figure 3.19 A,B) Design of a culture chamber with 8 surrounding and one central traversing vascular channels (A) and its corresponding cross-sectional view in the YZ plane (B) showing all the design channel dimensions. The insert in (A) shows the cross-sectional view in the XZ plane. C) Photograph (top view) of the printed PEGDA construct with the vascular network perfused by red dyed liquid and the chamber perfused by blue dyed liquid. D) Fluorescence micrograph (top view) of the construct with the vascular network walls coated by rhodamine (red) and the chamber filled with GelMA hydrogel laden with live fibroblasts (calcein AM, green). E) Confocal fluorescence micrograph (rhodamine, red) of a cross-sectioned slice of the construct showing perfusion of microfluidic channels. f) Confocal fluorescence micrograph of a cross-sectioned slice of the construct showing the perfused vascular network (rhodamine, red), live 3T3 fibroblasts (green) and the PEGDA construct outline (transmitted light, gray).

Those results demonstrate the flexibility of our approach for embedding a highly compliant cell-laden matrix in a mechanically stable yet diffusion-open hydrogel microfluidic chip of intermediate compliance. However, two common problems were often observed during the embedding procedure. Firstly, although channel dimensions were adjusted to compensate for the fluidic resistance difference, all the channels cannot always be simultaneously perfused (**Figure 3.20A**). Secondly, the culture chamber was often not fully filled with cell-laden matrices (**Figure 3.20B**). Although all the tubing was always pre-filled with perfusion medium before needle insertion, air bubbles could still occur during perfusion partly due to the fact that GelMA can function as a surfactant, thus effectively creating void space in the culture chamber. Moreover, the structural supports of the center channel in the chamber could obstruct the flow and complicate the fluidic dynamics, thus preventing effective filling of the culture chamber.

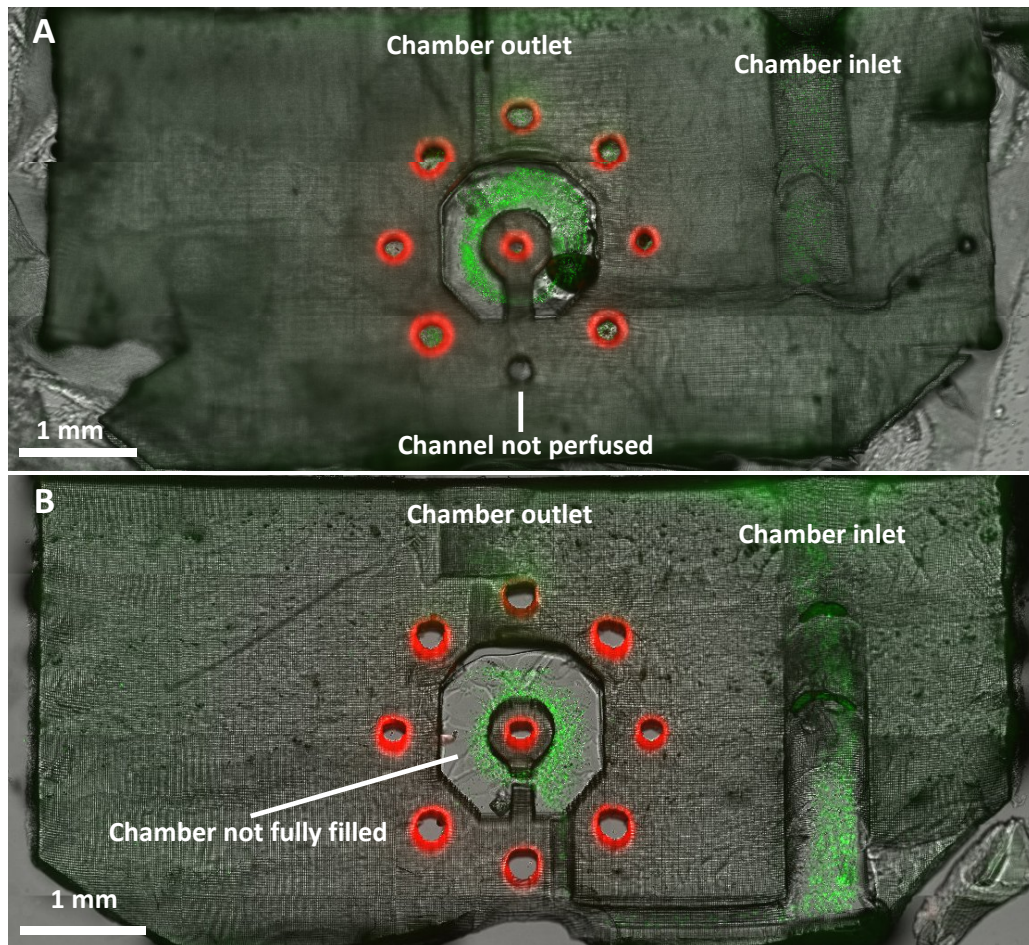


Figure 3.20 A,B) Fluorescence micrographs of cross-sectioned slices of the constructs showing the perfused vascular network (rhodamine, red), live 3T3 fibroblasts (green) and the PEGDA construct outline (transmitted light, gray). In (A) one channel was perfused while in (B) much void space was observed in the culture chamber. The green color of the background was due to the autofluorescence of printed PEGDA hydrogels.

In order to address those two common problems, a new perfusion chip design is implemented (**Figure 3.21**). The main concept is similar, but with a few adjustments. Firstly, a loading chamber is incorporated right above the culture chamber so that embedding of cell-laden matrices can be accomplished by simple pipetting, and the perfusion channel connected to the chamber is intended to remove all remaining liquid medium by suction before loading rather than to fill the chamber (**Figure 3.21A,B**). It should be noted that cells seeded in the loading chamber will consume the oxygen diffused from the top and therefore cells in the culture chamber can only survive on the oxygen diffused from the channel network. Secondly, the sloped parts of all branched channels are enlarged so the effect of overcuring on printed channel dimensions can be minimized as previously discussed, which results in more or less equivalent fluidic resistance within perfusion network, and therefore the same design dimension is adopted for all the channels (**Figure 3.21C,D**).

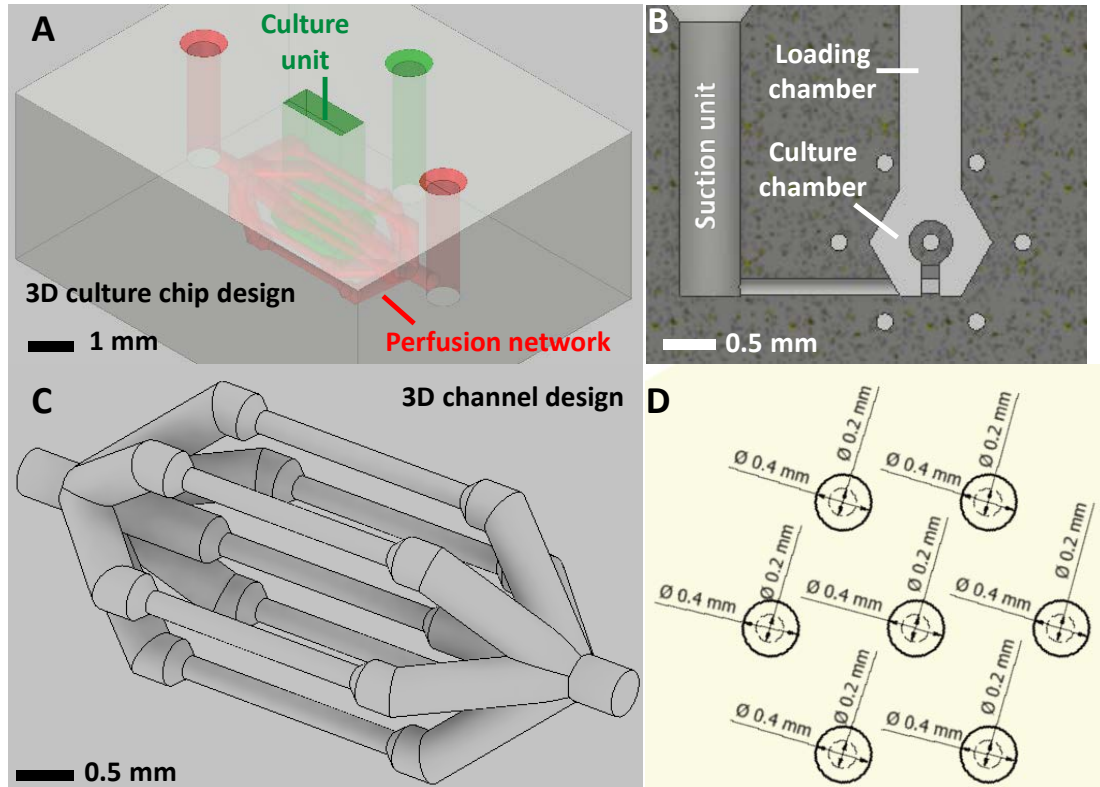


Figure 3.21 A,B) Design of a culture chamber with 6 surrounding and one central traversing vascular channels (A) and its corresponding cross-sectional view (B). C,D) Design of an adjusted multi-furcated channel network with enlarged sloped part (C) and its corresponding cross-sectional view (D) showing all the design channel dimensions.

To test if the culture chamber can be fully filled using the adjusted design, pre-gel GelMA solutions containing LAP and fluorescence microbeads were carefully pipetted into the loading chamber that was previously fully emptied and subsequently exposed to UV-A illumination. Confocal imaging of a sectioned sample confirmed that the chamber was fully filled with gelled GelMA after illumination (**Figure 3.22A**). Perfusion check was also performed to test the adjusted design of channel network and it was shown that simultaneous perfusion of all channels can be achieved rather easily (**Figure 3.22B**).

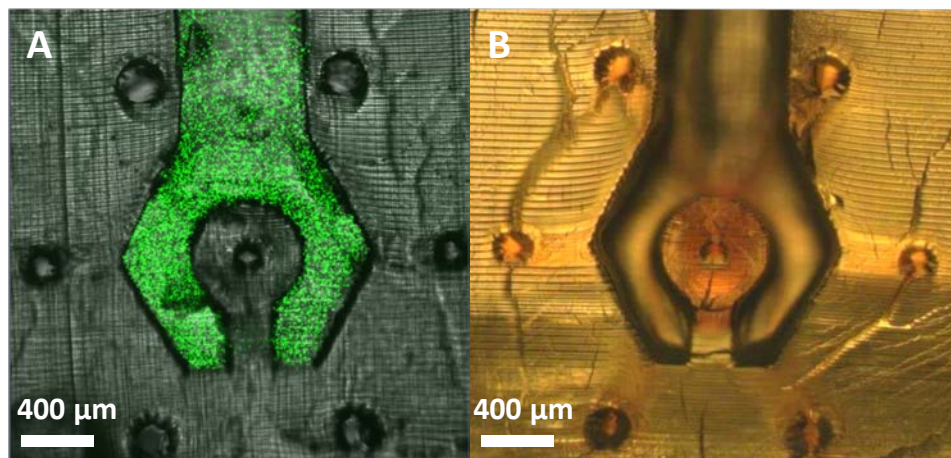


Figure 3.22 A) Confocal fluorescence micrograph of a cross-sectioned slice of the construct showing the culture chamber filled with fluorescence microbeads (green) encapsulated in GelMA and the PEGDA construct outline (transmitted light, gray). B) Micrograph of a cross-sectioned slice of the construct showing the channel network perfused with red dyed liquid.

The long-term steady perfusion has been demonstrated in a single straight circular microchannel, as showed in **Figure 3.13**. The same test was then performed in a culture chip construct with both a multi-furcated channel network and a culture chamber to see if a structure with more intricate structural features can withstand long-term and continuous convective flow. The results showed that the construct can be steadily perfused for at least a week, snapshots of the recorded perfusion video at different time points are shown in **Figure 3.23**. The dye diffuses from the channel volume through the diffusion open PEGDA matrix and establishes a stable color (concentration) gradient near the object's perimeters within the first 12 h. The gradient remains stable over the 7 days captured in the video, *via* daily exchange of the surrounding water bath that would otherwise become saturated with the diffusing dyes.

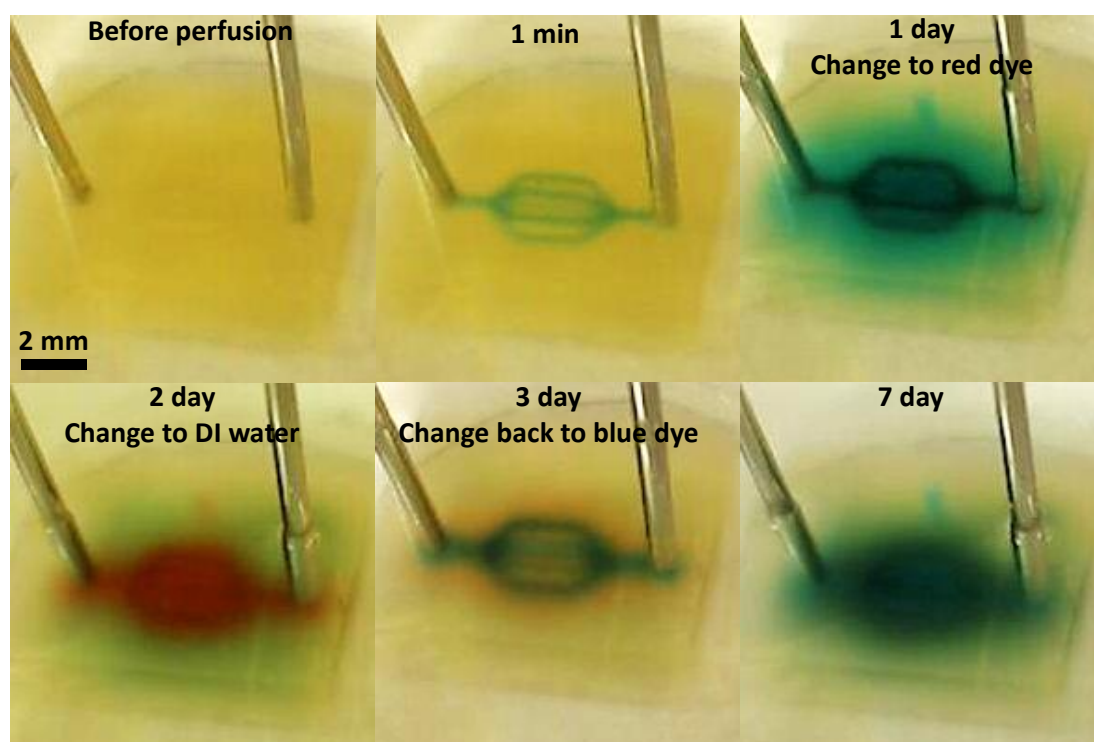


Figure 3.23 Long-term perfusion of a 3D printed PEGDA culture chip containing a multi-furcated channel network (each channel of cross-section \varnothing 200 μ m) as well as a culture chamber immersed in a water-filled petri dish with change between dyed liquids (blue, red and undyed DI water) every day.

After the demonstration of effective chamber filling as well as steady perfusion of channel network, we further developed a perfusion culture platform to see if the incorporated microfluidic network can sustain a healthy true 3D culture in the long term. First, we optimized LAP concentration for cell encapsulation in order to ensure adequate cell

viability after gelation of GelMA via radical photopolymerization. Before, cells were encapsulated and then immediately visualized to demonstrate the filling of the culture chamber. However, radicals formed during gelation can be toxic to cells,¹⁶⁰ and therefore it is important to use a suitable LAP concentration so GelMA can be properly gelled with minimized cytotoxic effect on long-term culture. Cell-laden pre-gel GelMA solution supplemented with different LAP concentrations were added to a standard well plate and subsequently exposed to UV-A irradiation. After a 7-day culture period with intermediate medium change every 2 days, cells were visualized using live/dead staining. As shown in **Figure 3.24A and B**, a high concentration of LAP (5 mg/mL) had significant deleterious effect on cell viability and almost no cells were alive after 7-day culture, while adequate cell viability was observed using a low LAP concentration (0.5 mg/mL), but only limited to a thin layer (100-200 μm thick) right below the surface. Those results confirmed that a suitable LAP concentration is essential during gelation process and that cells embedded deep within hydrogels without proper vascularization cannot survive in the long term due to the diffusion limit of oxygen and other necessary nutrients. Considering the fact that cell-laden GelMA embedded in our printed hydrogel culture chips needs to be sectioned for visualization, a higher concentration of both GelMA and LAP is preferred so formed GelMA hydrogels can withstand the sectioning process better. Thus the same test was performed using a higher concentration of both GelMA (100 mg/mL) and LAP (1 mg/mL), but samples were cultured only for 2 days to mainly investigate the effect of encapsulation process on cell viability. As shown in **Figure 3.24C**, sufficient cell viability was observed after encapsulation probably due to the fact that radicals are consumed faster by GelMA at a higher GelMA concentration. Therefore, such formulation is adopted for cell encapsulation for the remaining work.

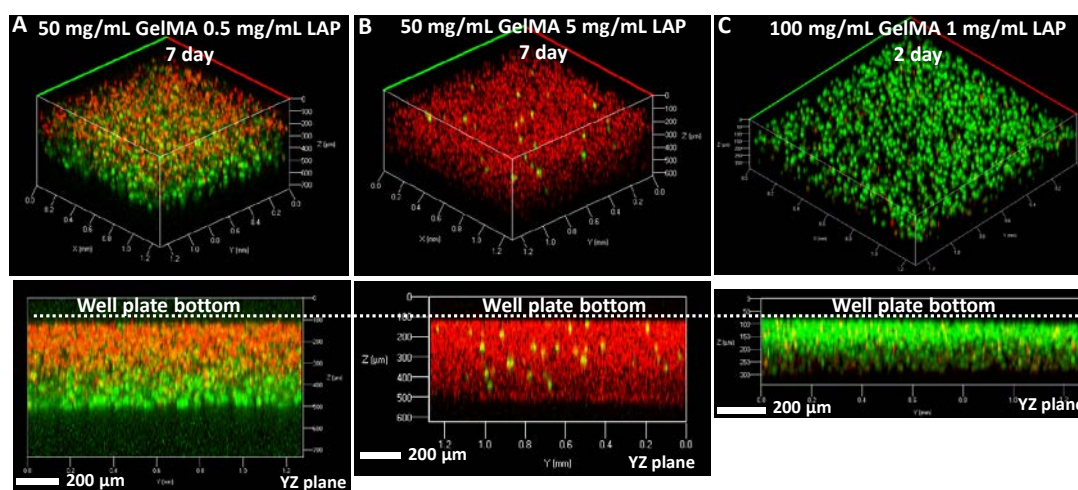


Figure 3.24 A,B) Confocal images of HT-29 cells 7 day after being encapsulated in 50 mg/mL GelMA with either 0.5 mg/mL (A) or 5 mg/mL (B) LAP: live cells (calcein-AM, green) and dead cells (propidium iodide, red). The seeding density was 5×10^6 cells/mL. C) Confocal images of HT-29 cells 2 day after being encapsulated in 100 mg/mL GelMA with 1 mg/mL LAP: live cells (calcein-AM, green) and dead cells (propidium iodide, red). The seeding density was 10×10^6 cells/mL.

The previously discussed perfusion setup in this chapter was applied with minor adjustments to meet the requirement of a sterilized environment for cell culture studies. Since a sterilized environment prefers a closed system, the container for printed hydrogel chip, which is usually a petri dish, needs to be properly capped during perfusion culture to minimize the risk of contamination and therefore CO₂ laser is utilized to create holes on petri dish lids for needle insertion (**Figure 3.25**). The holes are designed to be larger than necessary to allow for flexibility in case of misalignment. In addition, the holes are sealed by Parafilm prior to the insertion process to avoid contamination.

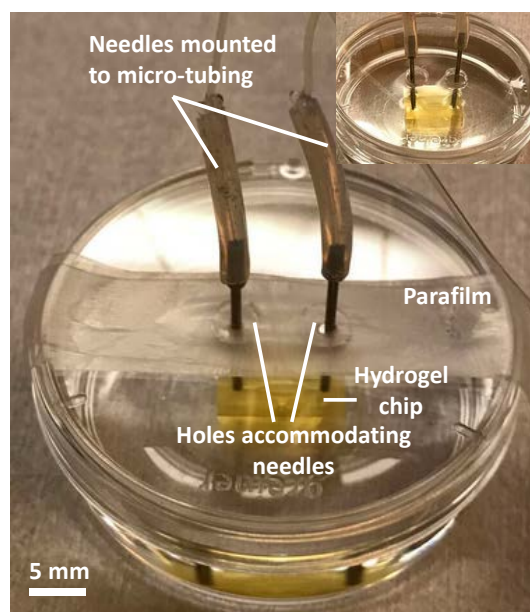


Figure 3.25 Two needles mounted to the micro-tubing were connected to a printed hydrogel chip in a water-filled petri dish with two holes on its lid. The insert shows the same setup without Parafilm covering the holes.

The whole perfusion culture setup is illustrated in **Figure 3.26**. It consists of a medium reservoir, a multi-channel peristaltic pump, a sample incubator, a heated circulating water bath and a gas supply unit. An external supply of 95% air and 5% CO₂ is used to maintain constant pH of culture medium in both the medium bottle and petri dishes containing the printed hydrogel chips. The medium reservoir is composed of two glass bottles with holes drilled in their lids for tubing, one for culture medium and the other filled with sterilized water for humidifying the gas mixture before entering the medium bottle in order to minimize evaporation of medium. A 0.22 μ m filter is connected to the end of the gas tubing to avoid contamination. A water bath is used to keep both the medium and humidifying bottle warm. Samples are kept inside a microscope stage incubator without a lid to avoid constraints on the tubing. Instead, a plastic bag is wrapped around the incubator to minimize heat and gas exchange with surrounding atmosphere. Heated circulating water bath is used to keep the incubator warm. The gas mixture also passes through the heated circulating bath before entering the incubator. The multi-channel peristaltic pump allows for

simultaneous perfusion of multiple samples. Before perfusion culture starts, all the tubing is perfused by a large amount of 70% ethanol, followed by sterilized water using the peristaltic pump. The surfaces of all equipment are wiped with 70% ethanol prior to experiment. Printed samples along with all the glass bottles are sterilized by UV-C irradiation. Sterilized Samples are then transferred to a laminar flow bench for cell loading and subsequently connected to the pump through needle insertion and tubing. Although it is not a perfectly sterilized environment, culture medium used for perfusion is still completely transparent after a 7-day culture period, which indicates no or limited contamination (**Figure 3.26C**).

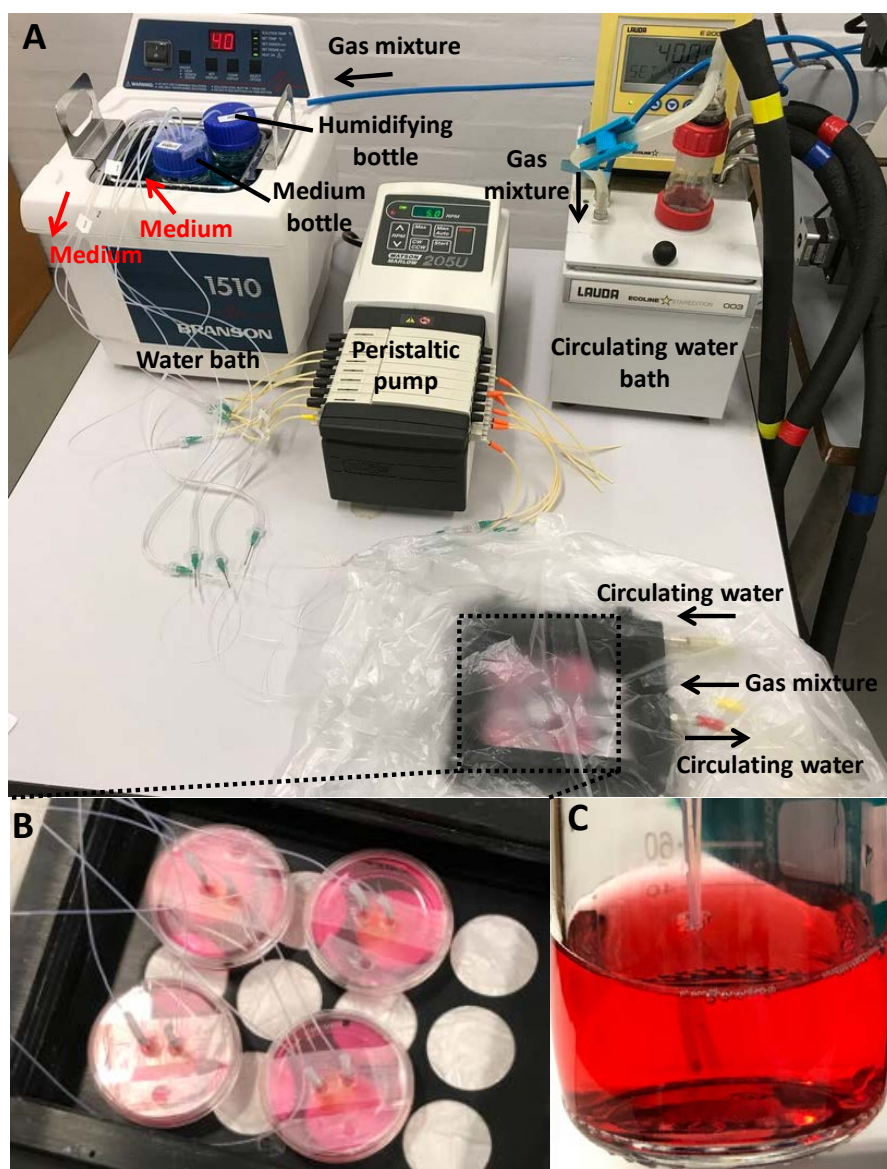


Figure 3.26 A) A photograph of the perfusion culture setup. The system consists of a medium reservoir, a multi-channel peristaltic pump, a sample incubator, a circulating water bath and an external gas supply unit. The medium reservoir is continuously fed with a gas mixture (95% air and 5% CO₂) humidified gas mixture to maintain pH and to minimize evaporation. The medium is circulated through an automated peristaltic pump. Samples are kept inside a stage incubator wrapped with a plastic bag with continuously fed warm circulating water and humidified gas mixture. B) Four samples were placed in the stage incubator and simultaneously perfused. C) A photograph of the culture medium used for perfusion after a 3-day culture period.

To test if perfusion culture can maintain a healthy 3D cell culture, colorectal adenocarcinoma cell line (HT-29) was encapsulated in GelMA solution and subsequently loaded into the printed hydrogel culture chip. After a 3-day and 7-day perfusion culture period, samples were sectioned and afterwards visualized using standard live/dead staining. Samples that were loaded with the same cell-laden GelMA and cultured without medium perfusion through channel network were used as controls (static cultures). Confocal imaging showed a higher fraction of live cells in the perfused samples (**Figure 3.27**), indicating that soluble factors such as oxygen and nutrients can continuously diffuse from channel network to culture chamber and consequently maintain a healthier cell culture. This demonstrates the potential of this facile approach for manufacturing robust hydrogel culture chips as *in vitro* cell culture models that can find many uses such as drug screening and *in vitro* disease modeling.

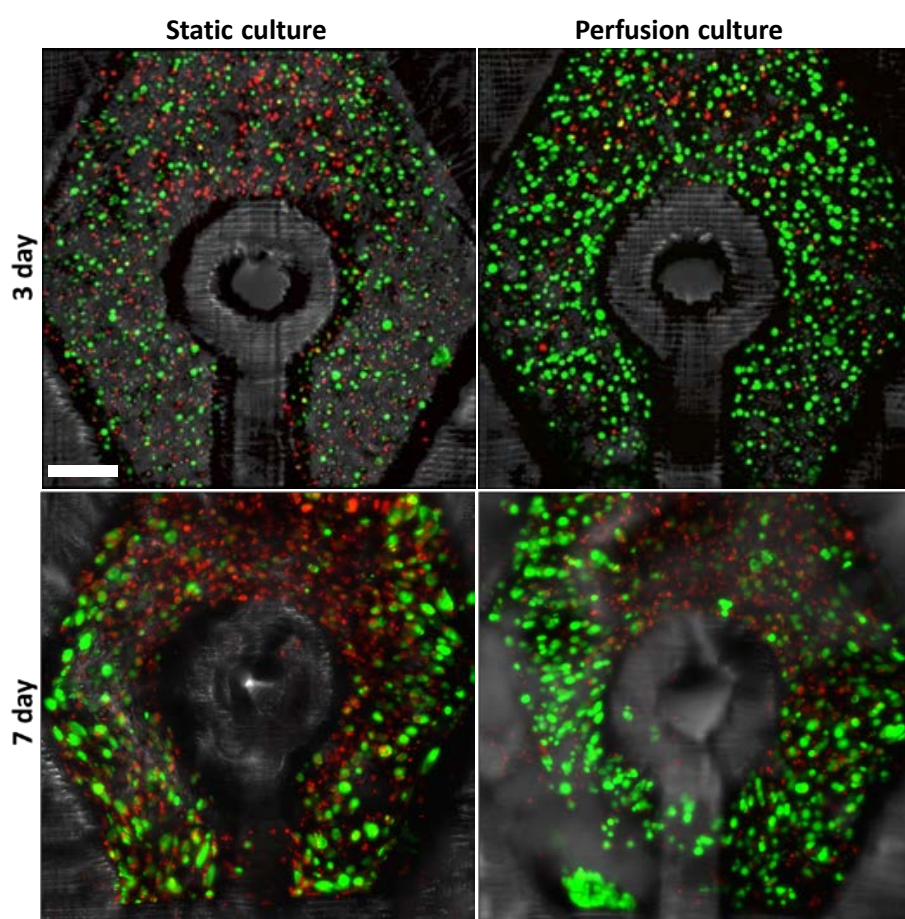


Figure 3.27 Confocal fluorescence micrographs of cross-sectioned slices of the culture chamber in printed hydrogel chips showing the live HT-29 cells (calcein-AM, green), the dead cells (propidium iodide, red), and the PEGDA construct outline (transmitted light, gray) after either a 3-day or 7-day culture period in both static and perfusion culture conditions. Scale bar represents 200 μm .

3.6 Printing and perfusion of a massively perfusable tissue chip

Unpublished data: The authors would like to keep this section confidential until they are published.

3.7 Conclusion

In summary, we have developed a new approach based on high-resolution stereolithography employing easily synthesized and commercially available starting compounds to produce *in vitro* vascular network-like hydrogel constructs with high 3D complexity, facile perfusion setup, and the possibility to culture cells in both the vascular networks and the defined interstitial volumes. In addition, this technique is suitable for production up-scaling without compromising spatial resolution and fabrication speed with the continuous advances in optical components developed for SLA. Further work should be performed to validate the proposed approach with respect to its use as fully functional *in vitro* models. Future studies will focus on detailed investigation of long-term cell culture behavior in 3D when the chemical microenvironment is modulated by compound perfusion through the vascular network-like constructs. This versatile platform opens new avenues for a number of biomedical applications, such as chemotaxis studies, drug development and *in vitro* disease modeling.

3.8 Experimental section

3.8.1 Materials

Poly(ethylene glycol) diacrylate (M_n 700 g mol⁻¹, PEGDA) and Quinoline Yellow (QY) were acquired from Sigma-Aldrich and used as purchased.

3.8.2 LAP synthesis

LAP was synthesized based on a previously reported procedure.¹⁶⁰ Briefly, at room temperature and in a nitrogen atmosphere, 3.2 g of 2,4,6-trimethylbenzoyl chloride (TCI America) was added dropwise to an equimolar amount of continuously stirred dimethyl phenylphosphonite (3.0 g, Sigma-Aldrich). The reaction mixture was stirred overnight, followed by the addition of a four-fold excess of lithium bromide (6.1 g, Sigma-Aldrich) dissolved in 100 mL acetone. The reaction mixture was then heated to 50 °C. After about 10 min, a white solid precipitate formed. The mixture was cooled to room temperature and then filtered under vacuum. The filtrate was washed 3 times with acetone to remove unreacted lithium bromide, and the remaining solvent was removed by vacuum.

3.8.3 GelMA synthesis

GelMA was synthesized based on a previously reported procedure.¹⁸³ Briefly, a 100 mg mL⁻¹ gelatin solution was first prepared by dissolving gelatin powder (Type A, 300 g bloom from porcine skin, Sigma-Aldrich) in Dulbecco's phosphate-buffered saline (DPBS) at 60 °C for 2 h with vigorous stirring. Then the solution temperature was lowered to 50 °C and 0.14 mL of methacrylic anhydride was added dropwise to the gelatin solution for each gram of gelatin in the solution (about 50% degree of methacrylation). The mixture was allowed to

react for 4 h at 50 °C with vigorous stirring. The methacrylation reaction was then quenched by diluting the mixture with DPBS pre-warmed to 40 °C to a GelMA concentration of 45 mg mL⁻¹. GelMA was precipitated overnight by the addition of 100 mL ice-cold acetone to the diluted mixture. Acetone was then decanted from the precipitated GelMA, which was then dissolved in DPBS at 100 mg mL⁻¹ at 40 °C. The warm GelMA solution was filtered under vacuum through a 0.2 µm filter (PES membrane, VWR vacuum filtration), transferred to a 12-14 kDa molecular weight cutoff (MWCO) dialysis tubing (Spectra/Por 4), and dialyzed against deionized (DI) water at 40 °C for 3 days with frequent change of the dialysis media (twice a day) to remove remaining methacrylic acid. Finally, the GelMA was lyophilized for 2 days and subsequently stored at -20 °C prior to further use.

3.8.4 Pre-treatment of cover slip surfaces

The PEGDA hydrogels were printed onto pre-treated cover glasses for the purpose of easy handling, calling for prior chemical activation of the glass surface to secure the printed PEGDA to the glass support. The treatment was based on a previously reported procedure.¹⁷³ The circular cover glasses (Ø 20 mm, VWR) were first cleaned via plasma treatment to remove organic contaminants. The cleaned glasses were then soaked in a 2% v/v 3-(trimethoxysilyl)propyl methacrylate (Sigma-Aldrich) solution in 95% v/v ethanol/water (pH adjusted to 5 by acetic acid) for 10 min, washed with pure ethanol for 3 times, and eventually baked at 105 °C for another 10 min.

3.8.5 Projection stereolithography of PEGDA hydrogels

Stereolithographic printing used a home-built high resolution printer based on 1-to-1 projection of light reflected off a Digital Mirror Device (13.68 µm pixel pitch, DLP7000 UV, Texas Instruments, DMD) coupled to a V-7000 Hi-Speed controller (Vialux). The printing process proceeded using custom written MATLAB (MathWorks) code that synchronizes digital mask exposure on the DMD, light exposure using a 365-nm high power LED (LZ1-00UV00, Ledengin), and fabrication stage movement via a linear stage (LNR50S, Thor Labs). The power density at the vat bottom was 10.9 mW cm⁻² as measured using a UV power meter (OAI 306, Optical Associates). Pre-treated cover glasses were mounted to the fabrication stage. Non-adhesive fluorinated ethylene propylene (FEP) foil (130 µm thick) was applied to the vat bottom to facilitate smooth release of each printed layer from the vat. 3D models were designed using Autodesk Inventor 2016 (Autodesk). The resulting design was sliced into a series of digital masks with a slicing thickness of 20 µm using the open-source slicer software Slic3r. The aqueous resin consisted of 200 mg mL⁻¹ PEGDA, 5 mg mL⁻¹ LAP and 12 mg mL⁻¹ QY. After adding resin to the vat, the fabrication stage was moved close to the vat bottom. The first digital mask was projected for an extended time of 15 s to ensure proper attachment of the polymer to the cover glass. After the formation of the first layer, the stage was raised by 20 µm for each additional digital mask exposure. The first 10 layers

(corresponding to ~200 μm thickness) were each exposed for 15 s followed by a gradual reduction of the exposure time to 3 s over the next 10 layers to minimize mechanical strain. All layers in the remaining part of the printed object, including all parts defining channel and chamber structures, were exposed for 3 s each (5 s for massively perfusable tissue construct). After printing, the object was immediately immersed in DI water for at least overnight to leach out remaining reagents and allowing it to reach its equilibrium swollen state prior to further use. Prior to dimensional measurements, printed samples were removed from cover slip using a blade. An array of micropillars as structural supports can be included at the bottom to facilitate smooth removal of samples from cover slip without damaging channel structures.

3.8.6 Analysis of swelling properties of printed PEGDA hydrogels

Solid PEGDA objects of size 10 mm \times 10 mm \times 3.5 mm were printed on a cover glass by stereolithography employing the optimized pre-polymer solution composition and printing conditions. Immediately after printing, surplus water was removed by quickly touching the cuboid's surfaces with tissue, and its weight was determined. The sample was immediately re-immersed in DI water, and the procedure was repeated after 1, 2, 3, 4 h as well as after overnight immersion. The swollen cuboid was placed in an oven at 60 $^{\circ}\text{C}$ and the weight after overnight drying was used for calculating the volumetric swelling ratio.

3.8.7 Analysis of mechanical properties of printed PEGDA hydrogels

Solid PEGDA cylinders of \varnothing 6 mm and height 5 mm were printed on a cover glass by stereolithography employing the same pre-polymer solution composition and printing conditions used for printing perfusion constructs. The printed cylinders were released from the cover glass support by a scalpel and allowed to reach their equilibrium degree of swelling by immersion overnight in DI water. The mechanical properties of the still wet samples were analyzed on an Instron 5967 at a compression rate of 0.5 mm min^{-1} to a final extension ratio λ of 0.7. The data was analyzed using neo-Hookean rubber elastic theory for highly swollen hydrogels that predicts a linear dependence of the stress on $\lambda^{-\lambda^{-2}}$.¹⁸⁴ A linear fit to the data in the $\lambda^{-\lambda^{-2}}$ range from 0.2 to 0.8 yields a hydrogel shear modulus of 0.43 MPa.

3.8.8 Perfusion of printed PEGDA microchannel networks

Blunt stainless needles (\varnothing 0.8 mm \times 22 mm, Sterican) were mounted to polytetrafluoroethylene (PTFE) tubing ($\varnothing_{\text{inner}}$ 0.30 mm and $\varnothing_{\text{outer}}$ 0.50 mm, Adtech Polymer Engineering) that was connected to a peristaltic pump (MasterFlex) via Luer Lock connectors. Printed constructs were fixated onto the bottom of a polystyrene petri dish using double sided adhesive tapes, and the petri dish filled with DI water. Aqueous solutions of either red or blue food dye (Dr. Oetker) were used as perfusion fluids. The tubing was pre-perfused

with fluid to avoid bubbles, and the needles were inserted into the 3D printed inlet and outlet (\varnothing 0.7 mm). Pumping proceeded at a flow rate of $100 \mu\text{L min}^{-1}$ and the channel perfusion was recorded by either a phone camera (for short-term perfusion) or a stationary live camera (for long-term perfusion). In case of phone camera, the recorded videos were stabilized using the plugin TurboReg in the Fiji software package.^{185,186} In case of stationary live camera, a Python code was used to control the camera so that one image was taken every one minute. After recording, images were stacked to a time-lapse video using Fiji software. To measure diffusion distance of the dye molecules, images taken at different time points were converted to grey scale images using Fiji software.

3.8.9 Cell culture

Primary human umbilical vein endothelial cells (HUVECs) (Gibco) were cultured in Medium 200 (Gibco) supplemented with 2% v/v Large Vessel Endothelial Supplement (Gibco). Human colorectal adenocarcinoma cells (HT-29) (ATCC, HTB-38, Rockville, MD, USA), and 3T3 Swiss Albino cells (ECACC 85022108) were cultured in Dulbecco's modified Eagle's medium with high glucose (DMEM, Biowest) supplemented with 10% v/v fetal bovine serum (FBS, Sigma-Aldrich) and 1% v/v penicillin-streptomycin (P/S, Sigma-Aldrich). Cells were incubated at 37°C in a humidified atmosphere with 5% CO_2 . All the cell cultures were passaged following the respective vendors' manuals. HUVECs were not used beyond passage 5.

3.8.10 Cytotoxicity assay

Bowl structures ($\varnothing_{\text{inner}}$ 8 mm, $\varnothing_{\text{outer}}$ 10 mm, 0.4 mm thick bottom, 2.5 mm overall height) were printed and immersed in DI water for 24 h with two intermediate changes of water bath to allow the leaching of unreacted reagents. $100 \mu\text{L}$ aqueous solution of 10 mg mL^{-1} GelMA and 5 mg mL^{-1} LAP was added to each bowl, followed by 2 min of UV-A illumination (330-380 nm, peaking at 365 nm, 18 mW cm^{-2}).¹⁷⁴ The reaction mixture was removed and the structures were washed with DI water 3 times before being immobilized in a 6-well plate using double sided adhesive tape. HUVEC culture medium was added to the well plate to submerge each structure and the whole plate containing the structures was sterilized by 20 min exposure of UV-C irradiation (254 nm, UV sterilization cabinet, Cleaver Scientific) in a laminar flow bench. The structures were immersed in HUVEC culture medium overnight to exchange the water in the hydrogel for culture medium. Before cell seeding, culture medium was partially removed so that each bowl structure was not submerged yet still moist. Then the culture medium inside each bowl was replaced with $100 \mu\text{L}$ HUVEC suspension. Cells were seeded at three densities, $7 \times 10^4 \text{ cells cm}^{-2}$, $1.4 \times 10^5 \text{ cells cm}^{-2}$, and $2.1 \times 10^5 \text{ cells cm}^{-2}$, respectively, and cultured at 37°C in 5% CO_2 for 24 h. Non-adherent cells were washed away using culture medium, and adhered cells were stained with calcein-AM ($2 \mu\text{g mL}^{-1}$, Invitrogen), propidium iodide (PI, $2 \mu\text{g mL}^{-1}$, Sigma-Aldrich) and Hoechst 33342 ($2 \mu\text{g mL}^{-1}$,

Sigma-Aldrich) for 1 h. Each sample was then characterized by fluorescence microscopy (AxioVert 100 M, Zeiss). Composite microscopy images were generated using Fiji by combining the three fluorescence channels.

3.8.11 Endothelialization of perfusion microchannels

The inner walls of printed vascular channels were functionalized by perfusing 0.5 mL aqueous solution of 10 mg mL⁻¹ GelMA and 10 mg mL⁻¹ LAP, followed by 2 min of UV-A illumination. Constructs were then immersed in HUVEC culture medium, sterilized by UV-C irradiation for 20 min in a laminar flow bench, and stored overnight. The functionalized channels were perfused with 0.5 mL HUVEC suspension (1 × 10⁷ cells mL⁻¹). The petri dish containing the construct was then fully filled with culture medium, sealed using Parafilm, and fixated onto the bottom of an acrylic box. Fast cell sedimentation in the channel leading to inhomogeneous cell coverage was overcome by repeated rotation of the construct around the channel axis during the seeding process: The box was initially turned upside down and incubated for 15 min. The box was rotated 90° clockwise and again incubated for 15 min, and then rotated 180° counter-clockwise before incubating for another 15 min. The same cycle was conducted again to ensure that all parts of the channel walls were fully exposed to the cells. After 24 h incubation at 37 °C and 5% CO₂, the channels seeded with HUVECs were perfused with 0.5 mL of culture medium containing 2 µg mL⁻¹ calcein-AM and further incubated for 1 h. The samples were then characterized by confocal laser scanning microscope (LSM 700, Zeiss) using excitation at 488 nm. The vertical axis of the acquired confocal z-stack micrographs was corrected for the refractive index of the culture medium using the microscope software package (Zeiss Zen 2012 Black edition).

3.8.12 Multi-furcated 3D perfusion culture constructs

To demonstrate the perfusion of multi-furcated channel network as well as embedding cell-laden matrices in the culture chamber, constructs with a separate culture chamber and channel networks were printed in PEGDA. The channels were first perfused with 1 mL of 20 µg mL⁻¹ acryloxyethyl thiocarbamoyl rhodamine B (Sigma-Aldrich) solution containing 10 mg mL⁻¹ LAP, followed by 2 min of UV-A illumination. The unreacted rhodamine molecules were flushed away using DI water. The constructs were then immersed in 3T3 fibroblast culture medium overnight to exchange the DI water for medium in the PEGDA hydrogel. Before harvesting cells, 3T3 fibroblasts were stained with calcein-AM (2 µg mL⁻¹) in a culture flask for 1 h. Cell-laden GelMA solution was prepared by mixing warm (37 °C) LAP-containing GelMA solution in DPBS with an equivalent volume of 3T3 fibroblast suspension to reach final concentrations of 100 mg mL⁻¹ GelMA, 5 mg mL⁻¹ LAP and 5 × 10⁶ cells mL⁻¹. The culture chamber was then perfused with 0.5 mL of cell-laden GelMA solution, followed by 90 s of UV-A illumination. Both the intact sample and cross-sectional slices generated by manual

cutting were then immediately characterized by confocal laser scanning microscopy using excitation at 488 and 555 nm.

To test if the culture chamber can be fully filled with matrices for cell embedding using pipetting rather than perfusion, 0.02 wt. % fluorescence microbeads (\varnothing 2 μm , FluoSpheres carboxylate-modified microspheres, yellow-green fluorescence, Thermo Fisher Scientific) instead of cells were encapsulated in 100 mg mL^{-1} GelMA solution containing 1 mg mL^{-1} LAP, loaded into the culture chamber and crosslinked through 2 min of UV-A irradiation. Samples were then sectioned and characterized using confocal laser scanning microscopy.

For testing optimal LAP concentration for cell encapsulation, 200 μL of cell-laden pre-gel GelMA solutions with desired GelMA and LAP concentrations were added to a 48-well plate, followed by 2 min of UV-A irradiation. Then 500 μL of culture medium was added to each well. Samples were incubated for a desired period of time, with intermediate medium change every 2 days. Before visualization under confocal laser scanning microscopy using excitation at 488 and 555 nm, culture medium in each well was replaced with fresh medium containing 2 $\mu\text{g mL}^{-1}$ calcein-AM and 2 $\mu\text{g mL}^{-1}$ propidium iodide, and then incubated for another 1 h.

3.8.13 Perfusion culture in printed 3D hydrogel microfluidic chips

Before perfusion culture started, all the tubing was perfused by a large amount of 70% ethanol, followed by sterilized water using a multi-channel peristaltic pump (Watson-Marlow, 205U). The surfaces of all equipment, including water bath, sample incubator, the pump and the outer surfaces of the tubing were wiped with 70% ethanol prior to experiment. Printed samples immersed in DMEM culture medium supplemented with 2% v/v penicillin-streptomycin, along with all the glass bottles are sterilized by UV-C illumination for 20 min (254 nm, UV sterilization cabinet, Cleaver Scientific). Prior to cell loading, sterilized samples were transferred to a laminar flow bench after immersion in DMEM medium for overnight to exchange the water in the hydrogel for culture medium. Cell-laden GelMA solution was prepared by mixing warm (37 $^{\circ}\text{C}$) LAP-containing GelMA solution in DPBS with an equivalent volume of HT-29 cells suspension to reach final concentrations of 100 mg mL^{-1} GelMA, 1 mg mL^{-1} LAP and 1×10^7 cells mL^{-1} . Before cell loading, culture medium was partially removed so that samples were not submerged yet still moist, exposing the loading chamber to the atmosphere without severe dehydration of samples. The remaining liquid medium in the culture chamber was then completely removed by suction using a syringe connected to the needles as well as micro-tubing. The culture chamber was finally loaded by dropwise pipetting cell-laden GelMA solution into the chamber, followed by 2 min of UV-A illumination. Before connecting samples to the pump, extra culture medium was added to petri dish to submerge samples again and the dish was capped by a lid with holes covered by Parafilm. Needles that were pre-filled with culture medium were then inserted to the channel connectors in samples and the perfusion rate was set at 70 $\mu\text{L}/\text{min}$. After culture, samples were sectioned by manual cutting. The generated cross-sectional

slices were stained with calcein-AM ($2\text{ }\mu\text{g mL}^{-1}$, Invitrogen) and propidium iodide (PI, $2\text{ }\mu\text{g mL}^{-1}$, Sigma-Aldrich) for 1 h and then characterized by confocal laser scanning microscopy using excitation at 488 and 555 nm.

Chapter 4:

Multi-material stereolithographic printing

One of the current limitations of stereolithography is its limited capability of simultaneous printing of multiple materials. In contrast, extrusion-based printing can realize multi-material printing simply by implementing different printhead nozzles. Researchers have attempted multi-material stereolithographic printing by constantly changing and washing different resins between each layer fabrication.^{124,125,134,144,147,149–151,155,187,188} However, such an approach requires manual labor and thus is time consuming. Therefore, true multi-material stereolithographic printing requires sophisticated chemistries that allow for independent photopolymerization of different monomers using different photoinitiators and wavelengths, which is not a trivial task to accomplish. Multi-material printing in stereolithography is of particular interest in constructing advanced *in vitro* cell culture models because incorporation of materials of different properties to fulfill various chemical, physical and mechanical requirements can potentially mimic the highly heterogeneous nature of *in vivo* system, and, equally important, integrate soft biomimicking hydrogels in a stiff self-contained chip unit.

A dual material resin has previously been developed in the group based on both radical and cationic photopolymerization (**Figure 4.1**).¹⁸⁹ Two different monomers, namely acrylate and epoxy, can be independently polymerized by their respective photoinitiators that are activated *via* different wavelengths, to form a construct with widely tunable elasticity, from highly stiff epoxy to highly compliant PEGDA. Although the current perfusion setup is fairly robust to conduct long-term perfusion culture experiments, such hydrogel material of intermediate compliance still needs to be handled with much caution. Therefore, it would be very useful to print a multi-material perfusion construct with stiff perimeters serving as user-friendly world-to-chip interface (inlet/outlet) as well as with soft and diffusion-open interstitial volumes serving as cell culture unit.

The postdoc, Esben K.U. Larsen, who developed the multi-material resin also conducted preliminary 3D printing test using the home-built polychromic printer. Sudan I, which absorbs light at both 365 and 450 nm, was selected as photoabsorber to improve vertical printing resolution. After the postdoc left the group, two tasks were carried out as a side project in this thesis: 1) optimize epoxy and PEGDA printing concentration so printed epoxy and PEGDA within the same construct would swell to a similar degree in immersion medium and thus mechanical strain due to swelling could be minimized; 2) print a perfusion construct using an optimized resin formulation with both stiff epoxy as perimeters and soft PEGDA as channel walls.

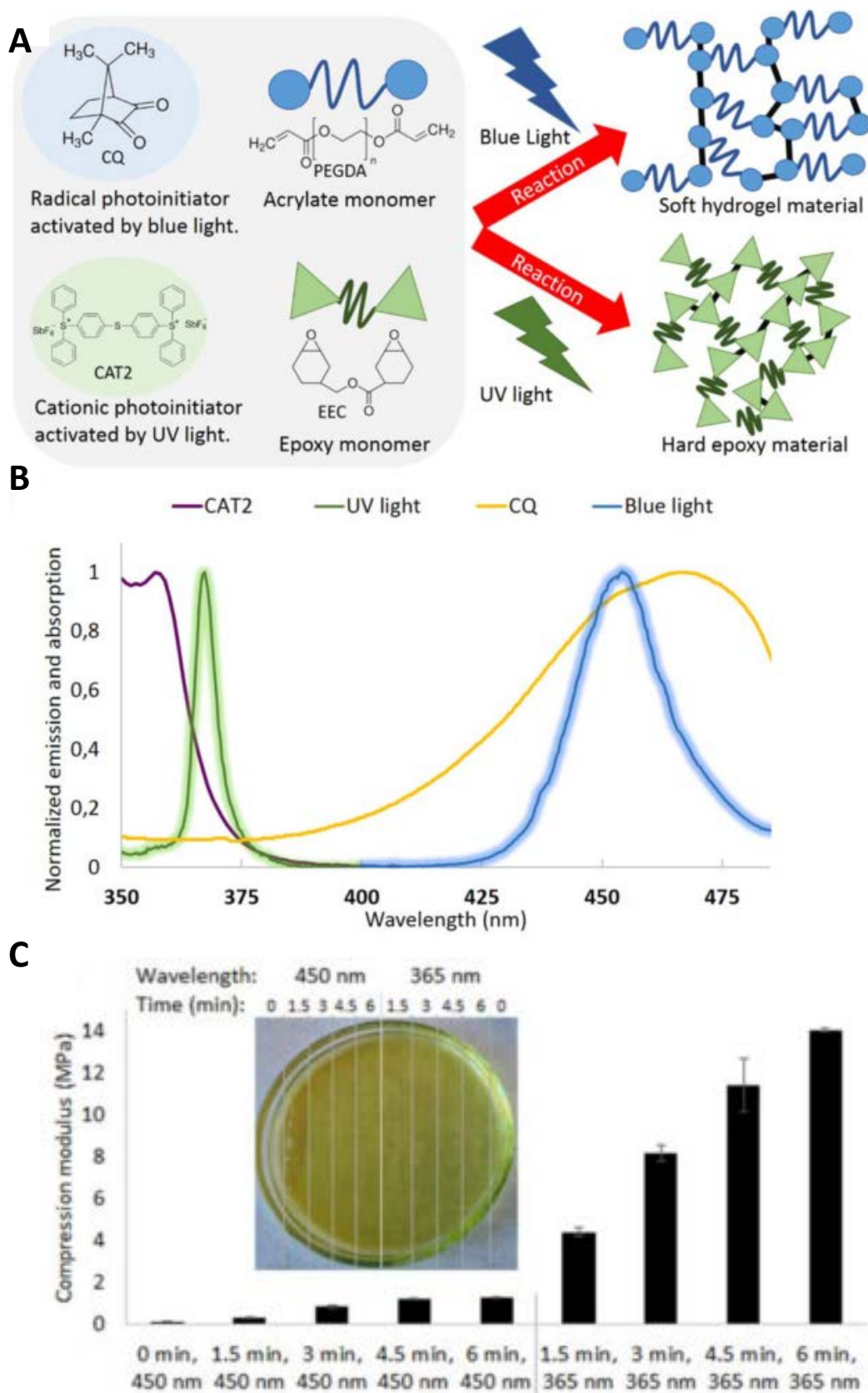


Figure 4.1 A) A schematic diagram of chemical reaction for CQ and CAT2 photoinitiation of the free radical polymerization of the acrylate (PEGDA) and the cationic polymerization of the epoxy component (EEC), respectively.¹⁸⁹ B) Normalized absorption of the CQ and CAT2 photoinitiators and normalized emission spectra of the blue (450 nm) and UV (365 nm) light source.¹⁸⁹ C) Compression

modulus of a solution containing 40% v/v EEC, 20% v/v PEGDA, CQ and CAT2 exposed with gradually increasing doses of either 450 or 365 nm light in a petri dish with the gradient of light duration and wavelength indicated. Error bars show the standard deviation of replicate measurements within the dish ($n = 3$).¹⁸⁹ Adapted from ref. 189.

4.1 Optimization of epoxy and PEGDA concentration

Unpublished data: The authors would like to keep this section confidential until they are published.

4.2 Printing and perfusion of dual-material constructs

Unpublished data: The authors would like to keep this section confidential until they are published.

4.3 Conclusion

Although still in the preliminary stage, our multi-material stereolithographic printing approach demonstrates the potential for printing perfusion constructs with stiff material as construct perimeters as well as soft material as diffusion-open microchannel walls. More work needs to be done in the future to further optimize printing configuration, characterize the diffusion behavior within printed PEGDA, and study the cell compatibility of the printed constructs.

4.4 Experimental section

4.4.1 Materials

Poly(ethylene glycol) diacrylate (M_n 700 g mol⁻¹, PEGDA), camphorquinone (CQ), triarylsulfonium hexafluoroantimonate salts (CAT2) (50 wt. % in propylene carbonate), 3,4-epoxycyclohexylmethyl 3,4-epoxycyclohexanecarboxylate (EEC), 1-phenylazo-2-naphthol (Sudan I), propylene carbonate (PC) and diethylene glycol diethyl ether (DGDE) were all purchased from Sigma-Aldrich and used as purchased.

4.4.2 Projection stereolithography of dual-material constructs

The printing procedures were almost the same as single material printing. Light exposure used both a 365-nm and 450-nm LED. The 3D design was exported separately as epoxy and PEGDA part, which were then independently sliced into a series of digital masks with a slicing thickness of 25 μ m using the open-source slicer software instead of 20 μ m used in single material printing. The resin was composed of 40% v/v PEGDA, 40% v/v EEC, 1 mg mL⁻¹ Sudan I, 20 mg mL⁻¹ CQ and 30 mg mL⁻¹ CAT2. Stock solutions of CQ and Sudan I were dissolved in DGDE. Prior to the addition of resin to the vat, aluminum foil was used to wrap the resin container to avoid premature crosslinking due to the ambient light. The digital masks from the two parts in the same layer were sequentially projected onto the vat bottom *via* their respective light source, UV exposure of 40 s for each epoxy layer and blue light

exposure of 70 s for each PEGDA layer. After printing, the object was immediately immersed in ethanol or PC for at least overnight to leach out remaining reagents and then transferred to a water bath prior to further use.

4.4.3 Perfusion of dual-material printed constructs

The same perfusion setup as mentioned before was applied. Briefly, blunt stainless needles (\varnothing 0.8 mm \times 22 mm) were mounted to polytetrafluoroethylene (PTFE) tubing ($\varnothing_{\text{inner}}$ 0.30 mm and $\varnothing_{\text{outer}}$ 0.50 mm) that was connected to a peristaltic pump (MasterFlex) via Luer Lock connectors. Printed constructs were fixated onto the bottom of a polystyrene petri dish using double sided adhesive tapes, and the petri dish filled with DI water. Aqueous solutions of both red and blue food dye (Dr. Oetker) were used as perfusion fluids. The tubing was pre-perfused with fluid to avoid bubbles, and the needles were inserted into the 3D printed inlet and outlet (\varnothing 0.7 mm). Pumping proceeded at a flow rate of 100 $\mu\text{L min}^{-1}$ and the channel perfusion was recorded by a phone camera.

Chapter 5:

Discussion

5.1 The advantages of our proposed approach

5.1.1 Direct embedding 3D complex and well-defined perfusion channel networks in hydrogel materials at high spatial resolutions

Our stereolithographic hydrogel printing approach for direct embedding of 3D complex perfusion channel networks within diffusion-open materials has advantages over conventional 2D microfluidic systems engineered *via* molding and replication approaches,^{43,66,73–78} which are labor intensive and can usually produce channel networks restricted to planar architectures. Alternatively, 3D hydrogel microfluidic systems have been achieved using extrusion-based 3D printing in combination with sacrificial molding.^{112–117} However, due to the fact that extruded sacrificial filaments tend to fold or collapse under their own weight, perfusion channel networks constructed through this approach have been mostly rectilinear lattice architectures with limited 3D topological complexity, contrary to the multi-furcated channel networks demonstrated in our approach.

Our optimized printing configuration results in the faithful printing of perfusable microchannels of cross-section as small as $100\ \mu\text{m} \times 100\ \mu\text{m}$. Although it still cannot compare to the sub-micro resolution achieved in conventional 2D microfluidics engineered in research labs through photolithography and PDMS molding, such spatial printing resolution for perfusable microchannels has not yet been reported in hydrogel materials using stereolithography, to our best knowledge. By manipulating the diameters of printhead nozzles, sacrificial filaments with a diameter of about $50\ \mu\text{m}$ have been extrusion printed and subsequently removed after hydrogel casting to form perfusable microchannels ($\varnothing\ 50\ \mu\text{m}$).¹¹⁵ Although smaller microchannels can be constructed using this approach, channels cannot be directly printed and are limited to cylindrical geometry. Furthermore, upon removal of sacrificial filaments, the formed microchannels are ultimately defined by their surrounding highly compliant hydrogels used for cell encapsulation, which challenge their long-term mechanical stability as well as structural fidelity. Researchers have also used undiluted highly crosslinked ultra-low MW PEGDA ($M_n\ 250\ \text{g mol}^{-1}$) to manufacture microchannels of cross-section as small as $18\ \mu\text{m} \times 20\ \mu\text{m}$ by stereolithography.^{145,146} However, the resulting constructs are so densely crosslinked that they resist swelling and are impermeable to water. Consequently, they are not considered as hydrogel materials and not suitable for constructing *in vitro* 3D cell culture models.

Therefore, our proposed stereolithographic hydrogel printing approach has advantages over other existing methods for direct embedding 3D complex well-defined perfusion channel networks in hydrogel materials at high spatial resolutions.

It should also be noted that we did not implement the smallest perfusable microchannels we can print for our perfusion culture constructs. Instead, we implemented

slightly larger microchannels (\varnothing 200 μm) because we wanted to achieve steady perfusion within a 3D complex channel network in a reproducible manner. As discussed in the previous chapter, small channels with sloped parts are more affected by the overcuring during printing, which is essential for manufacturing mechanically stable constructs through strong bonding between neighboring layers. Since sloped parts are inevitable when constructing complex channel networks in a full 3D manner, small channels pose extra challenges for steady perfusion throughout the whole fluidic network in cases where random channel blockage can occur and difference in fluidic resistance among multiple channels complicates the fluidic behaviors. We have introduced a solution to overcome this issue by enlarging the sloped parts of channels to minimize the effect of overcuring, as discussed previously. Although effective, such approach requires more bulky structural elements in channel network designs, which might limit the density of channels that we can achieve in a full 3D manner. Extra work needs to be conducted in the future to fully benefit from the high spatial resolution of our stereolithographic hydrogel printing approach. However, we believe this is highly achievable.

5.1.2 Diffusion-open and mechanically stable hydrogel constructs as self-contained 3D microfluidic chips that allow for long-term steady perfusion cultures

By using the PEGDA with suitable molecular weight, diffusion-open and mechanically stable hydrogel constructs have been achieved using our approach. The mechanical stability of printed constructs allows for long-term steady medium perfusion through channel network using a facile perfusion setup based on needles, microtubing and external pumping. The diffusional properties of printed constructs enables continuous diffusion of soluble factors such as oxygen and nutrients from channel network to culture volume, where cells are encapsulated in a different hydrogel material, and consequently can maintain a healthier cell culture in the long term. This is essential regardless of the intended applications of constructed 3D cell culture models, either as clinically useful replacements for damaged tissues or as *in vitro* models for scientific studies such as disease modeling and drug development. To our best knowledge, only few studies so far have reported long-term perfusion cell cultures in true 3D hydrogel microfluidic systems.¹¹⁶ Researchers have constructed a 3D cell culture entity that exceeded 1 cm in thickness with embedded lattice channel networks using extrusion printing in combination with sacrificial molding and consequently a healthy cell culture was maintained for weeks through medium perfusion.¹¹⁶ However, upon removal of the sacrificial materials, the formed channel networks were ultimately defined only by the highly compliant hydrogels used for cell encapsulation. The resulting construct's high compliance and limited long-term structural fidelity as well as stability thus challenge its use as self-contained perfusable *in vitro* systems. Consequently, an external perfusion chip device was integrated to maintain long-term perfusion and the fluidic channel networks were a bit distorted after perfusion (**Figure 1.16B**).¹¹⁶

Therefore, our approach has advantages over other existing methods for constructing mechanically stable, self-contained, 3D perfusable chip systems capable of supplying oxygen and nutrients through long-term medium perfusion in a reproducible manner.

5.2 The limitations of our proposed approach

5.2.1 Inability to encapsulate cells during fabrication and limited capability of incorporating multiple materials

Our printed PEGDA hydrogels, although allowing for compound diffusion, are not suitable for cell encapsulation due to their relatively high crosslinking density. Therefore, cells are encapsulated in a different hydrogel material and subsequently incorporated post-fabrication. PEGDA (M_n 700 g mol⁻¹), instead of those highly compliant hydrogel materials used for cell encapsulation, was chosen because our current focus is to address the challenge in constructing mechanically stable, self-contained and perfusable chip systems capable of supplying oxygen and nutrients to an integrated 3D culture volume in a reproducible manner. However, it will be indeed of interest to further develop resin formulations that can simultaneously encapsulate cells and produce mechanically stable structures. A potential solution will be to print mixture of high and low MW PEGDA in order to keep a balance between mechanical stability and cell encapsulation capability. Furthermore, the stereolithographic process itself also poses challenges in simultaneous cell encapsulation: a) the cytotoxicity of formed radicals during photopolymerization and b) cell settlement in liquid resin during fabrication. By tuning photoinitiator concentration¹⁶⁰ as well as using density gradient adjusting reagents to match the buoyant density of the cells with the resin,¹³⁸ the cytotoxicity and cell settlement can be overcome. In contrast, extrusion based bioprinting techniques can inherently enable simultaneous cell encapsulation by simply mixing cell suspensions with bioinks.^{9,10,19,79,82,88}

Stereolithography is mostly restricted to the use of a single material while extrusion-based technique can simultaneously print multiple materials by simply implementing multiple printhead nozzles. In our 3D hydrogel microfluidic culture chip system, a different type of material is incorporated post-printing by embedding a cell-laden hydrogel within the confines of a 3D printed PEGDA hydrogel chip. This approach can be scaled up by printing multiple culture volumes and subsequently incorporating multiple cellular matrices. However, post-fabrication cell loading can be challenging in terms of achieving effective filling of confined culture volumes, as discussed in the previous chapter. Our dual-material stereolithographic printing system, although demonstrating the ability to construct a PEGDA hydrogel perfusion channel network within the confines of stiff epoxy as a more robust “chip-to-the-world” interface, has some challenges that need to be overcome before living up to its full potential, such as difference in swelling properties among multiple materials and the channel connectivity at PEGDA/epoxy interface, as discussed in the previous chapter. Furthermore, adding a third material component in multi-material stereolithographic

printing is far from a trivial task. It requires even more sophisticated chemistries, where multiple components can be independently polymerized using different light wavelengths, as well as extensive studies regarding post-printing handling of the printed constructs where the interfaces between different components can maintain intact.

Therefore, developing more advanced resin formulations that can encapsulate cells as well as allow for multi-material printing will be of particular interest in manufacturing advanced *in vitro* cell culture models that highly mimic the heterogeneous nature of *in vivo* system by stereolithography.

5.2.2 Inability to establish direct cell-cell contact between cells cultured in different compartments within the same culture chip

Our printed PEGDA hydrogel chips allow for diffusive paracrine signaling but not for direct cell-cell contact, either between the endothelial cells in the channel networks and the cells cultured in a separate printed compartment, or between the cells in different compartments, due to their nanoporous structures. This limitation may be circumvented by including micro-fenestrations in chip designs, as demonstrated previously in 2D microfluidic cell culture systems (**Figure 1.7D,E**).^{33,43,60,66,190} However, such micro-fenestrations not only need to be large enough to enable cell-cell contact but also small enough to retain their functions as structural confines, which usually are within the range from a few microns to tens of microns and consequently challenge the current spatial resolution that can be achieved by our printing configurations. Furthermore, direct cell-cell contact requires close proximity between cells ($< 50\ \mu\text{m}$),¹⁹¹ indicating our printed channel networks and culture compartments should be only separated by very thin confines. This is challenging because the mechanical instability of a printed thin as well as perforated PEGDA layer might compromise the structural fidelity of the whole construct. Those challenges need to be addressed before we can implement micro-fenestrations in our chip designs to enable direct cell-cell contact.

5.3 Summary and future work

Extrusion bioprinting of cell-laden hydrogels used in combination with sacrificial molding is certainly a very useful and versatile technique, which is currently the most widely used technique for constructing 3D cell culture models. However, it also poses significant challenges in mechanical stability of a self-contained perfusable chip device as well as in the obtainable spatial resolution and 3D complexity of the perfusion fluidic network. In comparison, we have taken a distinctly different approach to address those challenges by manufacturing a mechanically stable and self-contained 3D perfusable chip that supplies oxygen as well as nutrients to maintain a long-term healthy culture of cells embedded in alternative soft hydrogels in a separate culture compartment, which is essential for 3D cell culture models regardless of the intended applications. However, our approach also poses

major challenges in cell encapsulation during fabrication, simultaneous incorporation of multiple materials and types of cells, as well as allowing for both short (juxtacrine signaling) and long distance (paracrine signaling) cell-cell communication. Those challenges limit the biological relevance/complexity that can be currently achieved by our approach in comparison with extrusion bioprinting.

A promising direction in the future might be to develop a hybrid printing platform where extrusion printing is used in combination with stereolithography to produce 3D cell culture models with both structural and biological complexity.

There are many things that we have not investigated in the scope of this study but might be of interest for the future work, such as how the endothelial cells seeded inside the channel networks would regulate compound transport, how flow rate would affect the outcome of perfusion cultures, and how the cellular microenvironment modulated by compound perfusion through channel network would affect various cellular behaviors other than cell viability.

Chapter 6:

Conclusion and outlook

The main aim of this work was to develop methods to 3D print diffusion-open and mechanically stable hydrogel constructs as self-contained 3D microfluidic chips at high spatial resolutions.

One of the sub-goals of this project was to develop a cost-efficient resin for printing diffusion-open yet mechanically stable hydrogel constructs with embedded 3D microfluidic channels as artificial vascular-like network. By employing commercially available starting materials at reasonable cost, 3D PEGDA hydrogel microfluidic culture chips of intermediate compliance with embedded multi-furcated channel networks have been fabricated using an optimized stereolithographic 3D printing configuration. A systematic approach has been adopted to investigate the combined effect of multiple experimental parameters on the structural fidelity of printed microchannels. The optimized printing configuration results in the faithful printing of perfusable microchannels of cross-section as small as $100\text{ }\mu\text{m} \times 100\text{ }\mu\text{m}$. By characterizing the time dependent diffusion distance of a perfused dyed liquid inside a printed microchannel, well-fitted diffusion kinetics have been observed within printed PEGDA hydrogels. Cellular components are incorporated post-fabrication by embedding cell-laden matrices within the confines of printed PEGDA culture compartments.

Another sub-goal of this project was to develop a facile platform for steady and long-term perfusion of printed hydrogel microfluidic culture chips. By employing commercial flexible micro-tubing and blunt syringe needles, a facile perfusion setup has been developed and resulted in stable leak-free perfusion of printed hydrogel culture chips for at least a week. Due to the mechanical stability of printed hydrogel culture chips, needles mounted to the micro-tubing can be inserted into printed channel connectors, and the connection between the micro-tubing and external pump can be easily made *via* widely used Luer locks and regular tubing.

A third sub-goal of this project was to develop a long-term perfusion culture platform using printed hydrogel 3D microfluidic culture chips. Due to the simplicity of the established perfusion setup, all equipment can be easily sterilized separately. Physicochemical properties that are important for a cell culture environment such as pH, temperature and oxygen tension, are maintained by implementing a commonly used circulating water bath, a microscope stage incubator and an external gas supply. Long-term perfusion culture for a week within printed hydrogel microfluidic chips has been demonstrated without notable contamination using this facile platform. The incorporated microfluidic channel network has proven to be essential to maintain a healthy 3D cell culture in the long term.

By the end of this project, all the main goals have been achieved. In addition, multi-material stereolithographic printing has also been attempted in this project. Although still in the preliminary stage, our dual-material printing approach based on independent

photopolymerization mechanisms has demonstrated the potential for manufacturing perfusion systems with heterogeneous materials fulfilling different purposes, namely highly stiff epoxy component serving as structural supports and soft PEGDA component serving as cell culture unit.

Two printing systems have been studied in this project, one is based on a commercial stereolithography printer and the other is based on a home-built polychromatic stereolithography printer. The commercial system offers limited flexibility in changing experimental configurations, but is a good start point for researchers who want to work on 3D printing without experience or access to customized systems. We believe the presented approach in this thesis for modifying the commercial system to print hydrogel materials can serve as a useful guideline for beginners. On the other hand, the home-built system requires expertise in machinery and optics for construction, but offers great flexibility in exploring multiple experimental parameters as well as better resolution. It should be noted that although the construction of the printer requires trained personnel, the use of the optimized system is quite straightforward and demands minimal labor.

In summary, we have addressed the challenge of construction as well as perfusion of a mechanically stable and self-contained 3D perfusable chip system that supplies oxygen and nutrients to maintain a long-term healthy culture of cells embedded in alternative soft hydrogels in a separate printed culture compartment *via* a reproducible and highly automated process. We believe this proposed approach will enable faster translation of 3D *in vitro* chip culture technologies to become a standard accessible and reliable technology both in the biological and medical sciences and, in particular, in industrial and clinical settings.

However, some major challenges specifically relevant to our approach need to be addressed in the future work, such as cell encapsulation during fabrication, simultaneous incorporation of multiple materials and types of cells, as well as allowing for both short (juxtacrine signaling) and long distance (paracrine signaling) cell-cell communication. Those challenges may be overcome by developing more advanced resin formulations that can simultaneously produce mechanically stable constructs and encapsulate cells, as well as by incorporating micro-fenestrations into our chip designs. Also, future work has to be performed to validate the proposed approach with respect to its use as fully functional *in vitro* models. So far only cell viability has been investigated in this project. Future studies should focus on detailed investigation of long-term cell culture behavior regarding specific functionalities in 3D when the cellular microenvironment is modulated by compound perfusion through the vascular network-like constructs.

In addition, some general challenges presented in *in vitro* 3D cell culture models are also worth special attention in the future.

Firstly, characterization methods need to be developed accordingly in order to fully benefit from a complex 3D culture model. Commonly used end-point assays in biological research cannot be easily applied to 3D culture models without complex 3D structural

elements obstructing the assay. Meanwhile retrieving or abstracting cells from the models is not a trivial task. Furthermore, optical imaging in 3D is very challenging due to light scattering among biomaterials and cells. Few reports have been published on imaging through an intact 3D cell culture entity.^{192,193} On the other hand, sectioning of samples to obtain perfect slices for microscopy is also difficult, which usually requires sophisticated equipment not only for sectioning but also for preserving biological structures during the process. Therefore, versatile characterization methods are in great demand for abstracting valuable information from complex 3D culture models more efficiently.

Secondly, due to the complexity of native biological systems, it is still unclear to what degree the *in vitro* microenvironment should be engineered to elicit desired biological response. Such task calls for continuous communications and collaborations among researchers with different expertise, such as material chemists, biologists and engineers.

Acknowledgements

I would like to thank everyone who has contributed to this thesis, especially:

My supervisor Prof. Niels B. Larsen, for being such a wonderful and dedicated mentor throughout the whole project, who has constantly provided me with practical guidance as well as inspirations. I'm always impressed by how knowledgeable you are on so many topics, how often you are just able to pop any equation on a blackboard and how involved you still are with experiments. Also thank you for your unwavering optimism to balance my realism. Without your help, this thesis would've not been possible.

I would also like to thank existing and former members of the Polycell group at DTU Nanotech for all the help and interesting discussions inside and outside the labs: Esben, for being such a great lab partner and making lab full of laughter; Adele, for helping me when I first started in the lab; Rie, for many interesting cultural discussions when we were at the conference; Milan, for many interesting discussions; Sarah, Maryam, and Mikkel, for helping me on the project.

I would also like to thank all the people who have helped me with my daily work, either on technical or administrative support: Jannik, Ole, Lotte, Lene and Louise. And I'd like to thank Jesper for taking the cover pictures of this thesis.

I would also like to thank all my friends for making life outside work much more enjoyable, especially:

Ada, for being such a wonderful friend who has driven me around all over the Europe, introducing me to various European cultures and teaching me all those specific terms for food ingredients and so on. For always taking care of everyone when we travel and for always cheering me up when I'm down. And for always being so organized and thoughtful.

Feng, for being such a wonderful friend, understanding and supporting me for more than a decade. 一言以蔽之，海内存知己，天涯若比邻。

Andreas, for being a great friend and introducing me to the Danish culture when I came to Denmark for the very first time.

Jon, for being such a great accompany in the office with so many interesting discussions.

Janko, for being there when I got drunk for the first time in my life.

Last but not least, I would like to thank my family, especially my parents for their unconditional love and support, for their understanding of me being such an absent son during the past few years. Also I'd like to dedicate this thesis to my late grandfather who passed way shortly after I started my PhD.

(在此，我想感谢我的家人，感谢他们自始至终的关爱与支持。尤其感谢我的父母，以及阿姨，感谢您们对我这几年的缺席表示谅解。同时，谨以此文献给我过世的爷爷，愿他老人家在另一个世界能尽享天伦。)

Finishing this thesis marks the ending of an important chapter of my life. While overwhelmed by all those precious memories during the past three years, I'm also looking forward to the next chapter. As a Chinese poet once wrote,

As I've chosen to travel to the distant, I shall endure whatever is coming on the way. (既然选择了远方，便只顾风雨兼程)

Reference

- (1) Haycock, J. W. *3D Cell Culture*; Haycock, J. W., Ed.; Methods in Molecular Biology; Humana Press: Totowa, NJ, 2011; Vol. 695.
- (2) Frohlich, E. M.; Charest, J. L. *Microfluidic Cell Culture Systems*; 2013.
- (3) Meyvantsson, I.; Beebe, D. J. Cell Culture Models in Microfluidic Systems. *Annu. Rev. Anal. Chem.* **2008**, *1* (1), 423–449 DOI: 10.1146/annurev.anchem.1.031207.113042.
- (4) Lee, J.; Cuddihy, M. J.; Kotov, N. A. Three-dimensional cell culture matrices: state of the art. *Tissue Eng. B, Rev.* **2008**, *14* (1), 61–86 DOI: 10.1089/teb.2007.0150.
- (5) Young, E. W. K.; Beebe, D. J. Fundamentals of microfluidic cell culture in controlled microenvironments. *Chem. Soc. Rev.* **2010**, *39* (3), 1036 DOI: 10.1039/b909900j.
- (6) Edmondson, R.; Broglie, J. J.; Adcock, A. F.; Yang, L. Three-dimensional cell culture systems and their applications in drug discovery and cell-based biosensors. *Assay Drug Dev. Technol.* **2014**, *12* (4), 207–218 DOI: 10.1089/adt.2014.573.
- (7) Vanderburgh, J.; Sterling, J. A.; Guelcher, S. A. 3D Printing of Tissue Engineered Constructs for In Vitro Modeling of Disease Progression and Drug Screening. *Ann. Biomed. Eng.* **2016**, *45* (1), 1–16 DOI: 10.1007/s10439-016-1640-4.
- (8) Ozbolat, I. T.; Ozbolat, I. T. 09-Applications of 3D Bioprinting. In *3D Bioprinting*; 2017; pp 271–312.
- (9) Zhang, Y. S.; Duchamp, M.; Oklu, R.; Ellisen, L. W.; Langer, R.; Khademhosseini, A. Bioprinting the Cancer Microenvironment. *ACS Biomater. Sci. Eng.* **2016**, *2* (10), 1710–1721 DOI: 10.1021/acsbiomaterials.6b00246.
- (10) Pati, F.; Gantelius, J.; Svahn, H. A. 3D Bioprinting of Tissue/Organ Models. *Angew. Chemie Int. Ed.* **2016**, *55* (15), 4650–4665 DOI: 10.1002/anie.201505062.
- (11) Li, X. (James); Valadez, A. V; Zuo, P.; Nie, Z. Microfluidic 3D cell culture: potential application for tissue-based bioassays. *Bioanalysis* **2012**, *4* (12), 1509–1525 DOI: 10.4155/bio.12.133.
- (12) Beebe, D. J.; Mensing, G. A.; Walker, G. M. Physics and Applications of Microfluidics in Biology. *Annu. Rev. Biomed. Eng.* **2002**, *4* (1), 261–286 DOI: 10.1146/annurev.bioeng.4.112601.125916.
- (13) Grimes, D. R.; Kelly, C.; Bloch, K.; Partridge, M. A method for estimating the oxygen consumption rate in multicellular tumour spheroids. *J. R. Soc. Interface* **2014**, *11* (92), 20131124–20131124 DOI: 10.1098/rsif.2013.1124.
- (14) Novosel, E. C.; Kleinhans, C.; Kluger, P. J. Vascularization is the key challenge in tissue engineering. *Adv. Drug Deliv. Rev.* **2011**, *63* (4–5), 300–311 DOI: 10.1016/j.addr.2011.03.004.
- (15) Risau, W.; Flamme, I. V asculogenesis. *Annu. Rev. Cell Dev. Biol.* **1995**, *11*, 73–91.
- (16) Laschke, M. W.; Harder, Y.; Amon, M.; Martin, I.; Farhadi, J.; Ring, A.; Torio-Padron, N.; Schramm, R.; Rücker, M.; Junker, D.; et al. Angiogenesis in Tissue Engineering: Breathing Life into Constructed Tissue Substitutes. *Tissue Eng.* **2006**, *12* (8), 2093–2104 DOI: 10.1089/ten.2006.12.2093.
- (17) Kirchmayer, D. M.; Gorkin III, R.; in het Panhuis, M. An overview of the suitability of hydrogel-forming polymers for extrusion-based 3D-printing. *J. Mater. Chem. B* **2015**, *3* (20), 4105–4117 DOI: 10.1039/C5TB00393H.
- (18) Jungst, T.; Smolan, W.; Schacht, K.; Scheibel, T.; Groll, J. Strategies and Molecular Design Criteria for 3D Printable Hydrogels. *Chem. Rev.* **2016**, *116* (3), 1496–1539 DOI: 10.1021/acs.chemrev.5b00303.
- (19) Albritton, J. L.; Miller, J. S. 3D bioprinting: improving in vitro models of metastasis with heterogeneous tumor microenvironments. *Dis. Model. Mech.* **2017**, *10* (1), 3–14 DOI: 10.1242/dmm.025049.
- (20) Jorfi, M.; D’Avanzo, C.; Kim, D. Y.; Irimia, D. Three-Dimensional Models of the Human

- Brain Development and Diseases. *Adv. Healthc. Mater.* **2017**, 1700723, 1700723 DOI: 10.1002/adhm.201700723.
- (21) Godoi, F. C.; Prakash, S.; Bhandari, B. R. 3d printing technologies applied for food design: Status and prospects. *J. Food Eng.* **2016**, 179, 44–54 DOI: 10.1016/j.jfoodeng.2016.01.025.
 - (22) Weaver, V. M.; Petersen, O. W.; Wang, F.; Larabell, C. A.; Briand, P.; Damsky, C.; Bissell, M. J. Reversion of the Malignant Phenotype of Human Breast Cells in Three-Dimensional Culture and In Vivo by Integrin Blocking Antibodies. *J. Cell Biol.* **1997**, 137 (1), 231–245 DOI: 10.1083/jcb.137.1.231.
 - (23) Kim, S.-S.; Sun Park, M.; Jeon, O.; Yong Choi, C.; Kim, B.-S. Poly(lactide-co-glycolide)/hydroxyapatite composite scaffolds for bone tissue engineering. *Biomaterials* **2006**, 27 (8), 1399–1409 DOI: 10.1016/j.biomaterials.2005.08.016.
 - (24) Gupta, N.; Liu, J. R.; Patel, B.; Solomon, D. E.; Vaidya, B.; Gupta, V. Microfluidics-based 3D cell culture models: Utility in novel drug discovery and delivery research. *Bioeng. Transl. Med.* **2016**, 1 (1), 63–81 DOI: 10.1002/btm2.10013.
 - (25) Walker, G. M.; Zeringue, H. C.; Beebe, D. J. Microenvironment design considerations for cellular scale studies. *Lab Chip* **2004**, 4 (2), 91 DOI: 10.1039/b311214d.
 - (26) Martin, I.; Wendt, D.; Heberer, M. The role of bioreactors in tissue engineering. *Trends Biotechnol.* **2004**, 22 (2), 80–86 DOI: 10.1016/j.tibtech.2003.12.001.
 - (27) Sackmann, E. K.; Fulton, A. L.; Beebe, D. J. The present and future role of microfluidics in biomedical research. *Nature* **2014**, 507 (7491), 181–189 DOI: 10.1038/nature13118.
 - (28) Bhattacharjee, N.; Urrios, A.; Kang, S.; Folch, A. The upcoming 3D-printing revolution in microfluidics. *Lab Chip* **2016**, 16 (10), 1720–1742 DOI: 10.1039/C6LC00163G.
 - (29) Huh, D.; Hamilton, G. A.; Ingber, D. E. From 3D cell culture to organs-on-chips. *Trends Cell Biol.* **2011**, 21 (12), 745–754 DOI: 10.1016/j.tcb.2011.09.005.
 - (30) Lee, J.; Kim, J.; Kim, H.; Bae, Y. M.; Lee, K.-H.; Cho, H. J. Effect of thermal treatment on the chemical resistance of polydimethylsiloxane for microfluidic devices. *J. Micromechanics Microengineering* **2013**, 23 (3), 35007 DOI: 10.1088/0960-1317/23/3/035007.
 - (31) Wu, J.; Wu, X.; Lin, F. Recent developments in microfluidics-based chemotaxis studies. *Lab Chip* **2013**, 13 (13), 2484 DOI: 10.1039/c3lc50415h.
 - (32) Sung, K. E.; Yang, N.; Pehlke, C.; Keely, P. J.; Eliceiri, K. W.; Friedl, A.; Beebe, D. J. Transition to invasion in breast cancer: a microfluidic in vitro model enables examination of spatial and temporal effects. *Integr. Biol.* **2011**, 3 (4), 439–450 DOI: 10.1039/C0IB00063A.
 - (33) Ugolini, G. S.; Visone, R.; Redaelli, A.; Moretti, M.; Rasponi, M. Generating Multicompartmental 3D Biological Constructs Interfaced through Sequential Injections in Microfluidic Devices. *Adv. Healthc. Mater.* **2017**, 6 (10), 1601170 DOI: 10.1002/adhm.201601170.
 - (34) Lin, B.; Levchenko, A. Spatial Manipulation with Microfluidics. *Front. Bioeng. Biotechnol.* **2015**, 3 (April), 1–6 DOI: 10.3389/fbioe.2015.00039.
 - (35) Moraes, C.; Mehta, G.; Leshner-Perez, S. C.; Takayama, S. Organs-on-a-Chip: A Focus on Compartmentalized Microdevices. *Ann. Biomed. Eng.* **2012**, 40 (6), 1211–1227 DOI: 10.1007/s10439-011-0455-6.
 - (36) Huang, Y.; Williams, J. C.; Johnson, S. M. Brain slice on a chip: opportunities and challenges of applying microfluidic technology to intact tissues. *Lab Chip* **2012**, 12 (12), 2103 DOI: 10.1039/c2lc21142d.
 - (37) Kilic, O.; Pamies, D.; Lavell, E.; Schiapparelli, P.; Feng, Y.; Hartung, T.; Bal-Price, A.; Hogberg, H. T.; Quinones-Hinojosa, A.; Guerrero-Cazares, H.; et al. Brain-on-a-chip model enables analysis of human neuronal differentiation and chemotaxis. *Lab Chip* **2016**, 16 (21), 4152–4162 DOI: 10.1039/C6LC00946H.

- (38) Kunze, A.; Giugliano, M.; Valero, A.; Renaud, P. Micropatterning neural cell cultures in 3D with a multi-layered scaffold. *Biomaterials* **2011**, *32* (8), 2088–2098 DOI: 10.1016/j.biomaterials.2010.11.047.
- (39) Adriani, G.; Ma, D.; Pavesi, A.; Kamm, R. D.; Goh, E. L. K. A 3D neurovascular microfluidic model consisting of neurons, astrocytes and cerebral endothelial cells as a blood–brain barrier. *Lab Chip* **2017**, *17* (3), 448–459 DOI: 10.1039/C6LC00638H.
- (40) Grosberg, A.; Alford, P. W.; McCain, M. L.; Parker, K. K. Ensembles of engineered cardiac tissues for physiological and pharmacological study: Heart on a chip. *Lab Chip* **2011**, *11* (24), 4165 DOI: 10.1039/c1lc20557a.
- (41) Marsano, A.; Conficconi, C.; Lemme, M.; Occhetta, P.; Gaudiello, E.; Votta, E.; Cerino, G.; Redaelli, A.; Rasponi, M. Beating heart on a chip: a novel microfluidic platform to generate functional 3D cardiac microtissues. *Lab Chip* **2016**, *16* (3), 599–610 DOI: 10.1039/C5LC01356A.
- (42) Jang, K.-J.; Suh, K.-Y. A multi-layer microfluidic device for efficient culture and analysis of renal tubular cells. *Lab Chip* **2010**, *10* (1), 36–42 DOI: 10.1039/B907515A.
- (43) Wang, L.; Tao, T.; Su, W.; Yu, H.; Yu, Y.; Qin, J. A disease model of diabetic nephropathy in a glomerulus-on-a-chip microdevice. *Lab Chip* **2017**, *17* (10), 1749–1760 DOI: 10.1039/C7LC00134G.
- (44) Kim, M. S.; Yeon, J. H.; Park, J.-K. A microfluidic platform for 3-dimensional cell culture and cell-based assays. *Biomed. Microdevices* **2007**, *9* (1), 25–34 DOI: 10.1007/s10544-006-9016-4.
- (45) Carraro, A.; Hsu, W.-M.; Kulig, K. M.; Cheung, W. S.; Miller, M. L.; Weinberg, E. J.; Swart, E. F.; Kaazempur-Mofrad, M.; Borenstein, J. T.; Vacanti, J. P.; et al. In vitro analysis of a hepatic device with intrinsic microvascular-based channels. *Biomed. Microdevices* **2008**, *10* (6), 795–805 DOI: 10.1007/s10544-008-9194-3.
- (46) Chang, R.; Nam, J.; Sun, W. Direct Cell Writing of 3D Microorgan for In Vitro Pharmacokinetic Model. *Tissue Eng. Part C Methods* **2008**, *14* (2), 157–166 DOI: 10.1089/ten.tec.2007.0392.
- (47) Toh, Y.-C.; Lim, T. C.; Tai, D.; Xiao, G.; van Noort, D.; Yu, H. A microfluidic 3D hepatocyte chip for drug toxicity testing. *Lab Chip* **2009**, *9* (14), 2026 DOI: 10.1039/b900912d.
- (48) Domansky, K.; Inman, W.; Serdy, J.; Dash, A.; Lim, M. H. M.; Griffith, L. G. Perfused multiwell plate for 3D liver tissue engineering. *Lab Chip* **2010**, *10* (1), 51–58 DOI: 10.1039/B913221J.
- (49) Rennert, K.; Steinborn, S.; Gröger, M.; Ungerböck, B.; Jank, A.-M.; Ehgartner, J.; Nietzsche, S.; Dinger, J.; Kiehntopf, M.; Funke, H.; et al. A microfluidically perfused three dimensional human liver model. *Biomaterials* **2015**, *71*, 119–131 DOI: 10.1016/j.biomaterials.2015.08.043.
- (50) Liu, W.; Tian, C.; Yan, M.; Zhao, L.; Ma, C.; Li, T.; Xu, J.; Wang, J. Heterotypic 3D tumor culture in a reusable platform using pneumatic microfluidics. *Lab Chip* **2016**, *16* (21), 4106–4120 DOI: 10.1039/C6LC00996D.
- (51) Du, Y.; Li, N.; Yang, H.; Luo, C.; Gong, Y.; Tong, C.; Gao, Y.; Lü, S.; Long, M. Mimicking liver sinusoidal structures and functions using a 3D-configured microfluidic chip. *Lab Chip* **2017**, *17* (5), 782–794 DOI: 10.1039/C6LC01374K.
- (52) Chrobak, K. M.; Potter, D. R.; Tien, J. Formation of perfused, functional microvascular tubes in vitro. *Microvasc. Res.* **2006**, *71* (3), 185–196 DOI: 10.1016/j.mvr.2006.02.005.
- (53) Chung, S.; Sudo, R.; Vickerman, V.; Zervantonakis, I. K.; Kamm, R. D. Microfluidic Platforms for Studies of Angiogenesis, Cell Migration, and Cell–Cell Interactions. *Ann. Biomed. Eng.* **2010**, *38* (3), 1164–1177 DOI: 10.1007/s10439-010-9899-3.
- (54) Zervantonakis, I. K.; Hughes-Alford, S. K.; Charest, J. L.; Condeelis, J. S.; Gertler, F. B.; Kamm, R. D. Three-dimensional microfluidic model for tumor cell intravasation and

- endothelial barrier function. *Proc. Natl. Acad. Sci.* **2012**, *109* (34), 13515–13520 DOI: 10.1073/pnas.1210182109.
- (55) Zheng, Y.; Chen, J.; Craven, M.; Choi, N. W.; Totorica, S.; Diaz-Santana, A.; Kermani, P.; Hempstead, B.; Fischbach-Teschl, C.; Lopez, J. A.; et al. In vitro microvessels for the study of angiogenesis and thrombosis. *Proc. Natl. Acad. Sci.* **2012**, *109* (24), 9342–9347 DOI: 10.1073/pnas.1201240109.
 - (56) Kim, S.; Lee, H.; Chung, M.; Jeon, N. L. Engineering of functional, perfusable 3D microvascular networks on a chip. *Lab Chip* **2013**, *13* (8), 1489 DOI: 10.1039/c3lc41320a.
 - (57) Bischel, L. L.; Young, E. W. K.; Mader, B. R.; Beebe, D. J. Tubeless microfluidic angiogenesis assay with three-dimensional endothelial-lined microvessels. *Biomaterials* **2013**, *34* (5), 1471–1477 DOI: 10.1016/j.biomaterials.2012.11.005.
 - (58) Grafton, M. M. G.; Wang, L.; Vidi, P.-A.; Leary, J.; Lelièvre, S. a. Breast on-a-chip: mimicry of the channeling system of the breast for development of theranostics. *Integr. Biol.* **2011**, *3* (4), 451 DOI: 10.1039/c0ib00132e.
 - (59) Gioiella, F.; Urciuolo, F.; Imparato, G.; Brancato, V.; Netti, P. A. An Engineered Breast Cancer Model on a Chip to Replicate ECM-Activation In Vitro during Tumor Progression. *Adv. Healthc. Mater.* **2016**, *5* (23), 3074–3084 DOI: 10.1002/adhm.201600772.
 - (60) Huh, D.; Matthews, B. D.; Mammoto, A.; Montoya-Zavala, M.; Hsin, H. Y.; Ingber, D. E. Reconstituting Organ-Level Lung Functions on a Chip. *Science* (80-.). **2010**, *328* (5986), 1662–1668 DOI: 10.1126/science.1188302.
 - (61) Kim, H. J.; Huh, D.; Hamilton, G.; Ingber, D. E. Human gut-on-a-chip inhabited by microbial flora that experiences intestinal peristalsis-like motions and flow. *Lab Chip* **2012**, *12* (12), 2165 DOI: 10.1039/c2lc40074j.
 - (62) Na, K.; Lee, M.; Shin, H.-W.; Chung, S. In vitro nasal mucosa gland-like structure formation on a chip. *Lab Chip* **2017**, *17* (9), 1578–1584 DOI: 10.1039/C6LC01564F.
 - (63) Nguyen, D. T. T.; van Noort, D.; Jeong, I.-K.; Park, S. Endocrine system on chip for a diabetes treatment model. *Biofabrication* **2017**, *9* (1), 15021 DOI: 10.1088/1758-5090/aa5cc9.
 - (64) Sung, J. H.; Shuler, M. L. A micro cell culture analog (μ CCA) with 3-D hydrogel culture of multiple cell lines to assess metabolism-dependent cytotoxicity of anti-cancer drugs. *Lab Chip* **2009**, *9* (10), 1385 DOI: 10.1039/b901377f.
 - (65) Zhang, C.; Zhao, Z.; Abdul Rahim, N. A.; van Noort, D.; Yu, H. Towards a human-on-chip: Culturing multiple cell types on a chip with compartmentalized microenvironments. *Lab Chip* **2009**, *9* (22), 3185 DOI: 10.1039/b915147h.
 - (66) Kim, S.; Chung, M.; Ahn, J.; Lee, S.; Jeon, N. L. Interstitial flow regulates the angiogenic response and phenotype of endothelial cells in a 3D culture model. *Lab Chip* **2016**, *16* (21), 4189–4199 DOI: 10.1039/C6LC00910G.
 - (67) Borenstein, J. T.; Weinberg, E. J.; Orrick, B. K.; Sundback, C.; Kaazempur-Mofrad, M. R.; Vacanti, J. P. Microfabrication of Three-Dimensional Engineered Scaffolds. *Tissue Eng.* **2007**, *13* (8), 1837–1844 DOI: 10.1089/ten.2006.0156.
 - (68) Kniazeva, T.; Hsiao, J. C.; Charest, J. L.; Borenstein, J. T. A microfluidic respiratory assist device with high gas permeance for artificial lung applications. *Biomed. Microdevices* **2011**, *13* (2), 315–323 DOI: 10.1007/s10544-010-9495-1.
 - (69) Li, N.; Schwartz, M.; Ionescu-Zanetti, C. PDMS compound adsorption in context. *J. Biomol. Screen.* **2009**, *14* (2), 194–202 DOI: 10.1177/1087057108327326.
 - (70) King, K. R.; Wang, C. C. J.; Kaazempur-Mofrad, M. R.; Vacanti, J. P.; Borenstein, J. T. Biodegradable Microfluidics. *Adv. Mater.* **2004**, *16* (22), 2007–2012 DOI: 10.1002/adma.200306522.
 - (71) Lenguito, G.; Chaimov, D.; Weitz, J. R.; Rodriguez-Diaz, R.; Rawal, S. A. K.; Tamayo-

- Garcia, A.; Caicedo, A.; Stabler, C. L.; Buchwald, P.; Agarwal, A. Resealable, optically accessible, PDMS-free fluidic platform for ex vivo interrogation of pancreatic islets. *Lab Chip* **2017**, *17* (5), 772–781 DOI: 10.1039/C6LC01504B.
- (72) Sticker, D.; Rothbauer, M.; Lechner, S.; Hehenberger, M.-T.; Ertl, P. Multi-layered, membrane-integrated microfluidics based on replica molding of a thiol–ene epoxy thermoset for organ-on-a-chip applications. *Lab Chip* **2015**, *15* (24), 4542–4554 DOI: 10.1039/C5LC01028D.
- (73) Paguirigan, a; Beebe, D. J. Gelatin based microfluidic devices for cell culture. *Lab Chip* **2006**, *6* (3), 407 DOI: 10.1039/b517524k.
- (74) Cheng, S.-Y.; Heilman, S.; Wasserman, M.; Archer, S.; Shuler, M. L.; Wu, M. A hydrogel-based microfluidic device for the studies of directed cell migration. *Lab Chip* **2007**, *7* (6), 763 DOI: 10.1039/b618463d.
- (75) Golden, A. P.; Tien, J. Fabrication of microfluidic hydrogels using molded gelatin as a sacrificial element. *Lab Chip* **2007**, *7* (6), 720 DOI: 10.1039/b618409j.
- (76) Ling, Y.; Rubin, J.; Deng, Y.; Huang, C.; Demirci, U.; Karp, J. M.; Khademhosseini, A. A cell-laden microfluidic hydrogel. *Lab Chip* **2007**, *7* (6), 756–762 DOI: 10.1039/b615486g.
- (77) Wang, X.-Y.; Jin, Z.-H.; Gan, B.-W.; Lv, S.-W.; Xie, M.; Huang, W.-H. Engineering interconnected 3D vascular networks in hydrogels using molded sodium alginate lattice as the sacrificial template. *Lab Chip* **2014**, *14* (15), 2709–2716 DOI: 10.1039/C4LC00069B.
- (78) Cuchiara, M. P.; Allen, A. C. B.; Chen, T. M.; Miller, J. S.; West, J. L. Multilayer microfluidic PEGDA hydrogels. *Biomaterials* **2010**, *31* (21), 5491–5497 DOI: 10.1016/j.biomaterials.2010.03.031.
- (79) Cui, H.; Nowicki, M.; Fisher, J. P.; Zhang, L. G. 3D Bioprinting for Organ Regeneration. *Adv. Healthc. Mater.* **2017**, *6* (1), 1601118 DOI: 10.1002/adhm.201601118.
- (80) Lee, V. K.; Kim, D. Y.; Ngo, H.; Lee, Y.; Seo, L.; Yoo, S.-S.; Vincent, P. A.; Dai, G. Creating perfused functional vascular channels using 3D bio-printing technology. *Biomaterials* **2014**, *35* (28), 8092–8102 DOI: 10.1016/j.biomaterials.2014.05.083.
- (81) Mandrycky, C.; Wang, Z.; Kim, K.; Kim, D.-H. 3D bioprinting for engineering complex tissues. *Biotechnol. Adv.* **2016**, *34* (4), 422–434 DOI: 10.1016/j.biotechadv.2015.12.011.
- (82) Murphy, S. V.; Atala, A. 3D bioprinting of tissues and organs. *Nat. Biotechnol.* **2014**, *32* (8), 773–785 DOI: 10.1038/nbt.2958.
- (83) Xu, T.; Zhao, W.; Zhu, J. M.; Albanna, M. Z.; Yoo, J. J.; Atala, A. Complex heterogeneous tissue constructs containing multiple cell types prepared by inkjet printing technology. *Biomaterials* **2013**, *34* (1), 130–139 DOI: 10.1016/j.biomaterials.2012.09.035.
- (84) Koch, L.; Deiwick, A.; Schlie, S.; Michael, S.; Gruene, M.; Coger, V.; Zychlinski, D.; Schambach, A.; Reimers, K.; Vogt, P. M.; et al. Skin tissue generation by laser cell printing. *Biotechnol. Bioeng.* **2012**, *109* (7), 1855–1863 DOI: 10.1002/bit.24455.
- (85) Billiet, T.; Vandenhaute, M.; Schelfhout, J.; Van Vlierberghe, S.; Dubruel, P. A review of trends and limitations in hydrogel-rapid prototyping for tissue engineering. *Biomaterials* **2012**, *33* (26), 6020–6041 DOI: 10.1016/j.biomaterials.2012.04.050.
- (86) Pfister, A.; Landers, R.; Laib, A.; Hübner, U.; Schmelzeisen, R.; Mülhaupt, R. Biofunctional Rapid Prototyping for Tissue-Engineering Applications: 3D Bioplotting versus 3D Printing. *J. Polym. Sci. Part A Polym. Chem.* **2004**, *42* (3), 624–638 DOI: 10.1002/pola.10807.
- (87) Ozbolat, I. T.; Hospodiuk, M. Current advances and future perspectives in extrusion-based bioprinting. *Biomaterials* **2016**, *76*, 321–343 DOI: 10.1016/j.biomaterials.2015.10.076.

- (88) Dababneh, A. B.; Ozbolat, I. T. Bioprinting Technology: A Current State-of-the-Art Review. *J. Manuf. Sci. Eng.* **2014**, *136* (6), 61016 DOI: 10.1115/1.4028512.
- (89) Rosenzweig, D. H.; Carelli, E.; Steffen, T.; Jarzem, P.; Haglund, L. 3D-printed ABS and PLA scaffolds for cartilage and nucleus pulposus tissue regeneration. *Int. J. Mol. Sci.* **2015**, *16* (7), 15118–15135 DOI: 10.3390/ijms160715118.
- (90) Schuurman, W.; Khristov, V.; Pot, M. W.; van Weeren, P. R.; Dhert, W. J. a; Malda, J. Bioprinting of hybrid tissue constructs with tailorable mechanical properties. *Biofabrication* **2011**, *3* (2), 21001 DOI: 10.1088/1758-5082/3/2/021001.
- (91) Kinstlinger, I. S.; Miller, J. 3D-printed Fluidic Networks as Vasculature for Engineered Tissue. *Lab Chip* **2016**, *16* (3), 2025–2043 DOI: 10.1039/C6LC00193A.
- (92) Hinton, T. J.; Jallerat, Q.; Palchesko, R. N.; Park, J. H.; Grodzicki, M. S.; Shue, H.-J.; Ramadan, M. H.; Hudson, A. R.; Feinberg, A. W. Three-dimensional printing of complex biological structures by freeform reversible embedding of suspended hydrogels. *Sci. Adv.* **2015**, *1* (9), e1500758–e1500758 DOI: 10.1126/sciadv.1500758.
- (93) Hinton, T. J.; Hudson, A.; Pusch, K.; Lee, A.; Feinberg, A. W. 3D Printing PDMS Elastomer in a Hydrophilic Support Bath via Freeform Reversible Embedding. *ACS Biomater. Sci. Eng.* **2016**, *2* (10), 1781–1786 DOI: 10.1021/acsbiomaterials.6b00170.
- (94) Highley, C. B.; Rodell, C. B.; Burdick, J. A. Direct 3D Printing of Shear-Thinning Hydrogels into Self-Healing Hydrogels. *Adv. Mater.* **2015**, *27* (34), 5075–5079 DOI: 10.1002/adma.201501234.
- (95) Bhattacharjee, T.; Zehnder, S. M.; Rowe, K. G.; Jain, S.; Nixon, R. M.; Sawyer, W. G.; Angelini, T. E. Writing in the granular gel medium. *Sci. Adv.* **2015**, *1* (8), e1500655–e1500655 DOI: 10.1126/sciadv.1500655.
- (96) Moxon, S. R.; Cooke, M. E.; Cox, S. C.; Snow, M.; Jeys, L.; Jones, S. W.; Smith, A. M.; Grover, L. M. Suspended Manufacture of Biological Structures. *Adv. Mater.* **2017**, *29* (13), 1605594 DOI: 10.1002/adma.201605594.
- (97) Zhang, Y.; Yu, Y.; Ozbolat, I. T. Direct Bioprinting of Vessel-Like Tubular Microfluidic Channels. *J. Nanotechnol. Eng. Med.* **2013**, *4* (2), 20902 DOI: 10.1115/1.4024398.
- (98) Zhang, Y.; Yu, Y.; Chen, H.; Ozbolat, I. T. Characterization of printable cellular microfluidic channels for tissue engineering. *Biofabrication* **2013**, *5* (2), 25004 DOI: 10.1088/1758-5082/5/2/025004.
- (99) Onoe, H.; Okitsu, T.; Itou, A.; Kato-Negishi, M.; Gojo, R.; Kiriya, D.; Sato, K.; Miura, S.; Iwanaga, S.; Kuribayashi-Shigetomi, K.; et al. Metre-long cell-laden microfibres exhibit tissue morphologies and functions. *Nat. Mater.* **2013**, *12* (6), 584–590 DOI: 10.1038/nmat3606.
- (100) Yu, Y.; Zhang, Y.; Ozbolat, I. T. A Hybrid Bioprinting Approach for Scale-Up Tissue Fabrication. *J. Manuf. Sci. Eng.* **2014**, *136* (6), 61013 DOI: 10.1115/1.4028511.
- (101) Grolman, J. M.; Zhang, D.; Smith, A. M.; Moore, J. S.; Kilian, K. A. Rapid 3D Extrusion of Synthetic Tumor Microenvironments. *Adv. Mater.* **2015**, *27* (37), 5512–5517 DOI: 10.1002/adma.201501729.
- (102) Morimoto, Y.; Hsiao, A. Y.; Takeuchi, S. Point-, line-, and plane-shaped cellular constructs for 3D tissue assembly. *Adv. Drug Deliv. Rev.* **2015**, *95*, 29–39 DOI: 10.1016/j.addr.2015.09.003.
- (103) Gao, Q.; He, Y.; Fu, J.; Liu, A.; Ma, L. Coaxial nozzle-assisted 3D bioprinting with built-in microchannels for nutrients delivery. *Biomaterials* **2015**, *61*, 203–215 DOI: 10.1016/j.biomaterials.2015.05.031.
- (104) Zhang, Y.; Yu, Y.; Akkouch, A.; Dababneh, A.; Dolati, F.; Ozbolat, I. T. In vitro study of directly bioprinted perfusable vasculature conduits. *Biomater. Sci.* **2015**, *3* (1), 134–143 DOI: 10.1039/C4BM00234B.
- (105) Alessandri, K.; Feyeux, M.; Gurchenkov, B.; Delgado, C.; Trushko, A.; Krause, K.-H.; Vignjević, D.; Nassoy, P.; Roux, A. A 3D printed microfluidic device for production of

- functionalized hydrogel microcapsules for culture and differentiation of human Neuronal Stem Cells (hNSC). *Lab Chip* **2016**, *16* (9), 1593–1604 DOI: 10.1039/C6LC00133E.
- (106) Jia, W.; Gungor-Ozkerim, P. S.; Zhang, Y. S.; Yue, K.; Zhu, K.; Liu, W.; Pi, Q.; Byambaa, B.; Dokmeci, M. R.; Shin, S. R.; et al. Direct 3D bioprinting of perfusable vascular constructs using a blend bioink. *Biomaterials* **2016**, *106*, 58–68 DOI: 10.1016/j.biomaterials.2016.07.038.
- (107) Colosi, C.; Shin, S. R.; Manoharan, V.; Massa, S.; Costantini, M.; Barbetta, A.; Dokmeci, M. R.; Dentini, M.; Khademhosseini, A. Microfluidic Bioprinting of Heterogeneous 3D Tissue Constructs Using Low-Viscosity Bioink. *Adv. Mater.* **2016**, *28* (4), 677–684 DOI: 10.1002/adma.201503310.
- (108) Hsiao, A. Y.; Okitsu, T.; Teramae, H.; Takeuchi, S. 3D Tissue Formation of Unilocular Adipocytes in Hydrogel Microfibers. *Adv. Healthc. Mater.* **2016**, *5* (5), 548–556 DOI: 10.1002/adhm.201500673.
- (109) Ouyang, L.; Highley, C. B.; Sun, W.; Burdick, J. A. A Generalizable Strategy for the 3D Bioprinting of Hydrogels from Nonviscous Photo-crosslinkable Inks. *Adv. Mater.* **2017**, *29* (8), 1604983 DOI: 10.1002/adma.201604983.
- (110) Kato-Negishi, M.; Onoe, H.; Ito, A.; Takeuchi, S. Rod-Shaped Neural Units for Aligned 3D Neural Network Connection. *Adv. Healthc. Mater.* **2017**, *6* (15), 1700143 DOI: 10.1002/adhm.201700143.
- (111) Yu, Y.; Fu, F.; Shang, L.; Cheng, Y.; Gu, Z.; Zhao, Y. Bioinspired Helical Microfibers from Microfluidics. *Adv. Mater.* **2017**, *29* (18), 1605765 DOI: 10.1002/adma.201605765.
- (112) Miller, J. S.; Stevens, K. R.; Yang, M. T.; Baker, B. M.; Nguyen, D.-H. T.; Cohen, D. M.; Toro, E.; Chen, A. A.; Galie, P. A.; Yu, X.; et al. Rapid casting of patterned vascular networks for perfusable engineered three-dimensional tissues. *Nat. Mater.* **2012**, *11* (9), 768–774 DOI: 10.1038/nmat3357.
- (113) Lee, V. K.; Lanzi, A. M.; Ngo, H.; Yoo, S.-S.; Vincent, P. A.; Dai, G. Generation of Multi-scale Vascular Network System Within 3D Hydrogel Using 3D Bio-printing Technology. *Cell. Mol. Bioeng.* **2014**, *7* (3), 460–472 DOI: 10.1007/s12195-014-0340-0.
- (114) Bertassoni, L. E.; Cecconi, M.; Manoharan, V.; Nikkhah, M.; Hjortnaes, J.; Cristino, A. L.; Barabaschi, G.; Demarchi, D.; Dokmeci, M. R.; Yang, Y.; et al. Hydrogel bioprinted microchannel networks for vascularization of tissue engineering constructs. *Lab Chip* **2014**, *14* (13), 2202–2211 DOI: 10.1039/C4LC00030G.
- (115) Kolesky, D. B.; Truby, R. L.; Gladman, A. S.; Busbee, T. A.; Homan, K. A.; Lewis, J. A. 3D Bioprinting of Vascularized, Heterogeneous Cell-Laden Tissue Constructs. *Adv. Mater.* **2014**, *26* (19), 3124–3130 DOI: 10.1002/adma.201305506.
- (116) Kolesky, D. B.; Homan, K. A.; Skylar-Scott, M. A.; Lewis, J. A. Three-dimensional bioprinting of thick vascularized tissues. *Proc. Natl. Acad. Sci.* **2016**, *113* (12), 3179–3184 DOI: 10.1073/pnas.1521342113.
- (117) Zhang, Y. S.; Davoudi, F.; Walch, P.; Manbachi, A.; Luo, X.; Dell’Erba, V.; Miri, A. K.; Albadawi, H.; Arneri, A.; Li, X.; et al. Bioprinted thrombosis-on-a-chip. *Lab Chip* **2016**, *16* (21), 4097–4105 DOI: 10.1039/C6LC00380J.
- (118) Hull, C. W. Apparatus for production of three-dimensional objects by stereolithography. US4575330, 1986.
- (119) Melchels, F. P. W.; Feijen, J.; Grijpma, D. W. A review on stereolithography and its applications in biomedical engineering. *Biomaterials* **2010**, *31* (24), 6121–6130 DOI: 10.1016/j.biomaterials.2010.04.050.
- (120) Skoog, S. A.; Goering, P. L.; Narayan, R. J. Stereolithography in tissue engineering. *J. Mater. Sci. Mater. Med.* **2014**, *25* (3), 845–856 DOI: 10.1007/s10856-013-5107-y.
- (121) Au, A. K.; Huynh, W.; Horowitz, L. F.; Folch, A. 3D-Printed Microfluidics. *Angew. Chemie Int. Ed.* **2016**, *55* (12), 3862–3881 DOI: 10.1002/anie.201504382.

- (122) Corbel, S.; Dufaud, O.; Roques-Carmes, T. *Stereolithography*; Bártolo, P. J., Ed.; Springer US: Boston, MA, 2011.
- (123) Ozbolat, I. T.; Ozbolat, I. T. 06-Laser-Based Bioprinting. In *3D Bioprinting*; 2017; pp 165–197.
- (124) Mapili, G.; Lu, Y.; Chen, S.; Roy, K. Laser-layered microfabrication of spatially patterned functionalized tissue-engineering scaffolds. *J. Biomed. Mater. Res. B. Appl. Biomater.* **2005**, *75* (2), 414–424 DOI: 10.1002/jbm.b.30325.
- (125) Lu, Y.; Mapili, G.; Suhali, G.; Chen, S.; Roy, K. A digital micro-mirror device-based system for the microfabrication of complex, spatially patterned tissue engineering scaffolds. *J. Biomed. Mater. Res. - Part A* **2006**, *77* (2), 396–405 DOI: 10.1002/jbm.a.30601.
- (126) Lee, K. W.; Wang, S.; Fox, B. C.; Ritman, E. L.; Yaszemski, M. J.; Lu, L. Poly(propylene fumarate) bone tissue engineering scaffold fabrication using stereolithography: Effects of resin formulations and laser parameters. *Biomacromolecules* **2007**, *8* (4), 1077–1084 DOI: 10.1021/bm060834v.
- (127) Han, L.-H.; Chen, S.; Mapili, G.; Roy, K. Projection Microfabrication of Three-Dimensional Scaffolds for Tissue Engineering. *J. Manuf. Sci. Eng.* **2008**, *130* (2), 21005 DOI: 10.1115/1.2823079.
- (128) Lee, S. J.; Kang, H. W.; Park, J. K.; Rhie, J. W.; Hahn, S. K.; Cho, D. W. Application of microstereolithography in the development of three-dimensional cartilage regeneration scaffolds. *Biomed. Microdevices* **2008**, *10* (2), 233–241 DOI: 10.1007/s10544-007-9129-4.
- (129) Melchels, F. P. W.; Feijen, J.; Grijpma, D. W. A poly(d,l-lactide) resin for the preparation of tissue engineering scaffolds by stereolithography. *Biomaterials* **2009**, *30* (23–24), 3801–3809 DOI: 10.1016/j.biomaterials.2009.03.055.
- (130) Jansen, J.; Melchels, F. P. W.; Grijpma, D. W.; Feijen, J. Fumaric Acid Monoethyl Ester-Functionalized Poly (D,L-lactide)/N-vinyl-2-pyrrolidone Resins for the Preparation of Tissue Engineering Scaffolds by Stereolithography. *Biomacromolecules* **2009**, *10* (2), 214–220 DOI: 10.1021/bm801001r.
- (131) Schuster, M.; Turecek, C.; Weigel, G.; Saf, R.; Stampfl, J.; Varga, F.; Liska, R. Gelatin-based photopolymers for bone replacement materials. *J. Polym. Sci. Part A Polym. Chem.* **2009**, *47* (24), 7078–7089 DOI: 10.1002/pola.23747.
- (132) Seck, T. M.; Melchels, F. P. W.; Feijen, J.; Grijpma, D. W. Designed biodegradable hydrogel structures prepared by stereolithography using poly(ethylene glycol)/poly(d,l-lactide)-based resins. *J. Control. Release* **2010**, *148* (1), 34–41 DOI: 10.1016/j.jconrel.2010.07.111.
- (133) Lee, J. W.; Ahn, G.; Cho, D. W.; Kim, J. Y. Evaluating cell proliferation based on internal pore size and 3D scaffold architecture fabricated using solid freeform fabrication technology. *J. Mater. Sci. Mater. Med.* **2010**, *21* (12), 3195–3205 DOI: 10.1007/s10856-010-4173-7.
- (134) Han, L. H.; Suri, S.; Schmidt, C. E.; Chen, S. Fabrication of three-dimensional scaffolds for heterogeneous tissue engineering. *Biomed. Microdevices* **2010**, *12* (4), 721–725 DOI: 10.1007/s10544-010-9425-2.
- (135) Elomaa, L.; Teixeira, S.; Hakala, R.; Korhonen, H.; Grijpma, D. W.; Seppälä, J. V. Preparation of poly(ε-caprolactone)-based tissue engineering scaffolds by stereolithography. *Acta Biomater.* **2011**, *7* (11), 3850–3856 DOI: 10.1016/j.actbio.2011.06.039.
- (136) Soman, P.; Kelber, J. A.; Lee, J. W.; Wright, T. N.; Vecchio, K. S.; Klemke, R. L.; Chen, S. Cancer cell migration within 3D layer-by-layer microfabricated photocrosslinked PEG scaffolds with tunable stiffness. *Biomaterials* **2012**, *33* (29), 7064–7070 DOI: 10.1016/j.biomaterials.2012.06.012.

- (137) Gauvin, R.; Chen, Y. C.; Lee, J. W.; Soman, P.; Zorlutuna, P.; Nichol, J. W.; Bae, H.; Chen, S.; Khademhosseini, A. Microfabrication of complex porous tissue engineering scaffolds using 3D projection stereolithography. *Biomaterials* **2012**, *33* (15), 3824–3834 DOI: 10.1016/j.biomaterials.2012.01.048.
- (138) Lin, H.; Zhang, D.; Alexander, P. G.; Yang, G.; Tan, J.; Cheng, A. W.-M.; Tuan, R. S. Application of visible light-based projection stereolithography for live cell-scaffold fabrication with designed architecture. *Biomaterials* **2013**, *34* (2), 331–339 DOI: 10.1016/j.biomaterials.2012.09.048.
- (139) Grogan, S. P.; Chung, P. H.; Soman, P.; Chen, P.; Lotz, M. K.; Chen, S.; D’Lima, D. D. Digital micromirror device projection printing system for meniscus tissue engineering. *Acta Biomater.* **2013**, *9* (7), 7218–7226 DOI: 10.1016/j.actbio.2013.03.020.
- (140) Leigh, S. J.; Gilbert, H. T. J.; Barker, I. A.; Becker, J. M.; Richardson, S. M.; Hoyland, J. A.; Covington, J. A.; Dove, A. P. Fabrication of 3-dimensional cellular constructs via microstereolithography using a simple, three-component, poly(ethylene glycol) acrylate-based system. *Biomacromolecules* **2013**, *14* (1), 186–192.
- (141) Ronca, A.; Ambrosio, L.; Grijpma, D. W. Preparation of designed poly(d,l-lactide)/nanosized hydroxyapatite composite structures by stereolithography. *Acta Biomater.* **2013**, *9* (4), 5989–5996 DOI: 10.1016/j.actbio.2012.12.004.
- (142) Ozbolat, I. T.; Ozbolat, I. T. 02-Design for Bioprinting. In *3D Bioprinting*; 2017; pp 13–39.
- (143) Melchiorri, A. J.; Hibino, N.; Best, C. A.; Yi, T.; Lee, Y. U.; Kraynak, C. A.; Kimerer, L. K.; Krieger, A.; Kim, P.; Breuer, C. K.; et al. 3D-Printed Biodegradable Polymeric Vascular Grafts. *Adv. Healthc. Mater.* **2016**, *5* (3), 319–325 DOI: 10.1002/adhm.201500725.
- (144) Arcaute, K.; Mann, B. K.; Wicker, R. B. Stereolithography of three-dimensional bioactive poly(ethylene glycol) constructs with encapsulated cells. *Ann. Biomed. Eng.* **2006**, *34* (9), 1429–1441 DOI: 10.1007/s10439-006-9156-y.
- (145) Gong, H.; Bickham, B.; Woolley, A. T.; Nordin, G. P. Custom 3D printer and resin for 18 μm \times 20 μm microfluidic flow channels. *Lab Chip* **2017** DOI: 10.1039/C7LC00644F.
- (146) Gong, H.; Beauchamp, M.; Perry, S.; Woolley, A. T.; Nordin, G. P. Optical approach to resin formulation for 3D printed microfluidics. *RSC Adv.* **2015**, *5* (129), 3627–3637 DOI: 10.1039/C5RA23855B.
- (147) Suri, S.; Han, L.-H.; Zhang, W.; Singh, A.; Chen, S.; Schmidt, C. E. Solid freeform fabrication of designer scaffolds of hyaluronic acid for nerve tissue engineering. *Biomed. Microdevices* **2011**, *13*, 983–993 DOI: 10.1007/s10544-011-9568-9.
- (148) Urrios, A.; Parra-Cabrera, C.; Bhattacharjee, N.; Gonzalez-Suarez, A. M.; Rigat Brugarolas, L. G.; Nallapati, U.; Samitier, J.; DeForest, C.; Posas, F.; Garcia-Cordero, J. L.; et al. 3D-Printing of Transparent Bio-Microfluidic Devices in Peg-Da. *Lab Chip* **2016**, *16*, 2287–2294 DOI: 10.1039/C6LC00153J.
- (149) Chan, V.; Zorlutuna, P.; Jeong, J. H.; Kong, H.; Bashir, R. Three-dimensional photopatterning of hydrogels using stereolithography for long-term cell encapsulation. *Lab Chip* **2010**, *10* (16), 2062–2070 DOI: 10.1039/c004285d.
- (150) Arcaute, K.; Mann, B.; Wicker, R. Stereolithography of spatially controlled multi-material bioactive poly(ethylene glycol) scaffolds. *Acta Biomater.* **2010**, *6* (3), 1047–1054 DOI: 10.1016/j.actbio.2009.08.017.
- (151) Ma, X.; Qu, X.; Zhu, W.; Li, Y.-S.; Yuan, S.; Zhang, H.; Liu, J.; Wang, P.; Lai, C. S. E.; Zanella, F.; et al. Deterministically patterned biomimetic human iPSC-derived hepatic model via rapid 3D bioprinting. *Proc. Natl. Acad. Sci.* **2016**, *113* (8), 201524510 DOI: 10.1073/pnas.1524510113.
- (152) Elomaa, L.; Pan, C.-C.; Shanjani, Y.; Malkovskiy, A.; Seppälä, J. V.; Yang, Y. Three-dimensional fabrication of cell-laden biodegradable poly(ethylene glycol-co-depsipeptide) hydrogels by visible light stereolithography. *J. Mater. Chem. B* **2015**, *3*

- (42), 8348–8358 DOI: 10.1039/C5TB01468A.
- (153) Dhariwala, B.; Hunt, E.; Boland, T. Rapid Prototyping of Tissue-Engineering Constructs, Using Photopolymerizable Hydrogels and Stereolithography. *Tissue Eng.* **2004**, *10* (9–10), 1316–1322 DOI: 10.1089/ten.2004.10.1316.
 - (154) Wang, Z.; Abdulla, R.; Parker, B.; Samanipour, R. A simple and high-resolution stereolithography-based 3D bioprinting system using visible light crosslinkable bioinks. *Biofabrication* **2015**, *7* (4), 1–29 DOI: 10.1088/1758-5090/7/4/045009.
 - (155) Zhu, W.; Qu, X.; Zhu, J.; Ma, X.; Patel, S.; Liu, J.; Wang, P.; Lai, C. S. E.; Gou, M.; Xu, Y.; et al. Direct 3D bioprinting of prevascularized tissue constructs with complex microarchitecture. *Biomaterials* **2017**, *124*, 106–115 DOI: 10.1016/j.biomaterials.2017.01.042.
 - (156) Mazzocchi, J. P.; Feke, D. L.; Baskaran, H.; Pintauro, P. N. Mechanical and cell viability properties of crosslinked low- And high-molecular weight poly(ethylene glycol) diacrylate blends. *J. Biomed. Mater. Res. - Part A* **2010**, *93* (2), 558–566 DOI: 10.1002/jbm.a.32563.
 - (157) Weber, L. M.; Lopez, C. G.; Anseth, K. S. Effects of PEG hydrogel crosslinking density on protein diffusion and encapsulated islet survival and function. *J. Biomed. Mater. Res. Part A* **2009**, *90A* (3), 720–729 DOI: 10.1002/jbm.a.32134.
 - (158) Mironi-Harpaz, I.; Wang, D. Y.; Venkatraman, S.; Seliktar, D. Photopolymerization of cell-encapsulating hydrogels: Crosslinking efficiency versus cytotoxicity. *Acta Biomater.* **2012**, *8* (5), 1838–1848 DOI: 10.1016/j.actbio.2011.12.034.
 - (159) Faralli, A.; Melander, F.; Larsen, E. K. U.; Chernyy, S.; Andresen, T. L.; Larsen, N. B. Multiplexed Dosing Assays by Digitally Definable Hydrogel Volumes. *Adv. Healthc. Mater.* **2016**, *5* (2), 244–254 DOI: 10.1002/adhm.201500542.
 - (160) Fairbanks, B. D.; Schwartz, M. P.; Bowman, C. N.; Anseth, K. S. Photoinitiated polymerization of PEG-diacrylate with lithium phenyl-2,4,6-trimethylbenzoylphosphinate: polymerization rate and cytocompatibility. *Biomaterials* **2009**, *30* (35), 6702–6707 DOI: 10.1016/j.biomaterials.2009.08.055.
 - (161) Zheng, Y.; Chen, J.; Lopez, J. A. Microvascular platforms for the study of platelet-vessel wall interactions. *Thromb. Res.* **2014**, *133* (4), 525–531 DOI: 10.1016/j.thromres.2013.12.039.
 - (162) Zhang, A. P.; Qu, X.; Soman, P.; Hribar, K. C.; Lee, J. W.; Chen, S.; He, S. Rapid fabrication of complex 3D extracellular microenvironments by dynamic optical projection stereolithography. *Adv. Mater.* **2012**, *24* (31), 4266–4270 DOI: 10.1002/adma.201202024.
 - (163) Shanjani, Y.; Pan, C. C.; Elomaa, L.; Yang, Y. A novel bioprinting method and system for forming hybrid tissue engineering constructs. *Biofabrication* **2015**, *7* (4), 45008 DOI: 10.1088/1758-5090/7/4/045008.
 - (164) Rennerfeldt, D. A.; Renth, A. N.; Talata, Z.; Gehrke, S. H.; Detamore, M. S. Tuning mechanical performance of poly(ethylene glycol) and agarose interpenetrating network hydrogels for cartilage tissue engineering. *Biomaterials* **2013**, *34* (33), 8241–8257 DOI: 10.1016/j.biomaterials.2013.07.052.
 - (165) Peyton, S. R.; Raub, C. B.; Keschrumrus, V. P.; Putnam, A. J. The use of poly(ethylene glycol) hydrogels to investigate the impact of ECM chemistry and mechanics on smooth muscle cells. *Biomaterials* **2006**, *27* (28), 4881–4893 DOI: 10.1016/j.biomaterials.2006.05.012.
 - (166) Underhill, G. H.; Chen, A. A.; Albrecht, D. R.; Bhatia, S. N. Assessment of hepatocellular function within PEG hydrogels. *Biomaterials* **2007**, *28* (2), 256–270 DOI: 10.1016/j.biomaterials.2006.08.043.
 - (167) Nemir, S.; Hayenga, H. N.; West, J. L. PEGDA hydrogels with patterned elasticity: Novel tools for the study of cell response to substrate rigidity. *Biotechnol. Bioeng.*

- 2010**, *105* (3), 636–644 DOI: 10.1002/bit.22574.
- (168) Kim, P.; Jeong, H. E.; Khademhosseini, A.; Suh, K. Y. Fabrication of non-biofouling polyethylene glycol micro- and nanochannels by ultraviolet-assisted irreversible sealing. *Lab Chip* **2006**, *6* (11), 1432 DOI: 10.1039/b610503c.
 - (169) Parlato, M.; Reichert, S.; Barney, N.; Murphy, W. L. Poly(ethylene glycol) hydrogels with adaptable mechanical and degradation properties for use in biomedical applications. *Macromol. Biosci.* **2014**, *14* (5), 687–698 DOI: 10.1002/mabi.201300418.
 - (170) Yuan, D.; Lasagni, A.; Shao, P.; Das, S. Rapid prototyping of microstructured hydrogels via laser direct-write and laser interference photopolymerisation. *Virtual Phys. Prototyp.* **2008**, *3* (4), 221–229 DOI: 10.1080/17452750802615713.
 - (171) Michiels, C. Endothelial cell functions. *J. Cell. Physiol.* **2003**, *196* (3), 430–443 DOI: 10.1002/jcp.10333.
 - (172) Godwin, L. A.; Deal, K. S.; Hoepfner, L. D.; Jackson, L. A.; Easley, C. J. Measurement of microchannel fluidic resistance with a standard voltage meter. *Anal. Chim. Acta* **2013**, *758*, 101–107 DOI: 10.1016/j.aca.2012.10.043.
 - (173) Liu Tsang, V.; Chen, A. A.; Cho, L. M.; Jadin, K. D.; Sah, R. L.; DeLong, S.; West, J. L.; Bhatia, S. N. Fabrication of 3D hepatic tissues by additive photopatterning of cellular hydrogels. *FASEB J.* **2007**, *21* (3), 790–801 DOI: 10.1096/fj.06-7117com.
 - (174) Larsen, E. K. U.; Mikkelsen, M. B. L.; Larsen, N. B. Protein and cell patterning in closed polymer channels by photoimmobilizing proteins on photografted poly(ethylene glycol) diacrylate. *Biomicrofluidics*. AIP Publishing December 30, 2014, p 64127.
 - (175) Popel, A. S.; Johnson, P. C. Microcirculation and Hemorheology. *Annu. Rev. Fluid Mech.* **2005**, *37*, 43–69 DOI: 10.1146/annurev.fluid.37.042604.133933.
 - (176) Chan, B. P.; Leong, K. W. Scaffolding in tissue engineering: General approaches and tissue-specific considerations. *Eur. Spine J.* **2008**, *17* (SUPPL. 4) DOI: 10.1007/s00586-008-0745-3.
 - (177) Boughen, L.; Liggat, J.; Ellis, G. Thermal degradation of polyethylene glycol 6000 and its effect on the assay of macroprolactin. *Clin. Biochem.* **2010**, *43* (9), 750–753 DOI: 10.1016/j.clinbiochem.2010.02.012.
 - (178) Han, S.; Kim, C.; Kwon, D. Thermal/oxidative degradation and stabilization of polyethylene glycol. *Polymer (Guildf)*. **1997**, *38* (2), 317–323 DOI: 10.1016/S0032-3861(97)88175-X.
 - (179) Pielichowski, K.; Flejtuch, K. Differential scanning calorimetry studies on poly(ethylene glycol) with different molecular weights for thermal energy storage materials. *Polym. Adv. Technol.* **2002**, *13* (10–12), 690–696 DOI: 10.1002/pat.276.
 - (180) Amador, C.; Urban, M. W.; Shigao Chen; Qingshan Chen; Kai-Nan An; Greenleaf, J. F. Shear Elastic Modulus Estimation From Indentation and SDUV on Gelatin Phantoms. *IEEE Trans. Biomed. Eng.* **2011**, *58* (6), 1706–1714 DOI: 10.1109/TBME.2011.2111419.
 - (181) Nichol, J. W.; Koshy, S. T.; Bae, H.; Hwang, C. M.; Yamanlar, S.; Khademhosseini, A. Cell-laden microengineered gelatin methacrylate hydrogels. *Biomaterials* **2010**, *31* (21), 5536–5544 DOI: 10.1016/j.biomaterials.2010.03.064.
 - (182) Djabourov, M.; Lechaire, J. P.; Gaill, F. Structure and rheology of gelatin and collagen gels. *Biorheology* **1993**, *30* (3–4), 191–205.
 - (183) Kolesky, D. B.; Truby, R. L.; Gladman, A. S.; Busbee, T. A.; Homan, K. A.; Lewis, J. A. 3D bioprinting of vascularized, heterogeneous cell-laden tissue constructs. *Adv. Mater.* **2014**, *26* (19), 3124–3130 DOI: 10.1002/adma.201305506.
 - (184) Treloar, L. R. G. *The physics of rubber elasticity*, 3rd ed.; Oxford University Press, 1975.
 - (185) Thévenaz, P.; Ruttimann, U. E.; Unser, M. A pyramid approach to subpixel registration based on intensity. *IEEE Trans. Image Process.* **1998**, *7* (1), 27–41 DOI: 10.1109/83.650848.
 - (186) Schindelin, J.; Arganda-Carreras, I.; Frise, E.; Kaynig, V.; Longair, M.; Pietzsch, T.;

- Preibisch, S.; Rueden, C.; Saalfeld, S.; Schmid, B.; et al. Fiji: an open-source platform for biological-image analysis. *Nat. Methods* **2012**, *9* (7), 676–682 DOI: 10.1038/nmeth.2019.
- (187) Zorlutuna, P.; Jeong, J. H.; Kong, H.; Bashir, R. Stereolithography-Based Hydrogel Microenvironments to Examine Cellular Interactions. *Adv. Funct. Mater.* **2011**, *21* (19), 3642–3651 DOI: 10.1002/adfm.201101023.
- (188) Raman, R.; Bhaduri, B.; Mir, M.; Shkumatov, A.; Lee, M. K.; Popescu, G.; Kong, H.; Bashir, R. High-Resolution Projection Microstereolithography for Patterning of Neovasculature. *Adv. Healthc. Mater.* **2016**, *5* (5), 610–619 DOI: 10.1002/adhm.201500721.
- (189) Larsen, E. K. U.; Larsen, N. B.; Almdal, K.; Larsen, E. K. U.; Larsen, N. B.; Almdal, K. Multimaterial hydrogel with widely tunable elasticity by selective photopolymerization of PEG diacrylate and epoxy monomers. *J. Polym. Sci. Part B Polym. Phys.* **2016**, 1–7 DOI: 10.1002/polb.24007.
- (190) Lee, H.; Park, W.; Ryu, H.; Jeon, N. L. A microfluidic platform for quantitative analysis of cancer angiogenesis and intravasation. *Biomicrofluidics* **2014**, *8* (5), 54102 DOI: 10.1063/1.4894595.
- (191) Vu, T. Q.; de Castro, R. M. B.; Qin, L. Bridging the gap: microfluidic devices for short and long distance cell–cell communication. *Lab Chip* **2017**, *17* (6), 1009–1023 DOI: 10.1039/C6LC01367H.
- (192) Zhao, L.; Lee, V. K.; Yoo, S. S.; Dai, G.; Intes, X. The integration of 3-D cell printing and mesoscopic fluorescence molecular tomography of vascular constructs within thick hydrogel scaffolds. *Biomaterials* **2012**, *33* (21), 5325–5332 DOI: 10.1016/j.biomaterials.2012.04.004.
- (193) Chen, Y. Y.; Silva, P. N.; Syed, A. M.; Sindhwani, S.; Rocheleau, J. V.; Chan, W. C. W. Clarifying intact 3D tissues on a microfluidic chip for high-throughput structural analysis. *Proc. Natl. Acad. Sci.* **2016**, *113* (52), 14915–14920 DOI: 10.1073/pnas.1609569114.

External dissemination

Papers in peer reviewed journals

- *Stereolithographic hydrogel printing of 3D culture chips with biofunctionalized complex 3D perfusion networks*
Rujing Zhang, Niels B. Larsen
Lab on a Chip, 2017, **17**, 4273-4282

Conference contributions

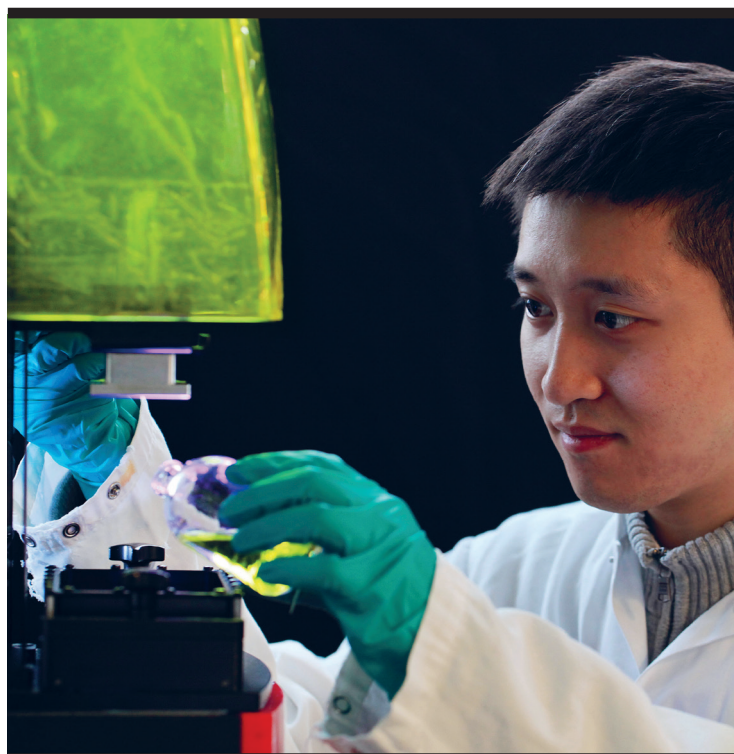
- *Stereolithography-based 3D printing of microchannels for vascularized hydrogels (oral presentation)*
Rujing Zhang, Mikkell Juul, Maryam Sami, Mads Frandsen, Niels B. Larsen
10th World Biomaterials Congress, Montreal, Canada, May 17-22, 2016.
- *Stereolithography of poly(ethylene glycol) hydrogels produces micro-containers for cell culture and microchannels for vascular networks (poster presentation)*
Rujing Zhang, Rodrigo Guzman, Sarah S. Rosenaa, Mikkell H. Juul, Niels B. Larsen
Biofabrication Conference, Utrecht, Netherlands, November 7-9, 2015.
- *Stereolithographic 3D printing of hydrogels using light-controlled radical polymerization (poster presentation)*
Rujing Zhang, Niels B. Larsen
Italian-Nordic Polymer Future, Pisa, Italy, September 14-15, 2017.

Appendix:

Stereolithographic hydrogel printing of 3D culture chips with biofunctionalized complex 3D perfusion networks

Rujing Zhang, Niels B. Larsen

<http://pubs.rsc.org/en/Content/ArticleLanding/2017/LC/C7LC00926G#!divAbstract>



Copyright: Rujing Zhang
All rights reserved

Published by:
DTU Nanotech
Department of Micro- and Nanotechnology
Technical University of Denmark
Ørstedes Plads, building 345C
DK-2800 Kgs. Lyngby